JOURNAL OF THE AERONAUTICAL SCIENCES

INSTITUTE OF THE AERONAUTICAL SCIENCES

ST. LOUIS
NOV 1955
PUBLIC LIBRARY

VOLUME 22 NOVEMBER, 1955 NUMBER 11

CONTENTS

Supersonic Diffuser Instability ..... CHARLES LEE DAILEY 733

The Stability of Vortex Streets with Consideration of the Spread of Vorticity of the Individual Vortices ..... ULRICH DOMM 750

Design Charts for Transient Temperature Distribution Resulting from Aerodynamic Heating at Supersonic Speeds ..... JOSEPH KAYE AND VICTOR C. M. YEH 755

Gas Dynamic Behavior of Real Gases ..... L. N. TAO 763

Acoustics in Relation to Aerodynamics ..... E. G. RICHARDSON 775

The Ultimate Strength of Multiweb Box Beams in Pure Bending ..... ROBERT A. NEEDHAM 781

A Rigorous Method for Finding the Lift of a Certain Class of Airfoils and Remarks on the Meaning of Schrenk's Approximate Rule ..... OTTO LAPORTE AND HIDEO YOSHIHARA 787

Readers' Forum: "Remarks on the Velocity of Sound," by Max M. Munk; "Strength Under Combined Tension and Bending in the Plastic Range," by J. M. Frankland and R. E. Roach; "Some Comments on 'A Theoretical and Experimental Study of Shock Tube Flows,'" by Darshan S. Dosanjh; "Surge Behavior in a Three-Stage Compressor," by Carl E. Pearson; "Supplementary Remark on 'Airplane Stopping Distance,'" by B. Saelman; "Measurements of the Effect of Two-Dimensional and Three-Dimensional Roughness Elements on Boundary-Layer Transition," by P. S. Klebanoff, G. B. Schubauer, and K. D. Tidstrom; "Errata—'On Buckling of a Clamped Rhombic Thin Plate in Shear,'" by M. Hasegawa 795–804

Published by
INSTITUTE OF THE AERONAUTICAL SCIENCES, INC.

JOURNAL OF THE AERONAUTICAL SCIENCES

Editor: HUGH L. DRYDEN, *Director, NACA*
Associate Editor: ROBERT R. DEXTER
Managing Editor: RITA J. TURINO
Editorial Assistant: CAROLINE TAYLOR

Editorial Committee

Aerodynamics

Dean R. Chapman
Francis H. Clauser
Antonio Ferri
Alexander Flax
R. Paul Harrington
R. T. Jones
Carl Kaplan
H. W. Liepmann
C. C. Lin
H. F. Ludloff
Harold Luskin
John R. Markham
Clark B. Millikan
Shatswell Ober
W. Bailey Oswald
C. D. Perkins
Elliott G. Reid
H. J. E. Reid
Russell Robinson
George S. Schairer
G. B. Schubauer
W. R. Sears
John Stack
Theodore Theodorsen
Th. von Kármán

Air Transport

Charles Froesch
J. A. Herlihy
R. D. Kelly
Otto E. Kirchner
Jerome Lederer
John C. Leslie
R. Dixon Speas

Flight Testing

R. R. Gilruth
Melvin N. Gough
W. L. Howland
W. F. Milliken, Jr.
E. G. Stout

Structures and Materials

W. B. Bleakney
E. W. Conlon
John E. Duberg
E. C. Hartmann
N. J. Hoff
Samuel Levy
J. F. McBrearty
Alfred S. Niles
W. Ramberg
F. R. Shanley
C. R. Strang
S. Timoshenko

Rotating Wing Aircraft

F. B. Gustafson
K. H. Hohenemser
Bartram Kelley
R. B. Maloy
Ralph McClarren
R. H. Miller
R. H. Prewitt
Igor I. Sikorsky

Vibration and Flutter

Lee Arnold
M. A. Biot
R. L. Bisplinghoff
William Bollay
Chieh-Chien Chang
J. P. Den Hartog
I. E. Garrick
Martin Goland
Theodore Theodorsen

Aircraft Design

W. E. Beall
E. H. Heinemann
Hall L. Hibbard
Richard Hutton
C. L. Johnson
A. A. Kartveli
E. G. Stout
F. K. Teichmann
Robert J. Woods

Electronics in Aviation

Welcome W. Bender
K. C. Black
M. V. Kiebert, Jr.
David S. Little
S. B. Rogers
Paul Rosenberg
L. M. Sherer

Physiologic Problems

H. G. Armstrong
Louis H. Bauer
Robert J. Benford
W. Randolph Lovelace, II
Ross A. MacFarland

Fuels and Oils

D. P. Barnard
J. H. Doolittle
Graham Edgar
R. T. Goodwin
A. M. Rothrock

Flight Propulsion

George W. Brady
Frank W. Caldwell
L. S. Hobbs
E. E. Johnson
Joseph Keenan
R. P. Kroon
Hans Reissner
Abe Silverstein
C. Fayette Taylor
E. S. Taylor
P. B. Taylor
E. S. Thompson

Instruments

Allan G. Binnie
Charles H. Colvin
Frank R. Cook
C. S. Draper
S. G. Eskin
O. E. Esval
C. F. Savage
R. C. Sylvander

Meteorology

C. F. Brooks
D. M. Little
F. W. Reichelderfer
K. C. Spengler

SUBSCRIPTION RATES

JOURNAL OF THE AERONAUTICAL SCIENCES, Published Monthly.—United States and Possessions: 1 Year, $12.00; Single Copies, $1.50. Foreign Countries Including Canada (American Currency Rates): 1 Year, $13.00; Single Copies, $1.50.

AERONAUTICAL ENGINEERING REVIEW, Published Monthly.—United States and Possessions: 1 Year, $3.00; Single Copies, $0.50. Foreign Countries Including Canada (American Currency Rates): 1 Year, $3.50; Single Copies, $0.50.

Notices of change of address should be sent to the Institute at least 30 days prior to actual change of address.

Manuscripts for publication, proofs, and all correspondence should be addressed to the Editorial Office of the JOURNAL.

Correspondence regarding subscriptions may be addressed to Publication Office, 20th and Northampton Sts., Easton, Pa., or to the Editorial Office of the JOURNAL OF THE AERONAUTICAL SCIENCES, 2 East 64th Street, New York 21, N.Y.

Copyright, 1955, by the Institute of the Aeronautical Sciences, Inc.

Entered as Second Class Matter at the Post Office, Easton, Pa., May 1, 1937. Acceptance for mailing at a special rate of Postage provided for in the Act of August 24, 1912. Authorized April 29, 1937.

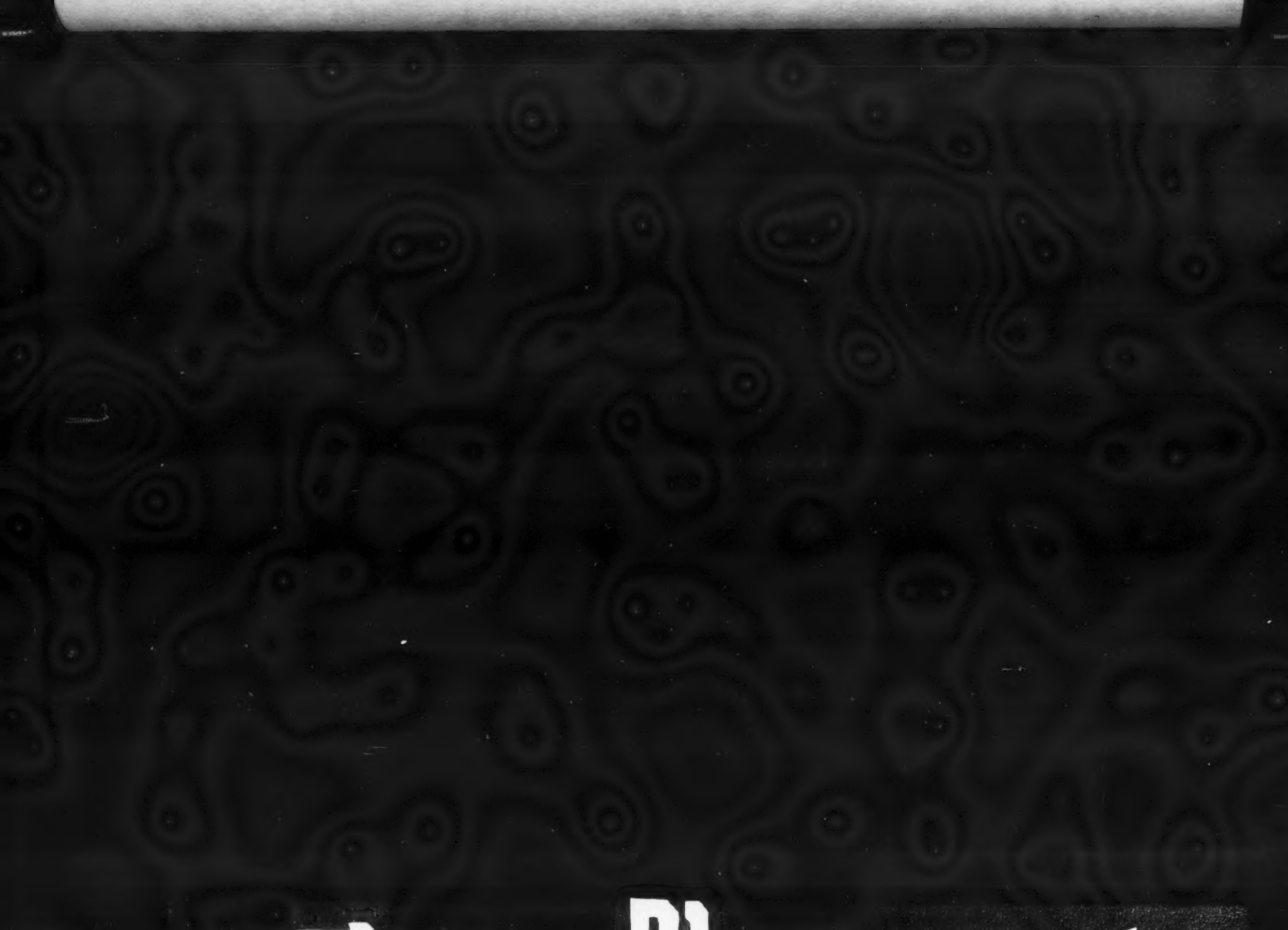

VOL

This
nation
to be c
mum n
phenon
laxation
operatio
subcriti
ternal c
plenum
until th
entering
plenum
tinction
author
noticed
after th
diffuser
pares w
fuser at
expelled
had a s
cases bl
first buz
was fou

P =
ρ =
T =
γ =
R =
M =
R_n =
m =
a =
t =
S =
V =

Receiv
* The
from se
Division,
† Rese

JOURNAL OF THE AERONAUTICAL SCIENCES

VOLUME 22 NOVEMBER, 1955 NUMBER 11

Supersonic Diffuser Instability*

CHARLES LEE DAILEY†

University of Southern California

SUMMARY

This paper presents the results of an experimental determination of the nature and cause of an instability that has been found to be characteristic of supersonic air inlets operating near maximum mass flow. Steady operation is interrupted by a transient phenomenon consisting of a random sequence of individual relaxation cycles. Mass flow entering the diffuser during steady operation is suddenly cut off by a strong interaction between the subcritical shock and boundary layer on the surface of the external compression generator which blocks the inlet. Air in the plenum chamber, stored at high pressure, then "blows down" until the inlet can restart. The subsequent supercritical flow entering the diffuser exceeds the flow rate at the exit, and the plenum chamber is recharged to the original condition. A distinction is drawn between this phenomenon, referred to by the author as "buzz," and a high frequency wave-type resonance noticed at low mass flows and during an individual buzz cycle after the diffuser shock system has been expelled. For the diffuser described herein, this high-frequency oscillation compares well to the eighth closed-end organ pipe mode of the diffuser at low mass flows and to the ninth mode during the shock-expelled phase of the buzz cycle. It was also found that buzz had a strong adverse effect on combustion stability. In most cases blowout occurred immediately with the occurrence of the first buzz cycle. When burning was maintained during buzz, it was found to have no qualitative effect on the buzz cycle.

SYMBOLS

P = pressure
ρ = density
T = temperature
γ = ratio of specific heats
R = gas constant
M = Mach Number
R_n = Reynolds Number
m = mass flow rate
a = speed of sound
t = time
S = cross-section area of stream tube
V = total internal volume of diffuser model
l = effective length—ratio of internal volume to plenum chamber cross-section area
f/a = fuel to air ratio for combustion tests

Subscripts

0 = free-stream conditions
1 = entrance to subsonic diffuser
2 = end of subsonic diffuser
3 = station just downstream of flame arrester
4 = end of combustion chamber
5 = sonic station in exit nozzle
6 = station at engine exit
$*$ = local sonic conditions
s = local stagnation conditions
c = denotes critical diffuser mass flow
e = engine exit

Received October 20, 1954.

* The experimental data presented in this paper were obtained from several investigations supported by the Power Plants Division, U.S. Navy Bureau of Aeronautics.

† Research Associate, Engineering Center.

INTRODUCTION

THERE ARE TWO PRINCIPAL requirements of a supersonic diffuser: First it must decelerate the entering air mass sufficiently to allow steady combustion, and second, it must compress the air mass before heat addition to achieve good thermal efficiency.

The former requirement is easily met; it is a simple matter to reduce the velocity approaching the burner to an arbitrarily low value by appropriate subsonic diffusion. The only penalty is a corresponding reduction in thrust relative to the burner frontal area. This is offset by an increase in cycle efficiency, but the gain is so small that it is of no practical importance. In practice, every effort is made to achieve the maximum burner velocity compatible with good combustion efficiency and stable burner performance. Whatever this maximum is, it simply becomes a design requirement for the diffuser which can easily be met.

The latter problem is more complicated. In order to compress supersonic flow it is necessary to reduce the area through which it passes. In order to achieve good overall efficiency it is essential to obtain the maximum possible supersonic compression. This is obtained with the least inlet contraction ratio that will start. For fixed geometry diffusers, this requires the use of a central body to compress the flow before it

enters the inlet. Diffusers without central bodies or other means of external compression are restricted so seriously by the starting problem that they are of no practical use at high Mach Numbers. Unfortunately, however, the compression produced by the central body is accompanied by a cowl drag. Since both drag and efficiency increase directly with flow deflection, it is necessary to optimize the diffuser design in terms of net thrust. Although this is somewhat more trouble than designing for a given burner velocity, it can be handled in a straightforward manner with existing methods.

An important feature of all supersonic diffusers is the existence of the supercritical regime that occurs when the inlet volume flow is a maximum for a given Mach Number. The "critical" point is simply the point of maximum compression efficiency in the supercritical regime and is the condition for maximum net thrust of a ram-jet. Operation of a ram-jet at the critical point is achieved by increasing heat addition in the burner until the shock system within the engine is moved upstream to the inlet. The shock losses within the diffuser are thus minimized, and the plenum chamber pressure is a maximum for supercritical operation. If further heat addition is attempted after this point has been reached, the diffuser enters the "subcritical" regime, and either one of two possible situations results. Either the flow remains steady, or flow breakdown occurs followed by a nonperiodic fill-up and discharge of the plenum chamber known as "buzz."

From a practical standpoint it is obviously important to know when this instability might occur, so that operation under these conditions can be avoided. It is the purpose of the present investigation to determine the nature and cause of this instability.

It should be observed that different kinds of transient flow processes may occur in ducts or in internal flow systems in general. Depending on the duct geometry and flow conditions, these phenomena are sometimes even qualitatively different. It would be unrealistic to expect a mechanism that accounts for instability in one case to apply to all instances of internal flow system instability. For example, it would not be expected that the well-known phenomena of compressor surge and the alternate stalling and unstalling of parallel ducts feeding the same plenum chamber could be explained by the same mechanism; nor would it be expected that axially symmetric supersonic diffusers with and without central bodies or scoop diffusers would necessarily exhibit the same transient flow characteristics. Furthermore, it should not be supposed that the mechanism that accounts for instability at a given mass flow, for a given diffuser operating at fixed Mach Number and Reynolds Number, would be the same for all other mass flows.

It is therefore emphasized that this investigation deals principally with the problem of determining the cause and nature of the instability that has been observed to occur in axially symmetric diffusers, with central bodies, operating at high subcritical mass flows. It is the occurrence of this instability which defines the lower limit of steady subcritical operation for such a diffuser.

The first mention of this phenomenon in the literature appears in an NACA translation of a German report by Oswatitsch describing experimental work performed by him in 1942.

He did not discuss the phenomenon in detail but merely observed its occurrence. In fact, he dismissed the subject with the remark that it was unimportant since the subcritical range was impractical anyway—an observation that is hardly realistic when one realizes that a sudden burst of instability might result in the failure of a supersonic ram-jet missile or destruction of a high Mach Number turbojet engine.

This phenomenon was again mentioned by Davidson and Umney in England in 1947, by Ferri and Nucci in 1948, and is compared to power-plant surge in general by Pearce. Stoolman gives a brief discussion of Oswatitsch's experiments and mentions similar results that he found in tests of the same size and type of model operated over the Mach Number range from 1.8 to 2.5. However, since Stoolman was concerned principally with the possibility of self-excited oscillations arising from the intrinsic character of the compression system in front of an open duct with low mass flow, he did not analyze the high mass flow instability for ducts with central bodies.

In spite of the fact that the occurrence of this phenomenon has been known for more than 10 years, it has not yet been adequately explained. The investigation described herein is presented in an effort to give a clear physical understanding of this process.

Discussion of Steady Operation

The essential features of steady supersonic diffuser performance can be shown quite effectively by the approximation of "one-dimensional" gasdynamics. Although the theory is simple and well known, it is reproduced in detail here for the intuitive feeling, or insight, which the derivation affords. An understanding of the different aspects of steady operation is helpful in gaining a physically clear picture of the instability.

The important features of a supersonic ram-jet engine with a central body diffuser are shown in Fig. 1.

Development of Steady Flow Theory

The relation between stagnation pressure ratio across the diffuser and mass flow is obtained directly from the condition of mass conservation. The rate of mass flow past any station is

$$m = \rho SM\sqrt{\gamma RT} = (PSM/\sqrt{T})\sqrt{\gamma/R}$$

where γ and R are specific heat ratio and gas constant, respectively. Mass conservation across the diffuser is therefore expressed as follows:

$$P_0 S_0 M_0/\sqrt{T_0} = P_2 S_2 M_2/\sqrt{T_2}$$

In terms of stagnation conditions, this can be written

$$\frac{P_{s_0}}{\sqrt{T_{s_0}}} S_0 M_0 \frac{\sqrt{T_{s_0}/T_0}}{P_{s_0}/P_0} = \frac{P_{s_2}}{\sqrt{T_{s_2}}} S_2 M_2 \frac{\sqrt{T_{s_2}/T_2}}{P_{s_2}/P_2}$$

Noting that diffuser flow is essentially adiabatic and solving for stagnation pressure ratio, one obtains

$$\frac{P_{s_2}}{P_{s_0}} = \frac{S_0}{S_2} \frac{M_0}{M_2} \frac{\sqrt{T_{s_0}/T_0}}{\sqrt{T_{s_2}/T_2}} \frac{P_{s_2}/P_2}{P_{s_0}/P_0} \tag{1}$$

But since this relation could also be applied between upstream and downstream sonic points, it follows that

$$P_{s_2}/P_{s_0} = S_{*_0}/S_{*_2} \tag{2}$$

The condition expressed by Eq. (1) therefore can be related to Eq. (2) by a tautology as follows:

$$P_{s_2}/P_{s_0} = (S_0/S_2) \frac{S_{*_0}/S_0}{S_{*_2}/S_2} \tag{3}$$

The area ratio, S_0/S_2, is a dimensionless expression of the mass flow entering the diffuser. In practice, it is convenient to refer the mass flow to the critical (or supercritical) value. Thus one writes the area ratio in terms of the critical capture area, S_{0_c}, as follows:

$$S_0/S_2 = (S_0/S_{0_c})\ (S_{0_c}/S_2)$$

The relative mass flow is now a measure of how close the diffuser is to its critical point. The remaining factor is a design constant specified for a given engine by such requirements as fuel–air ratio, combustion velocity, etc.

The mass conservation condition for a diffuser therefore results in the following relation:

$$\frac{P_{s_2}}{P_{s_0}} = \frac{S_0}{S_{0_c}} \left(\frac{S_{0_c}}{S_2}\right) \left(\frac{S_{*_0}/S_0}{S_{*_2}/S_2}\right) \tag{4}$$

Significant Features of Steady Diffuser Performance

A qualitative picture of diffuser performance as a function of relative mass flow can be obtained from Eq. (4) and general considerations based on the shock configurations in Fig. 2.

In the supercritical condition (Fig. 2a) and at a constant free-stream Mach Number, the mass flow is constant and the stagnation pressure ratio is fixed by the plenum chamber Mach Number. In this condition, the stagnation pressure ratio will increase as M_2 decreases (resulting from increased heat addition or reduced exit area). The maximum value is determined by the shock configuration for which the internal shock system is as near the inlet as possible.

If still more heat is added or the exit area is reduced further, the first shock of the internal system moves outside and intersects the cone shock; the entering mass flow is reduced by spillage in the subsonic region between the subcritical shock and the inlet. For the case shown in Fig. 2b, the shock system efficiency is about the same as for the critical mass flow condition. The overall diffuser efficiency increases slightly as the mass flow decreases because of reduced losses in the internal passage.

At low subcritical mass flows, the shock configuration shown in Fig. 2c occurs. The distinctive feature of this case is that some of the flow entering the diffuser passes through a single shock of the strong family. The entropy rise (or stagnation pressure loss) across this single shock is greater than that across the two shocks inside the intersection. The average stagnation pressure in the plenum chamber therefore decreases as the percentage of high entropy air in the inlet increases.

It can be seen on the basis of these qualitative considerations that diffuser performance for steady operation over a range of mass flows must be shown as Fig. 3.

The dashed line in Fig. 3 is the relation defined by Eq. (4) for constant exit area (hence constant M_2).

Discussion of Experimental Diffuser Characteristics

No mention has been made up to this point of the effect of unsteady operation. All the features shown in Fig. 3 have been explained in terms of steady diffuser flow. Although the occurrence in practice of such operation is rare, a few cases have been observed. An example is shown in Fig. 4a.

It is interesting to note that the essential features of the steady operation performance curve are the same as for unsteady operation or buzz. This is shown in Fig. 4b where unstable operation commenced when the higher entropy air first entered the inlet, so that the region of reduced efficiency corresponded to the unstable range of mass flows.

As noted in Fig. 4, the central bodies were slightly eccentric relative to the cowls. The fact that entrance of the high entropy air coincided with the onset of instability for one case and not for the other might be due to the difference in magnitude of this eccentricity. It also suggests that this event—i.e., entrance of high entropy flow—may, in some cases, result in instability. It is emphasized, however, that the data in Fig. 4a show that this condition alone cannot be sufficient for instability. The fact that it is not necessary is shown by the data in Fig. 5.

In each case, the stream tube surface passing through the intersection of the subcritical shock with the central body shock was outside the cowl when instability occurred. In Figs. 5a and 5c, the cone surface Mach Number was too low to allow branching of the strong subcritical shock near the surface; therefore no entropy discontinuities of any kind entered the inlet. These cases show that entrance of entropy discontinuities is not necessary for instability. For the diffuser shown in Fig. 5b, the high entropy air following the strong subcritical shock was well outside the cowl when instability occurred.

The linear relation for sonic exit velocity at the throttle area for which high entropy air first entered is shown in Fig. 4. Since the slope of the line in Fig. 4b is much greater than the steady performance curve,

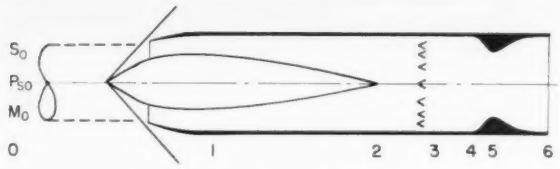

FIG. 1. Stations in a ram-jet.

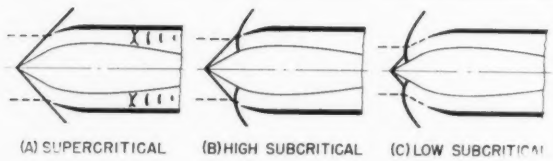

FIG. 2. Shock configurations under different steady-flow conditions.

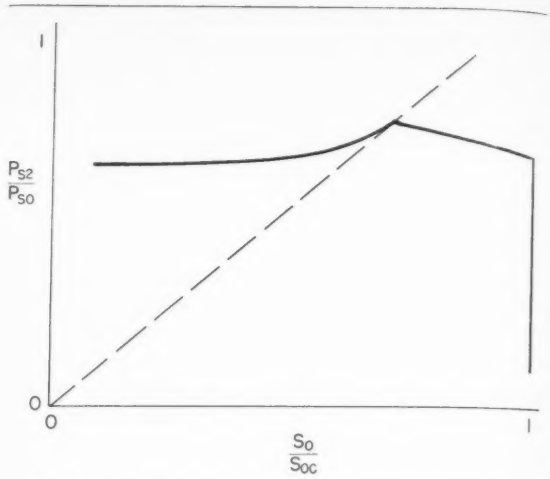

FIG. 3. Typical diffuser performance (steady operation).

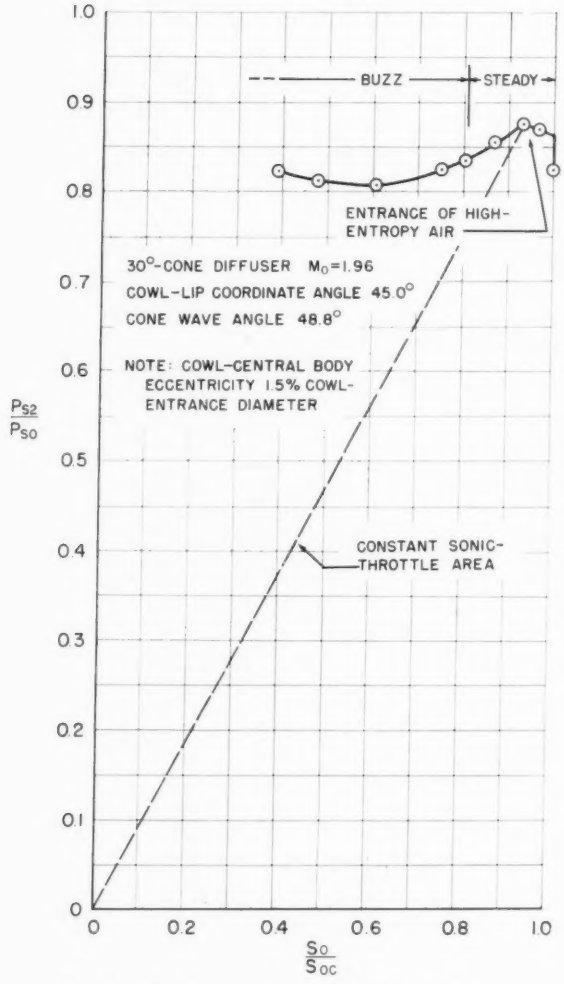

FIG. 4a. Steady operation with mixed inlet flow.

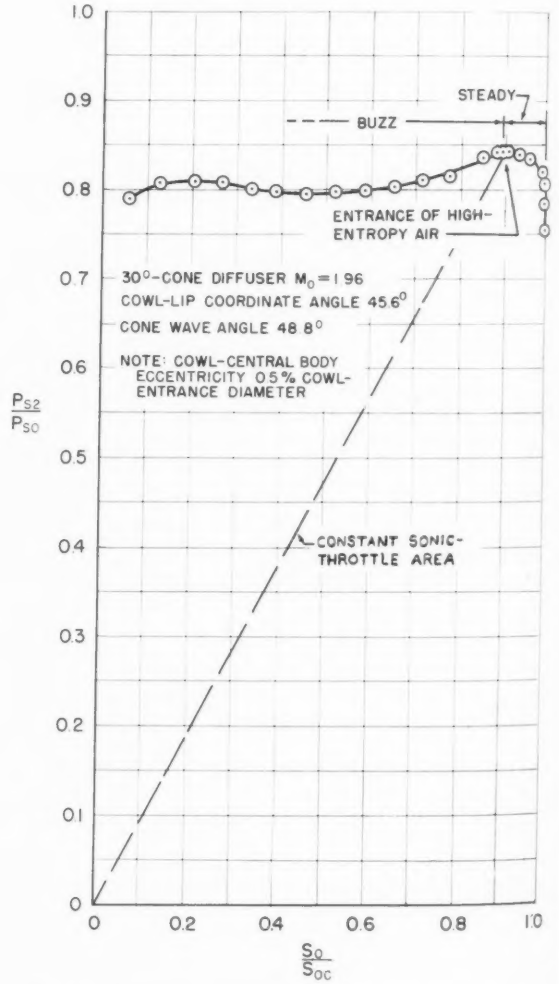

FIG. 4b. Unsteady operation coincident with mixed flow.

it is apparent that instability could not be caused by static divergence of the diffuser following entrance of the high entropy air.

The buzz phenomenon is easily recognized either by optical observation or by observation of plenum chamber pressure with a system capable of following high-speed transients. In wind-tunnel work, the easiest way to observe it is by either schlieren or shadowgraph observation of the diffuser shock system. The characteristic features of the oscillation are shown in Figs. 6 and 7.

The optical method not only easily detects the presence of buzz but also yields some understanding of the phenomenon. It can be seen in Fig. 6, for example, that the downstream limit of shock travel during the oscillation is the supercritical configuration. Another important observation is that the range of shock travel does not depend much on the average mass flow. In fact, by careful adjustment of the exit throttle, it is possible to set the mass flow so close to the transition point that several minutes can elapse between individual cycles without affecting the range of shock

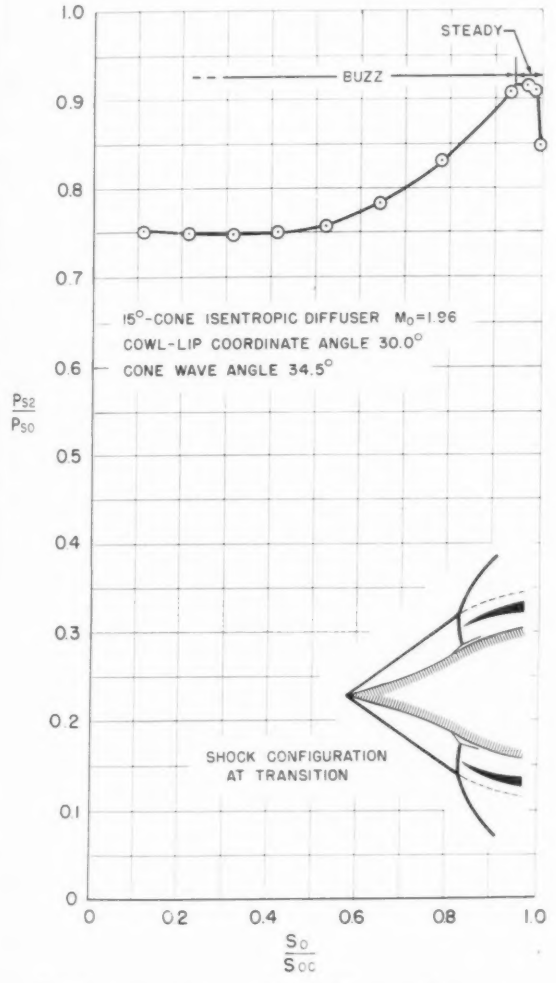

FIG. 5a. Isentropic central body diffuser performance.

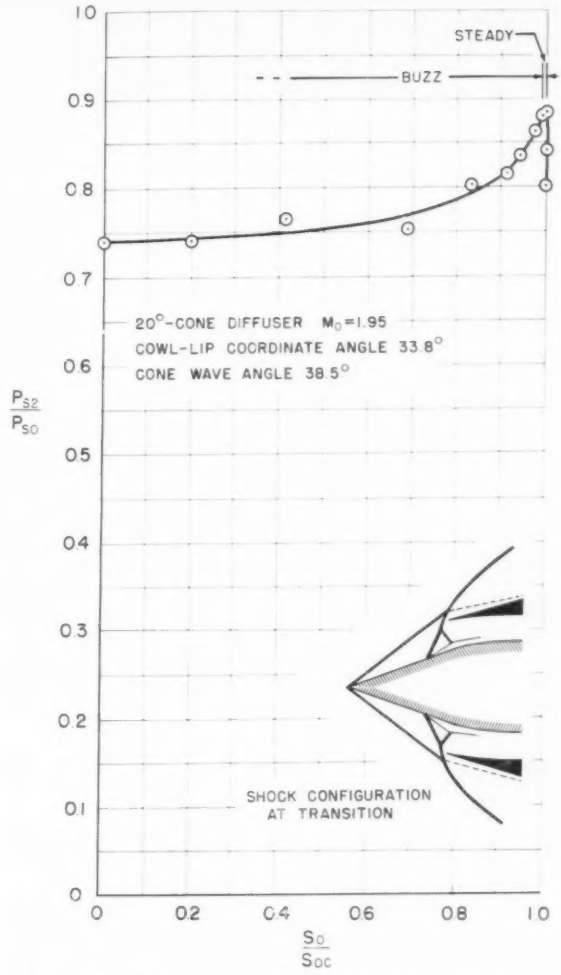

FIG. 5b. 20° cone central body diffuser performance.

travel. The interval between oscillations is random; the performance of the diffuser during this interval is the same as in the steady subcritical range above the transition point. By observation of the schlieren screen, the period of an isolated cycle can be seen to be on the order of 0.2 sec. or less.

Viewed by itself, this information—obtained simply by observation with conventional schlieren or shadowgraph methods—would be little more than suggestive; when combined with transient pressure measurements, however, a clear picture of the oscillation can be obtained.

DESCRIPTION OF MODEL AND EQUIPMENT FOR TRANSIENT FLOW TESTS

The model had a plenum chamber diameter of 5.25 in. and could be adjusted in length to 96, 120, or 140.4 in. by inserting cylindrical spools. It was equipped with pressure transducers located at three stations on the central body and at one station in the plenum chamber.

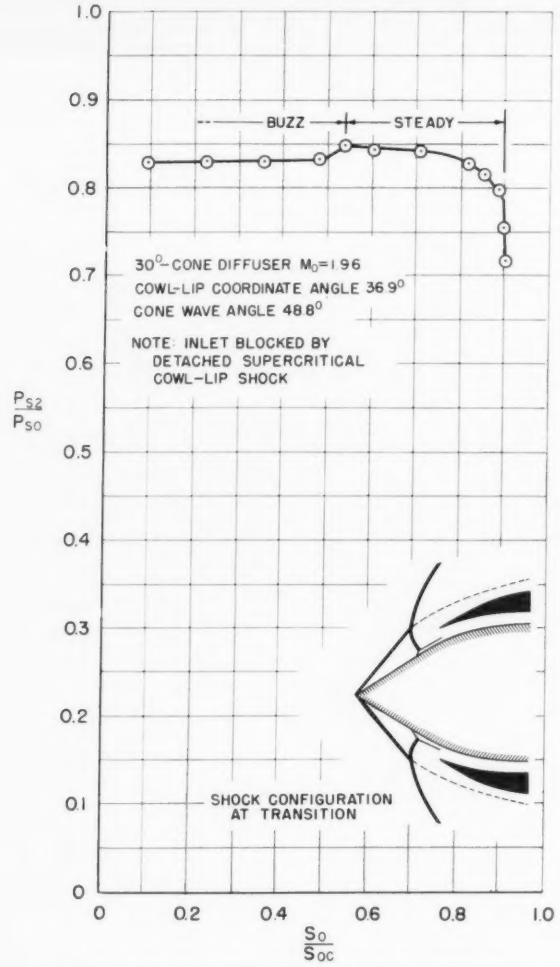

FIG. 5c. 30° cone central body diffuser performance.

Scale drawings of the model, showing the three lengths tested, and transducer stations are shown in Fig. 8. It had a 20° cone central body, a critical capture area at Mach Number 1.95 which was 27.7 per cent of the plenum chamber area, and a cowl lip coordinate angle of 33.8°.

Cold flow data for this diffuser are shown in Fig. 5b. It reached a critical point stagnation pressure ratio of 0.882 but had a transition point (from steady subcritical to buzz) at 99 per cent of critical mass flow.

The engine was equipped with a conventional can-type burner operating on gasoline fuel. It was installed for combustion tests in the 120-in. length engine only. The purpose of the combustion tests was to determine the influence of buzz on combustion, the effect of heat addition on buzz, and transient pressure variation during burning and blowout.

A standard Wiancko system was used for the pressure measurements. This consists of a carrier oscillator driving an a.c. bridge at 3,000 cycles per sec. The two active arms of the bridge consist of coils mounted in the transducer. The a.c. current resulting from an unbalance of the bridge is demodulated by a full wave crystal diode rectifier and used to drive the recording equipment, which for these tests was a Heiland oscillograph with 450 cycles per sec. elements. The flat response range of these galvanometers, with damping, was only 275 cycles per sec.

Oscillograph records are presented without reference to a pressure scale and are used for a qualitative analysis of the transient phenomena. The order of magnitude of pressure variation during buzz is shown in Figs. 12, 13, and 14.

The wind tunnel had a test section 17 by 20 in. in size and was operated nonreturn, without drying or temperature control. Air was supplied by a stand-by blast furnace compressor at the Kaiser steel mill located at Fontana, Calif. This wind tunnel was a part of the Fontana Aeronautical Laboratory operated by the University of Southern California Engineering Center until 1949. This facility has been relocated at NAMTC, Pt. Mugu, Calif. It is now known as the Aerodynamic Test Division and is still operated, under contract from Pt. Mugu, by the Engineering Center.

The nominal Mach Number of the tunnel was 2.00; during the test period it averaged 1.95 with a variation of ± 0.03 due to humidity effects. The stagnation temperature of the air stream averaged 200°F. with a variation of ± 25°.

Discussion of Experimental Results

Typical oscillograms are reproduced in Fig. 9, showing the effect of average mass flow through the diffuser on pressure fluctuations at the 4 transducer stations for the intermediate volume. Referring to the figure, vertical orientation of the traces down the page corresponds to downstream orientation of the transducers in the model. Vertical timing lines occur at 0.01-sec. intervals.

The important features of the oscillation are clearly shown in Fig. 9. At zero mass flow, all stations show the presence of a high frequency, periodic oscillation at about 600 cycles per sec. At 18 per cent of critical flow, the same high-frequency oscillation is apparent, but a different phenomenon has now appeared. A random oscillation with a much higher amplitude and longer period (about 0.035 sec.) now appears in addition to the high-frequency motion. At 41 per cent of critical flow, the long period motion is dominant; it is more nearly periodic, although still random, and the period has increased to about 0.040 sec. for an isolated cycle. The high-frequency motion is still present, although it occurs in bursts at intervals that show a consistent relation to the long period cycle. Its frequency is now about 700 cycles per sec. At 66 per cent of critical flow, the long period oscillation has acquired a wave form that is characteristic of this phenomenon for all higher mass flows between this value and the transition point.

It appears that the transient operation consists of a mixture of two intrinsically different phenomena. One is a high-frequency, periodic oscillation that occurs

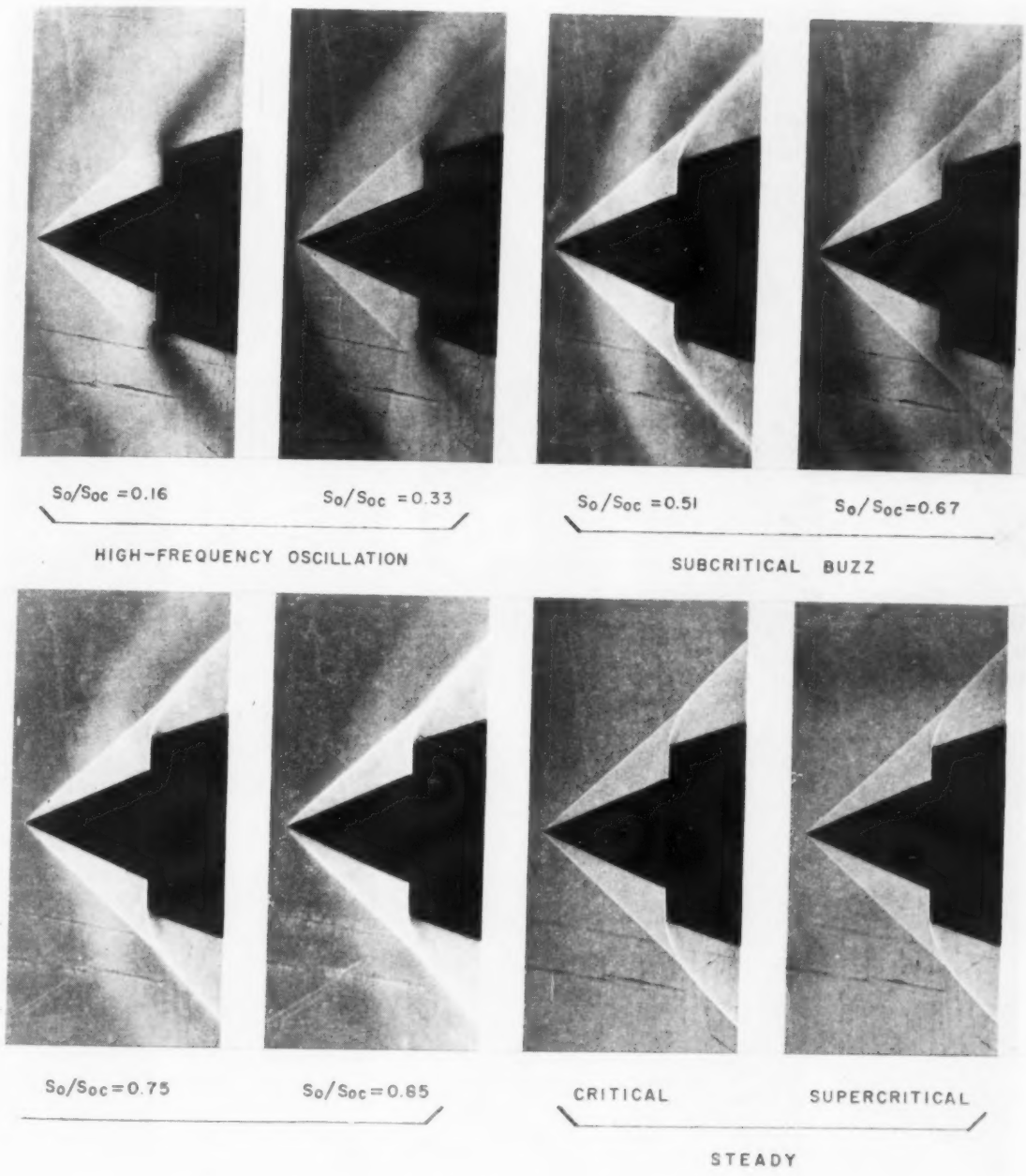

FIG. 6. Effect of mass flow on inlet shock system (25° cone, $M_0 = 1.91$).

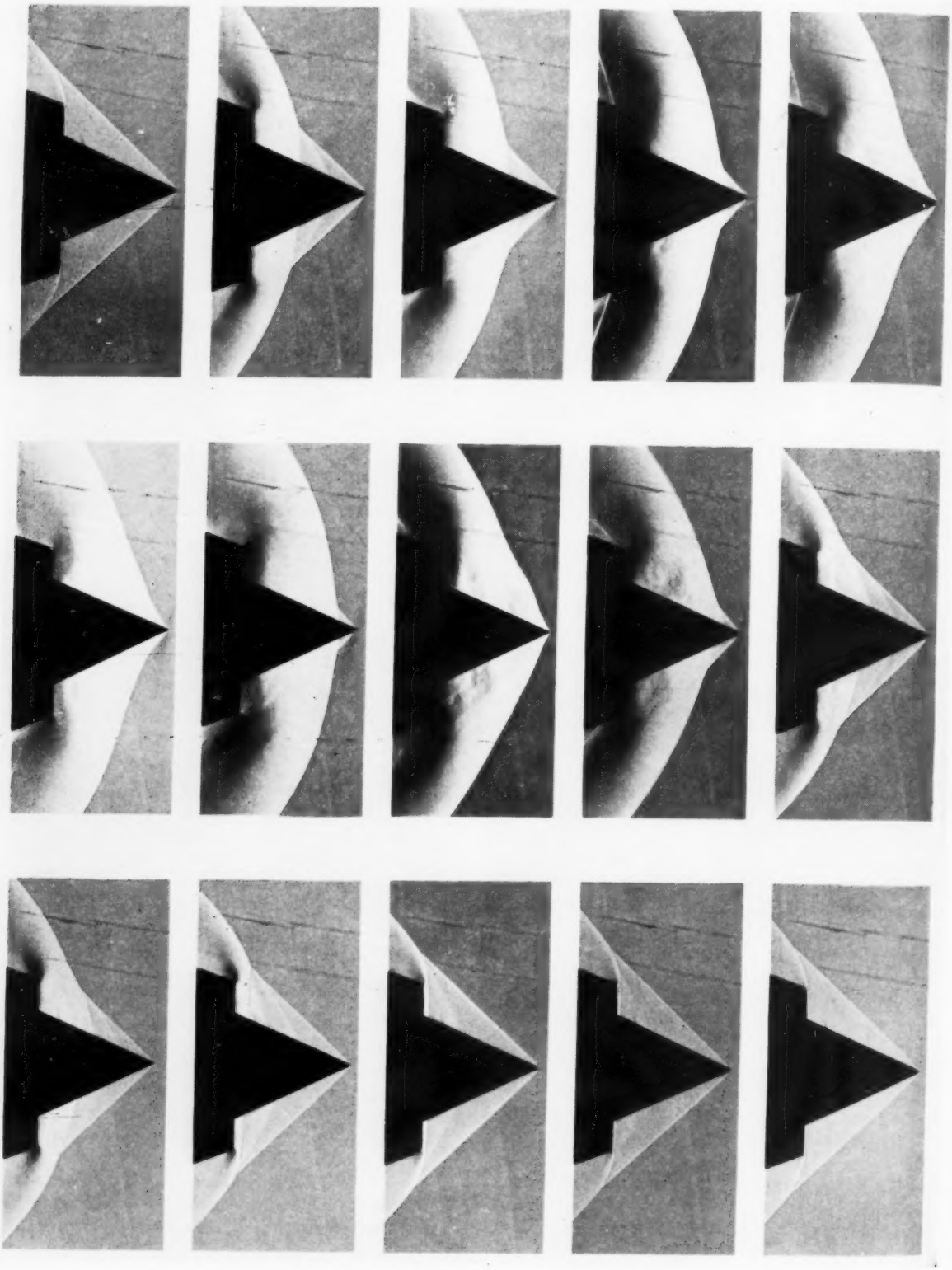

FIG. 7. Shock configuration during buzz (25° cone, $M_0 = 1.91$, 4-microsec. exposure).

without interruption only at very low flows. The other is a relatively long period motion with a fairly definite period for each cycle, depending on mass flow, but with a random time interval between cycles. Although the high frequency oscillation is present at all mass flows below the transition point, it is not actually superimposed on the long period motion. The long period motion blocks out the high-frequency oscillation over part of its cycle; the interval during which it is not blocked occurs consistently at the same phase of the long period motion.

Oscillograms showing the effect of plenum chamber volume on the transient pressures just below transition are presented in Fig. 10. The second trace from the inlet, for the smallest volume case, should be disregarded. The diaphragm of the transducer located at that station was broken during the run.

In addition to the transient pressure measurements, schlieren pictures of the inlet shock system were taken at a repetition rate on the order of 2,000 to 3,000 frames per sec. Although the resolution of these pictures was too poor to permit reproduction in this paper, significant observations based on them will be included in the following discussion.

The frequency of the shock motion during the high-frequency pressure oscillation at zero mass flow, determined by counting frames on the motion picture film, was found to be 607 cycles per sec. This agrees with the pressure record for zero mass flow in Fig. 9. The short burst of high-frequency oscillation noted above for high mass flows can also be seen in the motion picture data. The shock pulsation has the same appearance as in the zero mass flow case, but the frequency has increased to 690 cycles per sec.

Organ Pipe Oscillation at Low Mass Flow

Before proceeding with an analysis of the long period cycle, it is interesting to see how much can be said about the high-frequency motion.

The physical length of the small volume engine (from cowl lip to exit) was 7.83 ft., and the stagnation speed of sound was 1,260 ft. per sec. The exit nozzle for the high mass flow case consisted of a circular hole in a 1/2-in. thick flat plate. The only contraction from the plenum chamber diameter of 5.25 in. to the exit diameter of 2.53 in. was a conical frustum, formed by a 45° bevel in the 1/2-in. plate with its apex downstream. The downstream end of the plenum chamber was therefore essentially a flat plate with a small circular hole in the center occupying 23.2 per cent of the base area.

For the zero mass flow oscillation, the wave length is only 2.08 ft. Since the engine length is 7.83 ft., the theory of the Helmholtz resonator cannot be used to explain this high-frequency motion. It can, however, be accounted for in terms of wave propagation. Since the diffuser central body extends only 2 ft. downstream from the cowl lip, even the short engine must behave essentially like an organ pipe. At zero mass flow the

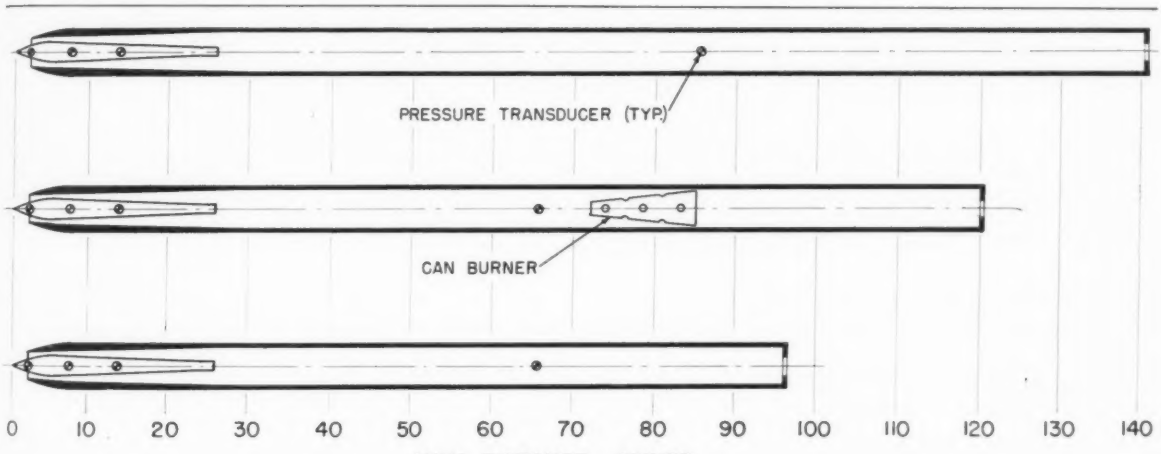

Central Body Coordinates				Cowl Coordinates			
				Inner		Outer	
X	Y	X	Y	X	Y	X	Y
2.664	0.968	7.000	1.120	2.154	1.440	2.154	1.440
2.736	0.992	8.000	1.100	2.304	1.468	5.875	2.510
2.808	1.016	9.000	1.075	2.592	1.520	7.000	2.750
2.880	1.035	10.000	1.040	2.880	1.566	8.000	2.885
3.024	1.067	12.000	0.965	3.168	1.606	8.500	2.925
3.312	1.107	14.000	0.900	3.600	1.650	10.812	3.000
3.600	1.131	16.000	0.835	4.032	1.680		
3.890	1.145	18.000	0.745	4.464	1.701		
4.176	1.151	20.000	0.650	2° slope to 2.625			
4.320	1.152	22.000	0.540				
4.464	1.152	24.060	0.437				
6.000	1.160	26.000	0.437				

FIG. 8. Model configurations.

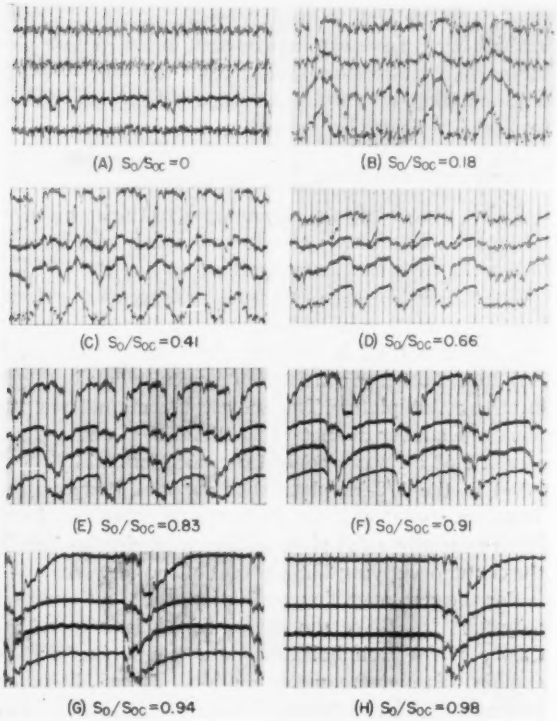

FIG. 9. Effect of mass flow on buzz (effective length, 8.93 ft.).

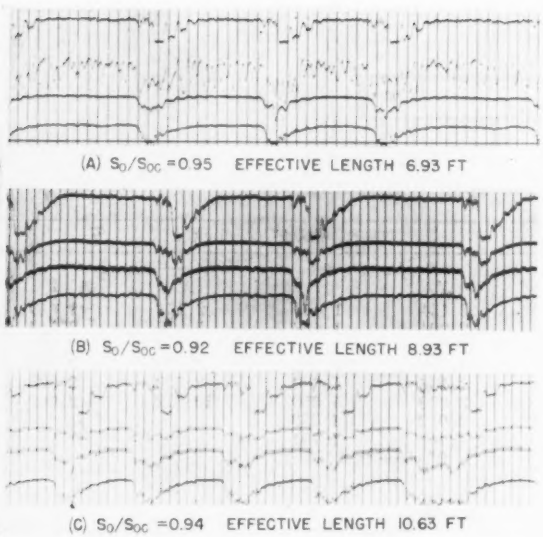

FIG. 10. Effect of plenum chamber volume on buzz cycle.

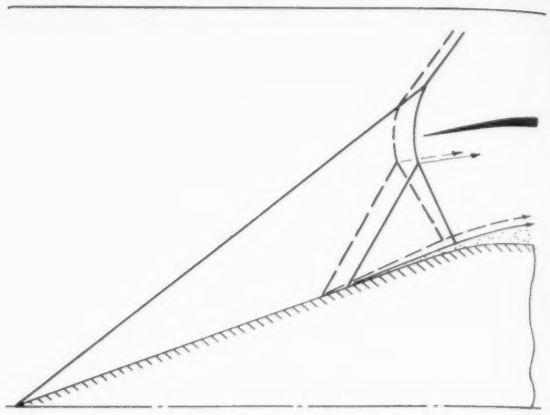

FIG. 11. Decreased effective inlet area due to upstream motion of shock.

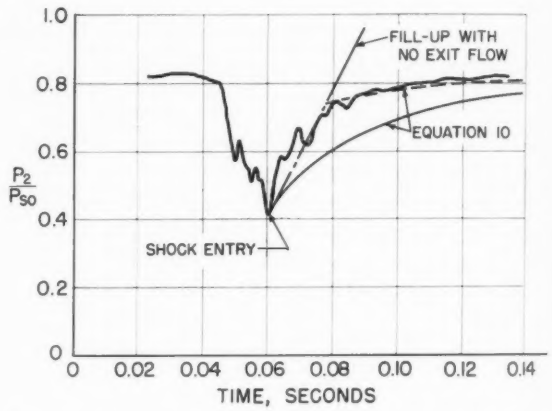

FIG. 12. Comparison of calculated and experimental fill-up time (effective length, 6.93 ft.).

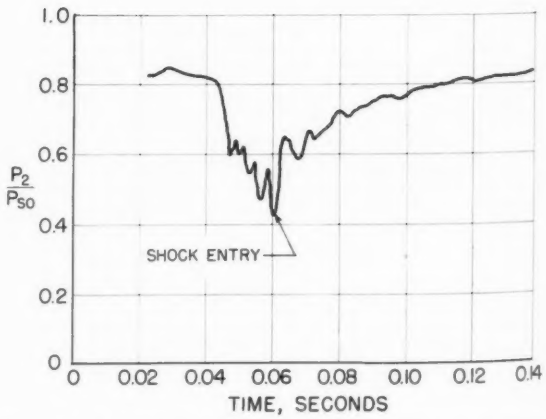

FIG. 13. Comparison of calculated and experimental fill-up time (effective length, 8.93 ft.).

TABLE 1
Comparison of Experimental and Theoretical Frequencies for Short Engine

Mass Flow	Experimental Frequency	Closed-End Mode	Organ Pipe Frequency
0	607	8	604
During buzz	690	9	685

exit is closed, and in the high subcritical range is only 23.2 per cent open. The reflection in the latter case is simply an attenuated wave of the same type as for the closed-end reflection. The experimental frequencies are compared to the eighth and ninth modes of a closed-end organ pipe in Table 1.

The fact that the oscillation is so far from the fundamental mode suggests that the frequency must be determined roughly by the driving mechanism. The actual frequency is then fixed by the nearest resonant mode of the pipe. The forcing function is not understood. However, a similar high-frequency oscillation has been noticed at low mass flows in tests on diffusers without central bodies. In both cases, the cowl leading edge has been sharp. This suggests vortex shedding from the cowl lip as the forcing function, as well as the frequency determining factor. It is not clear why the frequency should be higher when the exit is partially open, although this behavior seems to be characteristic of the oscillation.

Results similar to these have been observed on a small diffuser model tested at Mach Number 2. This model was only 1.89 ft. long, from the cowl lip to the exit, but its transient characteristics were qualitatively similar to those of the large engine.

Because of the small scale, the buzz (long period oscillation) had a much shorter period than that for the large engine, but the low mass flow oscillation had essentially the same frequency. At zero mass flow, the high-frequency oscillation occurred at 470 cycles per sec. At the test value of the stagnation speed of sound (1,160 ft. per sec.) the second mode of a closed-end organ pipe 1.89 ft. long is 460 cycles per sec. This note was clearly audible. As the mass flow was increased (below the buzz range), the note suddenly increased pitch by a little less than an octave, and the shape of the shock region in front of the inlet changed at the same instant. The actual frequency was not measured at the time. However, the third organ pipe mode is 767 cycles per sec. (a ratio of 5:3) which agrees with the observed change in pitch. Results of these two tests are summarized in Table 2.

TABLE 2
Comparison of Frequencies for Diffusers of Different Lengths

Diffuser Length, Ft.	Mass Flow	Experimental Frequency	Mode	Frequency	R_n (Based on Cowl Diameter)
7.83	0	607	8	604	0.72×10^6
7.83	>0	690	9	685	0.72×10^6
1.89	0	470	2	460	0.74×10^6
1.89	>0	<940	3	767	0.74×10^6

These data indicate there must be some forcing function relatively insensitive to frequency in the range from 400 to 800 cycles per sec., with the actual frequency determined by the nearest organ pipe mode. Since both frequency and Reynolds Number are essentially constant for all cases, it is suggested that vortex shedding from the sharp cowl lip might be the forcing function. It is felt that the experimental evidence justifies this as a reasonable hypothesis; verification of the vortex shedding mechanism through a separate experimental program would be necessary before it could be accepted, of course.

The main purpose of the present investigation, however, is to explain the long period buzz oscillation. Although an understanding of the high-frequency oscillation would be both interesting and valuable, it is not necessary for the present problem. It is sufficient to observe its presence during the phase of the buzz cycle in which the strong shock appears in front of the inlet.

Analysis of Buzz

It can be seen in Fig. 10a that the short burst of high-frequency oscillation for the short engine operating at high mass flow has a duration of about 0.018 sec. By counting frames in the motion picture record it is found that the strong shock is in front of the inlet for an interval of 0.0185 sec. This shows that the high-frequency burst, seen in the oscillograms just before the inlet pressure trace drops off, corresponds to the interval during which the strong shock is in front of the inlet. Events before and after this interval, shown on both the pressure record and schlieren film, can therefore be correlated.

From the film it can be seen that the diffuser shock system becomes supercritical immediately after the high-frequency oscillation stops. By counting frames, it is found that this persists for 0.036 sec., after which steady subcritical operation occurs for an arbitrary interval. As shown in Fig. 10, the supercritical interval appears as the low-pressure phase of the cycle for the trace nearest the inlet. This is graphically illus-

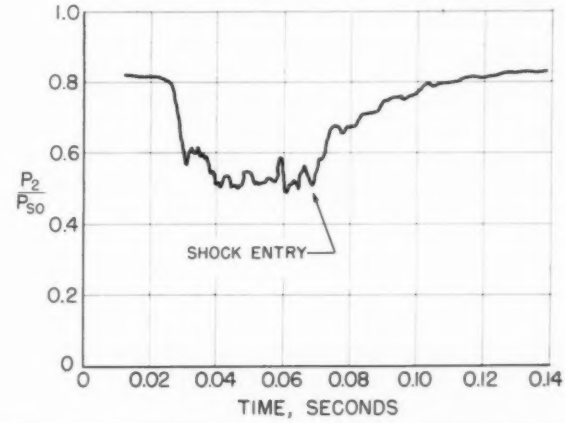

FIG. 14. Comparison of calculated and experimental fill-up time (effective length, 10.63 ft.).

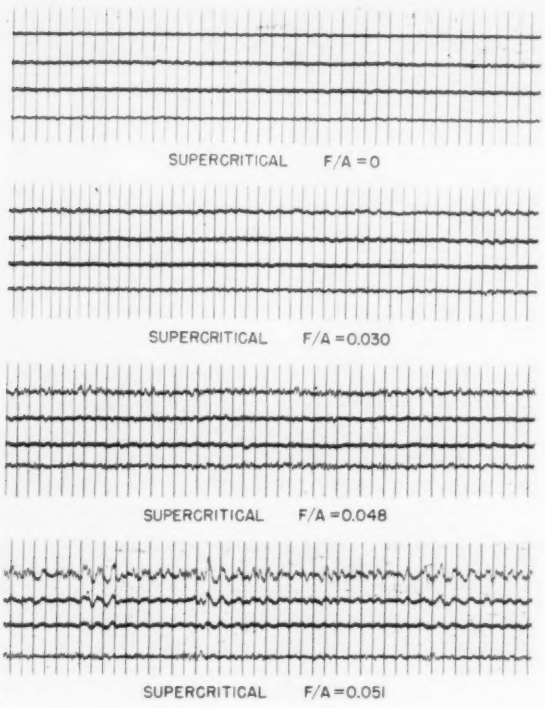

FIG. 15. Effect of fuel–air ratio on burning roughness.

trated by an interval of about 0.012 sec. during which the inlet shock is downstream of the first transducer station, and the local flow is supersonic. During this interval the pressure at this point is a minimum and is constant.

The total fill-up interval—i.e., the period of low pressure at the first station (Fig. 10a)—is about 0.050 sec. Apparently the inlet first becomes subcritical after 0.036 sec. and reaches equilibrium subcritical operation 0.014 sec. later at a slightly higher pressure. The buzz cycle has now ended; steady subcritical flow is established and persists for an arbitrary time interval before another cycle takes place.

The oscillation is evidently a series of relaxation cycles occurring at random intervals between which steady, equilibrium, subcritical operation occurs.

Steady subcritical operation is interrupted in some manner, following which the inlet shock moves to the tip of the central body, and the high-frequency oscillation—characteristic of low mass flow operation—sets in. While the inlet shock is oscillating, mass discharges from the plenum chamber with a corresponding drop in pressure. At the end of the high-frequency oscillation, the inlet shock moves into the diffuser and air enters at the supercritical rate. Because of the low plenum chamber pressure, the exit flow rate is less than the equilibrium value. The net inflow is therefore positive, and the plenum chamber pressure increases until the diffuser breaks down again. It has been found that, by careful adjustment of the exit throttle near the transition point, time intervals of several minutes between cycles can be observed.

With this qualitative description of the phenomenon in mind, a careful analysis of the pressure and schlieren data will now be made to determine the cause of the instability, the restarting process, and the nature of the fill-up phase of a typical buzz cycle.

It can be seen in the oscillograms that deviation from subcritical flow starts first near the inlet. The time scale is not large enough to permit accurate determination of the transducer that shows the first change in pressure. It is clear, however, that the three stations on the central body show a pressure drop before the plenum chamber station does. The plenum chamber Mach Number for this diffuser is 0.117 at the critical point. If this speed were added to the stagnation speed of sound (1,260 ft. per sec.), the time for a pressure wave to travel from the last central body station to the plenum chamber station would be found to be 0.003 sec., which agrees well with the data.

Following this initial pressure drop, the high-frequency oscillation sets in immediately. The time interval for the pressure drop cannot be determined accurately from these data, but for most cases it appears to be on the order of 0.002 sec. This means that the inlet flow changes from the steady subcritical condition to high-frequency oscillation in about 0.002 sec. This is much less than the time required for particle flow through the engine or for wave propagation from the inlet to the exit and back. At the plenum chamber Mach Number of 0.117, an interval of 0.053 sec. would be required for a fluid particle to travel from the inlet to the exit of the shortest engine. The wave propagation time for the same engine would be 0.012 sec.

Collapse of the inlet flow—i.e., from steady subcritical operation to the high-frequency oscillation—has been completed in one-third of the time required for an acoustic wave to reach the exit and before a fluid particle has had time to enter the plenum chamber. It must be concluded from this comparison that conditions in the plenum chamber have nothing to do with the breakdown of steady flow at the inlet—i.e., the break-

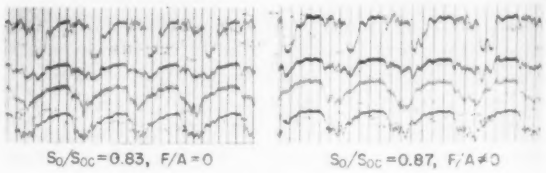

FIG. 16. Effect of burning on buzz cycle.

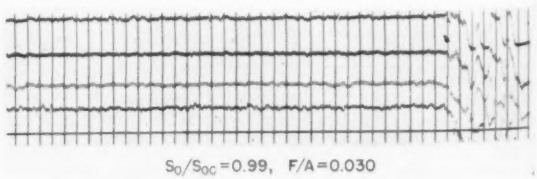

FIG. 17. Blowout in steady operation caused by diffuser instability.

down is so sudden that the way in which it occurs cannot be affected by conditions in the plenum chamber.

The question now arises as to whether conditions in the plenum chamber, just before the breakdown of the inlet flow, could be the cause of breakdown. Although the plenum chamber plays no role in the breakdown per se, it is possible that conditions in the plenum chamber preceding breakdown may have been sufficient to cause the instability.

Diffuser Separation as a Possible Cause

Consider the diffuser in a condition of steady subcritical operation, and suppose the central body flow were to separate suddenly at some point in the subsonic diffuser. The central body wake would increase, and the core flow velocity in the annular subsonic diffuser around the central body would also increase. As a result, the pressure at the plenum chamber transducer would decrease. If this flow were to mix completely in the plenum chamber before reaching the exit nozzle, the result would be a decrease in both the local pressure and stagnation pressure and a corresponding decrease in exit mass flow rate. Mass would therefore begin to accumulate in the plenum chamber which would result in a compression wave traveling upstream toward the inlet. The effect of this wave joining the inlet shock would be to move it upstream at the velocity required to match the increased pressure downstream of the shock. This motion might be unstable, beyond a certain amplitude, and result in collapse of the inlet flow.

If this argument were correct, one would expect to find a drop in pressure at the plenum chamber station as the expansion wave from the separation propagates downstream. Suppose, for example, that a separation occurred at the last central body transducer station for the shortest engine. The pressure would begin to drop at the plenum chamber station 0.0030 sec. later. Fluid from the separated region would reach the exit 0.046 sec. later, or 0.043 sec. after the plenum chamber pressure dropped. An upstream wave would then require roughly 0.007 sec. to reach the inlet. So one would expect to find a drop in pressure at the plenum chamber station about 0.050 sec. before the inlet pressure dropped. For the intermediate and long engines, corresponding values of this time would be 0.067 and 0.078 sec., respectively. Examination of the oscillograms in Figs. 9 and 10 shows that this argument must be completely inapplicable—the time intervals are too large by a factor of ten to be related in any way to the breakdown process. It follows, therefore, that the instability is not caused by a transient accumulation of mass in the plenum chamber following a loss in diffuser efficiency.

FIG. 18. Blowout in steady operation due to rough burning.

FIG. 19. Blowout during buzz due to buzz.

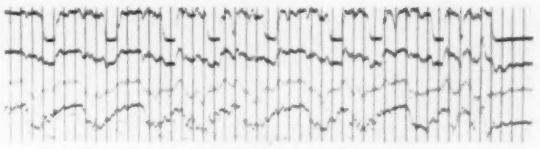

FIG. 20. Blowout during buzz due to rough burning.

Since the time interval required for particle flow is too long, the question arises whether diffuser flow separation could interact on the inlet flow through wave propagation in time to cause instability.

In the diffuser flow separation argument, it was observed that the exit flow would be reduced when the separated flow reached the exit nozzle. Actually, the reduction would begin earlier than this. As mentioned above, the immediate effect of a central body flow separation is a pressure decrease in the core flow, which is propagated into the plenum chamber as an expansion. As the fluid moves downstream from the separation point, a low-pressure region develops between that fluid and the separation point on the central body—i.e., the separated region grows at the particle flow rate—which means that expansion waves are generated continuously and move into the plenum chamber. Consequently, the exit pressure, and hence the exit flow rate, begins to drop when the first expansion wave from the separation reaches the exit and drops continuously for some time thereafter.

It might be argued that mass accumulation in the plenum chamber would begin when the first expansion wave from the separation reached the exit. In the order of increasing engine length, the time intervals required for acoustic waves to travel downstream from the plenum chamber transducer to the exit and back to the inlet are 0.0088, 0.0120, and 0.0153 sec., respectively.

If this phenomenon were responsible for breakdown of the inlet flow, one would expect to find a smooth drooping of the plenum chamber pressure traces beginning at these time intervals before the sharp drop in the central body traces takes place. Furthermore, the change in plenum chamber pressure should continue until the sharp pressure drop resulting from collapse of the inlet flow has had time to be felt at the

TABLE 3
Plenum Chamber Pressure Droop Intervals for Three Engine Lengths

Length Inlet to Exit, In.	Δt_1	Δt_2	$\Delta t_1 + \Delta t_2$
94	0.0088	0.0038	0.0126
118	0.0120	0.0038	0.0158
138.4	0.0153	0.0049	0.0202

plenum chamber station. In the order of increasing engine length these additional time intervals are 0.0038, 0.0038, and 0.0049 sec., respectively.

If the separation argument in this form was correct, one would expect to find the following situation: The plenum chamber pressure trace should begin to drop at a time interval, Δt_1, before the sharp drop representing collapse of the inlet flow, and should continue to change for an additional time interval, Δt_2, before the sharp drop from the inlet has reached the plenum chamber station. In the order of increasing engine length, these time intervals are summarized in Table 3.

Examination of the pressure data in Figs. 9 and 10 shows these time intervals to be too large by about a factor of two. Furthermore, it should be noted that the shape of the plenum chamber pressure trace is not quite right. Since it is argued that collapse of the inlet flow is due to upstream propagation of a pressure wave resulting from mass accumulation in the plenum chamber, one should expect to find some evidence of a pressure rise following the initial drop in the plenum chamber transducer trace. Examination of the data shows this does not occur.

Instability Caused by Blocked Inlet Flow

Another approach to the instability problem can be made on the basis of a consideration of inlet flow conditions alone. In this argument, the plenum chamber is not a factor in causing instability, it simply reflects the history of the breakdown within the inlet as the complete picture, from beginning to end, is propagated through the plenum chamber.

Flow in the inlet of a diffuser is far from the idealized concept of a normal shock followed by uniform subsonic flow. In reality, it is similar to the shock system in a wind-tunnel diffuser, in which transition to subsonic flow is accomplished through several shocks. The first shock of the train has the characteristic lambda form of a strong shock–boundary-layer interaction. Near the surface, the flow is separated by an oblique shock of the weak family, which forms a Mach reflection with a strong shock covering the remainder of the entering flow.

The Mach Number of the flow approaching the branch point is roughly 1.59, and since the downstream flow is subsonic the intersection will presumably be defined by the condition of maximum downstream pressure. The maximum pressure ratio across the lambda shock occurs when the strong shock is normal to the flow. The geometry of this shock for Mach Number 1.59 is shown by the solid lines in Fig. 11 for a flow direction of 10° upstream from the intersection point. The deflection of 2° across the oblique shocks is shown as a separation of the cone surface flow which creates a dead water region at the minimum area of the inlet and reduces the effective area available for the entering flow.

A random pressure pulse arriving at this lambda shock from downstream would increase the downstream pressure above the equilibrium value for the shock. Since the strong shock ascending from the Mach reflection is normal, it would have to assume an upstream velocity to match the increase in pressure. Calculation of the shock intersection problem for the moving shock shows a corresponding increase in deflection angle across the oblique shocks. An increase of 10 per cent in pressure ratio across the normal shock would result in an upstream shock velocity that is 15 per cent of the local sonic speed and an increase in surface flow separation angle from 2° to 5°. The moving shock is shown by the dashed lines in Fig. 11.

As long as the stream line approaching the cowl lip passes through the normal shock, the entering mass flow is essentially unaltered. However, as a result of both the forward motion and the increased separation angle, the effective inlet area available for that mass flow decreases as the shock moves forward.

If a random pressure pulse from downstream has sufficient strength to move the lambda shock far enough forward to block the inlet, mass will accumulate in the inlet, and the subsequent pressure rise will force the shock to diverge to the cone tip. As the forward velocity of the shock increases, the separation angle increases also. At some point, the deflected flow by-passes the entrance entirely, and the entering flow is cut off. Spark pictures of the shock during divergence have shown surface flow deflection angles as large as 17°.

As a result of the abrupt interruption of the flow, the moving air column within the diffuser creates a sharp pressure drop at the inlet which then propagates downstream through the engine.

The time for divergence of the shock, measured by counting frames on the motion picture record, is 0.0022 sec., which agrees well with the interval of 0.002 sec. required for the abrupt drop in inlet pressure in Figs. 9 and 10.

This argument would explain why the buzz cycles occur more frequently as the mass flow is reduced. Since the average position of the inlet shock moves forward with decreasing mass flow, a weaker pulse is capable of blocking the inlet. Thus a shorter interval of steady operation is possible, on the average, before such a pulse occurs.

The question now arises as to why the plenum chamber pressure droops about 0.005 sec. before the inlet pressure begins to drop. An acoustic wave requires 0.0038 sec. to travel from the inlet to the plenum chamber station (for the two shorter engines). This means that if the plenum chamber pressure droop were caused by something in the inlet, it would have started

0.0088 sec. before the sharp pressure drop at the inlet occurred. It appears, therefore, that the inlet blocks for about 0.0088 sec. before the entering flow is deflected sufficiently by the advancing shock to by-pass the entrance.

To recapitulate, the instability develops as follows: First, the inlet shock is pushed upstream by a random pressure pulse from downstream until the inlet blocks. Some of the mass that enters the cowl begins to accumulate upstream of the point of blockage. The pressure in that region rises and results in a forward motion of the subcritical shock. This motion is unstable and continues until the flow by-passes the cowl lip. After the entering flow has been cut off, the momentum of the air column in the diffuser sustains its downstream motion for awhile and results in a low-pressure region at the inlet. At the same time, the mass flow entering the diffuser begins to decrease as soon as the inlet blocks and continually decreases as the blocking progresses. The pressure downstream of the blockage point therefore begins to drop as soon as the inlet blocks. It appears from the pressure and high-speed schlieren data that the entering flow is cut off about 0.009 sec. after the inlet blocks, and about 0.002 sec. later the shock has advanced to the cone tip and the high-frequency oscillation has set in.

If blockage of the inlet occurred downstream of any of the central body transducers, one would expect to see a pressure rise at that point coincident with a drop in pressure at the nearest downstream station. A good illustration of this can be seen in Fig. 9h. The three downstream transducers begin to droop at the last timing line before the sharp drop occurs, but the first transducer shows a rising pressure in this same time interval.

Of the three arguments given above, the last seems the most plausible and is in agreement with the high-speed schlieren and pressure data. It is believed that this explanation is correct.

Apart from acting as the source of random disturbances, the subsonic diffuser and plenum chamber have nothing to do with the occurrence of instability. The breakdown is a local condition in the immediate entrance of the inlet.

Mechanism of Restarting Supercritical Flow

The initial pressure drop and subsequent high-frequency oscillation have now been identified. Both the schlieren and pressure records show an average duration of about 0.02 sec. for the high-frequency oscillation or about 14 cycles at 700 cycles per sec. During this time, the entering flow is cut off, and mass discharges from the plenum chamber through both the exit and the inlet.

Referring again to the pressure traces in Figs. 9 and 10, the next significant event is a large drop in inlet pressure caused by restarting of supercritical flow. Since the plenum chamber pressure is low when this occurs, the inlet flow is supersonic past the first central body station and remains supersonic for about 0.012 sec. As mass accumulates in the plenum chamber, the pressure rises, and the shock moves upstream toward the inlet. The traces at all stations show steadily rising pressure during this fill-up phase of the buzz cycle. The pressure increase in the plenum chamber is essentially due to the increase of stored mass as the diffuser approaches equilibrium mass flow. The pressure at the first station is the local static pressure at that point within the shock region, and it, therefore, increases as the shock moves upstream.

It is interesting to note how well the downstream stations reflect the history of the breakdown at the inlet—from the initial pressure drop when the inlet blocks through the high-frequency oscillation.

The immediate effect on plenum chamber pressure of the inlet restarting appears to be a sharp rise in pressure. It can be seen in the pressure records (particularly in Figs. 9f, 9g, and 10b) that this is recorded at approximately the same time the abrupt drop in inlet pressure occurs which seems to imply that the plenum chamber responds to restarting of the inlet instantly instead of at the acoustic wave interval of 0.0038 sec. The reason for this apparent inconsistency is shown partly by the pressure trace at the last central body station and partly by the high-speed schlieren data.

The traces at both the last central body station and the plenum chamber station show the same pressure jump as the inlet restarts, and the events are separated by the proper acoustic interval of 0.003 sec. Since the inlet pressure drop, as supersonic flow starts over the first central body transducer, coincides with the plenum chamber pressure jump, this means that the inlet must make an impulsive effort to restart about 0.0038 sec. before it becomes completely supercritical.

Examination of the schlieren motion picture record shows this to be correct. The high-frequency oscillation of the inlet shock continues until supercritical flow has started. Transition from the oscillation to supercritical operation occurs during the last three cycles of the oscillation, which is 0.00435 sec. at 690 cycles per sec. The first motion of the shock toward the inlet occurs at the downstream limit of the excursion, and entrance of the shock occurs at the same phase of the oscillation three cycles later.

The jump in plenum chamber pressure corresponds to the first impulsive entrance of mass into the inlet and the inlet pressure drops when supercritical flow is established three cycles later. Air in the inlet acts like a pump that delivers three impulsive surges to the internal air column to get it moving fast enough to allow the inlet to become supercritical.

Calculation of Supercritical Plenum Chamber Fill-Up

After the inlet has become supercritical, a simple approximate calculation of fill-up time can be made, based on engine volume and the known rates of flow in the inlet and out the exit. In addition to the usual assumption of one-dimensional gasdynamics, the plenum chamber pressure is assumed to be uniform and equal to the value given by the thermal equation

of state for the mass of air in the engine, to be at rest filling the entire engine volume, and to be at the upstream stagnation temperature.

Mass flow, m, through a sonic area, S_*, can be expressed in terms of stagnation pressure and temperature as follows:

$$m = \left[\left(\frac{\gamma+1}{2}\right)^{\frac{-(\gamma+1)}{2(\gamma-1)}}\sqrt{\frac{\gamma}{R}}\right] S_* \frac{P_s}{\sqrt{T_s}} \tag{5}$$

The time rate of mass accumulation within the engine is the difference between the inlet and exit flow rates.

$$\frac{dm}{dt} = \left(\frac{\gamma+1}{2}\right)^{\frac{-(\gamma+1)}{2(\gamma-1)}}\sqrt{\frac{\gamma}{R}}\frac{1}{\sqrt{T_{s_0}}}\left(S_{*_0}P_{s_0} - S_{*_2}P_{s_2}\right) \tag{6}$$

$$= V(d\rho_{s_2}/dt)$$

where V is the total internal volume of the engine. By use of the thermal equation of state, the density derivative can be written as follows:

$$d\rho_{s_2}/dt = (1/RT_{s_0})\,(dP_{s_2}/dt) \tag{7}$$

On substitution of Eq. (7) in Eq. (6), one obtains

$$\frac{dP_{s_2}}{dt} = \left(\frac{\gamma+1}{2}\right)^{\frac{-(\gamma+1)}{2(\gamma-1)}}\frac{\sqrt{\gamma RT_{s_0}}}{V}\left[S_{*_0}P_{s_0} - S_{*_2}P_{s_2}\right] \tag{8}$$

If an effective length, l, is defined such that

$$V \equiv S_2 l$$

Eq. (8) can be written as

$$\frac{d\,(P_{s_2}/P_{s_0})}{dt} = \left(\frac{\gamma+1}{2}\right)^{\frac{-(\gamma+1)}{2(\gamma-1)}}\frac{a_{s_0}}{l}\times \left[\left(\frac{S_*}{S}\right)_0\frac{S_0}{S_2} - \left(\frac{S_*}{S}\right)_e\frac{S_e}{S_2}\frac{P_{s_2}}{P_{s_0}}\right] \tag{9}$$

where subscript, e, refers to the model exit. By introducing $\gamma = 1.400$ and rearranging Eq. (9), one obtains

$$\frac{d(P_{s_2}/P_{s_0})}{dt} + \frac{1}{(1.2)^3}\frac{a_{s_0}}{l}\left(\frac{S_*}{S}\right)_e\frac{S_e}{S_2}\frac{P_{s_2}}{P_{s_0}} = \frac{1}{(1.2)^3}\frac{a_{s_0}}{l}\left(\frac{S_*}{S}\right)_0\frac{S_0}{S_2} \tag{10}$$

Eq. (10) has a simple exponential solution if the exit Mach Number is constant. However, since the plenum chamber pressure is low at the beginning of fill-up, the exit Mach Number may be subsonic during the initial part of the fill-up period. In the present case, the engine extended so far into the wind-tunnel diffuser that its exit Mach Number was always subsonic, and Eq. (10) was integrated numerically.

The result of this calculation is compared with a typical plenum chamber pressure-transducer curve in Fig. 12 for the short engine. If the integration constant is chosen such that the calculated and experimental pressures coincide at the beginning of the sharp pressure rise at the plenum chamber transducer, it can be seen that the calculated pressure rise is significantly less than the experimental curve. The best that can be done to bring the calculated and experimental curves into agreement, within the framework of this simple fill-up theory is to assume no exit flow during the initial phase of fill-up. This gives the linear pressure rise shown in Fig. 12 which is still less than the data for the first 0.01 sec.

It appears, from this comparison, that the assumption of uniform density throughout the engine is not entirely satisfactory. Immediately after supercritical flow has been re-established, the net rate of mass influx is a maximum. The incoming air rushes into the mass of air at rest in the engine which, although it is compressed, confines the incoming air to a region near the inlet. The initial pressure rise therefore corresponds to fill-up in the forward section of the engine rather than the entire plenum chamber. The subsequent fill-up consists of air entering at a fixed rate but being diverted in a nonuniform manner to various regions of the plenum chamber as the rather strong compression waves shown in the data are propagated back and forth in the engine. A more accurate calculation of pressure variation at the transducer station could be made by the method of characteristics, but it is felt that the simple fill-up model used here describes the essential feature of the phenomenon with sufficient accuracy for the present purpose.

The description of the buzz phenomenon is now complete. Steady subcritical operation is interrupted by choking of the inlet which causes the subcritical shock to move forward to the cone tip and thus deflect the approaching flow outside the cowl lip. As the stored mass discharges out both ends of the engine, the engine resonates at the ninth mode for a closed-end organ pipe of the same length as the engine. As the discharge out the inlet decreases, the oscillating shock moves toward the inlet and—after three cycles—is completely swallowed, and supercritical flow is established. The inlet flow rate is then greater than the exit discharge rate, and the plenum chamber fills up in an approximately exponential manner until the shock moves out of the inlet and returns to the initial equilibrium subcritical operation condition.

This explanation of the buzz phenomenon is applicable for diffusers with fill-up periods that are long in comparison with the period of either the Helmholtz oscillation or the fundamental closed-end organ pipe oscillation, whichever is greater. If the fill-up period is near the period of either of these modes, the relaxation form of the buzz cycle will be distorted by dynamic effects; and if it is less than either of these periods, the corresponding mode will appear in place of the relaxation cycle even though the downstream limit of the shock travel is still supercritical. The phenomenon is then similar to buzz with respect to the forcing mechanism, but the period is determined by the mode (Helmholtz or organ pipe) rather than by fill-up time.

Effect of Combustion

With the explanation of the buzz phenomenon established, it is interesting to see what effect burning has

on the buzz and also what effect the buzz has on burning.

The engine used gasoline fuel and employed a conventional can-type burner. Ignition was accomplished with a spark plug and hydrogen pilot jet. The pilot jet and spark were shut off after ignition of the main burner. The data presented, therefore, describe the operation of the gasoline burner alone and are not influenced by re-ignition from the pilot jet.

A comparison of burner roughness at various fuel–air ratios is presented in Fig. 15. Since these tests were made with a fixed exit area, the effect of increasing fuel flow was to move the internal shocks nearer the inlet and decrease the degree of supercritical operation. It is possible, therefore, that some of the observed increase in roughness may have been due to changing conditions within the diffuser, as well as to increasing burner roughness. If the effect of fuel–air ratio alone were desired, it would be necessary to control the exit area with changing fuel–air ratio so as to hold constant diffuser conditions.

A comparison of cold flow and hot flow buzz is shown in Fig. 16. It is apparent that heat addition does not alter the essential features of the buzz cycle. On the other hand, it is obvious that buzz affects burning, since the airflow through the burner varies from nearly zero to the supercritical rate during the cycle.

In most cases, it was found that the extreme variations in plenum chamber conditions resulting from buzz were too severe to allow the burner to continue operating. The only way buzz during burning could be obtained was by increasing the fuel–air ratio slowly after steady burning was established. In most cases, the burner would blow out immediately when buzz started. Roughly 20 tries were made before a single burning buzz was obtained.

Fig. 17 shows a case of blowout caused by the first part of a buzz cycle. The droop following blocking of the inlet, the sharp pressure drop occurring when the inlet is by-passed, the high-frequency oscillation, and the entrance of the supercritical shock can all be identified. In fact, it is interesting to note how well this record shows the presence of blocking between the first and second transducer stations. The first central body trace rises for about 0.01 sec. before the inlet is by-passed, and the other two central body traces droop during the same interval. The plenum chamber droop starts about 0.005 sec. later and has the same duration as the central body traces.

The blowout shown in Fig. 18 was due to rough burning at supercritical mass flow. The pressure fluctuations at the transducer nearest the inlet are due to the shock motion resulting from pressure pulsations in the plenum chamber. The blowout appears to occur in two explosions; the second is much more violent than the first. The upstream propagation of the explosion waves is clearly evident in the pressure traces. The second explosion was strong enough to blow the supercritical shock out of the diffuser, following which the high-frequency oscillation occurred for about 0.004 sec.

Similar cases of blowout due to buzz and to rough burning are shown in Figs. 19 and 20 where buzz occurred during burning. In Fig. 19 the burner simply quit during the high-frequency oscillation. When supercritical flow was re-established, the flame was out, and steady supercritical cold flow ensued.

In Fig. 20 rough burning appears to occur just after fill-up. Apparently the heat release drops off, increases, decreases, and then increases in the form of an explosion. This entire pattern has a definite upstream propagation and clearly originates in the plenum chamber.

Changes of Address

Since the Post Office Department does not as a rule forward magazines to forwarding addresses, it is important that the Institute be notified of changes in address 30 days in advance of publishing date to ensure receipt of every issue of the JOURNAL and REVIEW.

Notices should be printed legibly and sent directly to:

Institute of the Aeronautical Sciences, Inc.

2 East 64th Street, New York 21, New York

The Stability of Vortex Streets with Consideration of the Spread of Vorticity of the Individual Vortices

ULRICH DOMM*

Hermann-Foettinger-Institute, Technical University at Berlin-Charlottenburg, Germany

SUMMARY

This investigation concerns the stability of vortex streets consisting of two parallel rows of staggered real vortices of identical structure whose vorticity spreads with time into the ambient fluid. It is found that for the case of stability the ratio of centerline width and pitch of the street is a function of the nondimensional time $\tau = (4\nu/l^2)t$, where ν = kinematic viscosity, l = pitch of the vortex street, and t = time. For vanishing viscosity and also for vanishing time, the value calculated by von Kármán, $k = h/l = 0.281$, is obtained.

(1) Introduction

In his basic paper on the stability problem of vortex streets, von Kármán[1] treated a two-dimensional infinitely long vortex street in an ideal fluid in which the vortices are arranged on two parallel straight lines. He obtained the well-known result that only streets with staggered arrangement of vortices are stable and that this is the case for one condition only—namely, when the quotient of width h to pitch l of the street has the value $k = h/l = 0.281$.

Deviations from this result observed by various investigators were explained by Hooker[2] by the observation that these are due to differences between the theoretically assumed and the actual velocity distribution, the latter corresponding to that of real vortices. If this error is corrected according to Hooker, it appears, on the basis of Hooker's experimental data, that k first decreases slightly with time and that later it assumes values considerably larger than $k = 0.281$. In a previous paper, the author[3] has calculated the influence of the real velocity profiles upon the stability of the single-row vortex streets and of the double-row street with vortices, arranged oppositely as well as staggered, for the special case of perturbation of only one single vortex. The single-row street was found to be unstable. For the double-row vortex street, regions of stability were found to exist in the k, τ-plane where $k = h/l$ and τ = the nondimensional time already referred to. In the present paper, the vortex street with staggered arrangement will be treated for the case of a perturbation displacement of all vortices.

A considerable number of research papers have appeared concerning vortex streets, and these have been reviewed recently by Rosenhead[4] in a comprehensive and stimulating treatise.

Received November 5, 1954.

* Engineering Research Associate.

(2) Basic Assumptions

According to Hamel[5] the spread of a vortex in plane real flow may be defined in terms of the kinematic viscosity ν, the time t, the circulation at time zero Γ_0, the radius vector γ, and the azimuthal velocity component c_φ as follows

$$c_\varphi = [\Gamma_0/(2\pi\gamma)]\,(1 - e^{-\gamma^2/(4\nu t)}) \qquad (1)$$

For sufficiently large r and constant t, c_φ deviates an arbitrarily small amount from the ideal profile $c_\varphi = \Gamma_0/(2\pi\gamma)$. For small values of r the relation

$$c_\varphi \approx [\Gamma_0/(8\pi\nu t)]\gamma \qquad (2)$$

is valid—i.e., there exists a linear increase of c_φ with the radius. The core of the vortex rotates approximately like a solid body.

For the subsequent stability investigation let us use the velocity profile, Eq. (1). To establish the equation of motion it will be necessary to sum over all individual vortices. Strictly this superposition is not permissible because of the quadratic terms of the Navier-Stokes equation. These vanish for the case of the single vortex in an infinite field of flow but not in the case of disturbed axial symmetry. Let it be assumed that for small ratios of core radius to pitch of the street—i.e., for small values of τ—the center region of the vortex may be regarded by approximation as isolated. In the vicinity of the vortex cores, recourse is made to the velocity distribution decreasing with $1/\gamma$ with consequent disregard of the quadratic members. The ensuing theory may be expected therefore to give results at large Reynolds Numbers approximately correct for small time intervals and, at small Reynolds Numbers, valid also for larger intervals.

(3) Equations of Motion

Consider a vortex street, Fig. 1, produced at time $t = 0$ in the real fluid. This is the model of the vortex street treated by von Kármán. In addition let it be assumed that under the action of viscosity the vorticity of all vortices spreads with time into the ambient fluid at the same rate for all vortices. The question arises whether there exists a function $k = k(\tau)$ such that small impressed perturbations of the vortices remain prescribably small with respect to the original location of the vortices on the parallel straight lines.

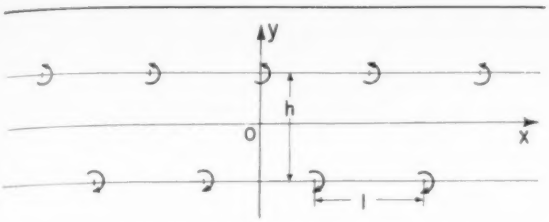

FIG. 1. Vortex centers of the von Kármán vortex street.

Let the perturbation of the vortices of the upper row be (x_m, y_m), those of the lower (x_n', y_n'); then there follows for the radius vector of the nth and nth vortex, relative to the reference vortex $(x_0, (h/2) + y_0)$

$$\gamma_{0m}^2 = (x_0 - ml - x_m)^2 + (y_0 - y_m)^2$$

$$\gamma_{0n}^2 = \{x_0 - [n + (1/2)]l - x_n'\}^2 + (h + y_0 - y_n')^2$$

The equations of motion for the reference vortex are:

$$\left.\begin{aligned}\frac{dx_0}{dt} + u_0 &= -\frac{\Gamma_0}{2\pi}\sum_m{}' \frac{y_0 - y_m}{\gamma_{0m}^2}\\ &\quad (1 - e^{-\gamma_{0m}^2/4\nu t}) + \frac{\Gamma_0}{2\pi}\sum_n \frac{y_0 - y_n' + h}{\gamma_{0n}^2} \times\\ &\quad (1 - e^{-\gamma_{0n}^2/4\nu t})\\ \frac{dy_0}{dt} &= \frac{\Gamma_0}{2\pi}\sum_m{}' \frac{x_0 - x_m - ml}{\gamma_{0m}^2}(1 - e^{-\gamma_{0m}^2/4\nu t}) -\\ &\quad \frac{\Gamma_0}{2\pi}\sum_n \frac{x_0 - x_n' - [n + (1/2)]l}{\gamma_{0n}^2}(1 - e^{-\gamma_{0n}^2/4\nu t})\end{aligned}\right\} \quad (3)$$

In these equations u_0 = common translatory velocity of the system. The index $m = 0$ is not included in the summation; this is indicated by affixing the prime to the summation symbol.

Let the perturbations (x_m, y_m) and (x_n', y_n') be so small in magnitude with respect to the pitch that linearization of the system [Eqs. (3)] is permissible. When introducing the nondimensional time $\tau = (4\nu/l^2)t$ this linearization results in:

$$\left.\begin{aligned}\frac{dx_0}{d\tau} &= -\frac{\Gamma_0}{8\pi\nu}\sum_m{}' \frac{1 - e^{-m^2/\tau}}{m^2}(y_0 - y_m) + \frac{\Gamma_0}{8\pi\nu}\sum_n \left(\frac{[n + (1/2)]^2 - k^2}{\{[n + (1/2)]^2 + k^2\}^2}(1 - e^{-\{[n+(1/2)]^2+k^2\}/\tau}) + \right.\\ &\quad \left.\frac{2k^2}{[n + (1/2)]^2 + k^2}\frac{e^{-\{[n+(1/2)]^2+k^2\}/\tau}}{\tau}\right)(y_0 - y_n') + \frac{\Gamma_0}{8\pi\nu}\sum_n \left(\frac{2[n + (1/2)]k}{\{[n + (1/2)]^2 + k^2\}^2} \times\right.\\ &\quad \left.(1 - e^{-\{[n+(1/2)]^2+k^2\}/\tau}) - \frac{2[n + (1/2)]k}{[n + (1/2)]^2 + k^2}\frac{e^{-\{[n+(1/2)]^2+k^2\}/\tau}}{\tau}\right)(x_0 - x_n')\\ \frac{dy_0}{d\tau} &= -\frac{\Gamma_0}{8\pi\nu}\sum_m{}' \frac{1 - e^{-m^2/\tau} - 2(m^2/\tau)e^{-m^2/\tau}}{m^2}(x_0 - x_m) + \frac{\Gamma_0}{8\pi\nu}\sum_n \left(\frac{[n + (1/2)]^2 - k^2}{\{[n + (1/2)]^2 + k^2\}^2} \times\right.\\ &\quad (1 - e^{-\{[n+(1/2)]^2+k^2\}/\tau}) + \left\{\frac{2k^2}{[n + (1/2)]^2 + k^2 - 2}\right\}\left.\frac{e^{-\{[n+(1/2)]^2+k^2\}/\tau}}{\tau}\right)(x_0 - x_n') - \frac{\Gamma_0}{8\pi\nu}\sum_n \times\\ &\quad \left(\frac{2[n + (1/2)]k}{\{[n + (1/2)]^2 + k^2\}^2}(1 - e^{-\{[n+(1/2)]^2+k^2\}/\tau}) - \frac{2[n + (1/2)]k}{[n + (1/2)]^2 + k^2}\frac{e^{-\{[n+(1/2)]^2+k^2\}/\tau}}{\tau}\right)(y_0 - y_n')\end{aligned}\right\} \quad (4)$$

(4) Stability

Let $\alpha, \beta, \alpha', \beta'$ be functions of the nondimensional time τ. Let the perturbations of the mth vortex of the upper row and of the nth vortex of the lower row be of the form

$$\begin{pmatrix} x_m \\ y_m \end{pmatrix} = \begin{pmatrix} \alpha \\ \beta \end{pmatrix} e^{im\varphi}, \quad \begin{pmatrix} x_n' \\ y_n' \end{pmatrix} = \begin{pmatrix} \alpha' \\ \beta' \end{pmatrix} e^{i[n+(1/2)]\varphi} \quad (5)$$

with $0 < \varphi < 2\pi$. Introducing these formulations into the system [Eqs. (4)] leads to

$$\begin{pmatrix} \dot{\alpha} \\ \dot{\alpha}' \\ \dot{\beta} \\ \dot{\beta}' \end{pmatrix} = -\frac{\Gamma_0}{8\pi\nu}\begin{bmatrix} 0 & B(\tau) & A(\tau) & C(\tau) \\ B(\tau) & 0 & -C(\tau) & -A(\tau) \\ \bar{A}(\tau) & \bar{C}(\tau) & 0 & -\bar{B}(\tau) \\ -\bar{C}(\tau) & -\bar{A}(\tau) & -\bar{B}(\tau) & 0 \end{bmatrix}\begin{pmatrix} \alpha \\ \alpha' \\ \beta \\ \beta' \end{pmatrix} \quad (6)$$

with the initial condition

$$\begin{bmatrix} \alpha(0) \\ \alpha'(0) \\ \beta(0) \\ \beta'(0) \end{bmatrix} = \begin{pmatrix} \alpha_0 \\ \alpha_0' \\ \beta_0 \\ \beta_0' \end{pmatrix} \quad (6a)$$

The equations for α' and β' are obtained by selecting the vortex $n = 0$ as reference vortex. The functions $A(\tau)$, $B(\tau)$, $C(\tau)$; $\bar{A}(\tau)$, $\bar{B}(\tau)$, $\bar{C}(\tau)$ according to Eqs. (4) are defined as follows:

$$A(\tau) = \sum_m{}' \frac{1 - e^{im\varphi}}{m^2}(1 - e^{-m^2/\tau}) - \sum_n \frac{[n + (1/2)]^2 - k^2}{\{[n + (1/2)]^2 + k^2\}^2}(1 - e^{-\{[n+(1/2)]^2+k^2\}/\tau} -$$
$$\sum_n \frac{2k^2}{[n + (1/2)]^2 + k^2} \frac{e^{-\{[n+(1/2)]^2+k^2\}/\tau}}{\tau}$$

$$B(\tau) = \sum_n \left(\frac{2[n + (1/2)]k}{\{[n + (1/2)]^2 + k^2\}^2}(1 - e^{-\{[n+(1/2)]^2+k^2\}/\tau}) - \right.$$
$$\left. \frac{2[n + (1/2)]k}{[n + (1/2)]^2 + k^2} \frac{e^{-\{[n+(1/2)]^2+k^2\}/\tau}}{\tau} \right) e^{i[n+(1/2)]\varphi}$$

$$C(\tau) = \sum_n \left(\frac{[n + (1/2)]^2 - k^2}{\{[n + (1/2)]^2 + k^2\}^2}(1 - e^{-\{[n+(1/2)]^2+k^2\}/\tau}) + \right.$$
$$\left. \frac{2k^2}{[n + (1/2)]^2 + k^2} \frac{e^{-\{[n+(1/2)]^2+k^2\}/\tau}}{\tau} \right) e^{i[n+(1/2)]\varphi} \tag{6b}$$

$$\bar{A}(\tau) = A(\tau) + 2\left[\sum_n \frac{e^{-\{[n+(1/2)]^2+k^2\}/\tau}}{\tau} - \sum_m{}' \frac{e^{-m^2/\tau}}{\tau}(1 - e^{im\varphi}) \right]$$

$$\bar{B}(\tau) = B(\tau) = 2i \sum_{n=0}^{\infty} \left(\frac{2[n + (1/2)]k}{\{[n + (1/2)]^2 + k^2\}^2}(1 - e^{-\{[n+(1/2)]^2+k^2\}/\tau}) - \right.$$
$$\left. \frac{2[n + (1/2)]k}{[n + (1/2)]^2 + k^2} \frac{e^{-\{[n+(1/2)]^2+k^2\}/\tau}}{\tau} \right) \sin\left(n + \frac{1}{2}\right)\varphi$$

$$\bar{C}(\tau) = C(\tau) - 2\sum_n \frac{e^{-\{[n+(1/2)]^2+k^2\}/\tau}}{\tau} e^{i[n+(1/2)]\varphi}$$

The mathematical problem is as follows: Find a system of solutions $(\alpha, \beta, \alpha', \beta')$ of Eqs. (6) and (6a), for which $(|\alpha|, |\beta|, |\alpha'|, |\beta'|)$ remain prescribably small as τ increases steadily. This must apply to all φ for $0 < \varphi < 2\pi$. To solve, first apply the transformation

$$\begin{pmatrix} p_1 \\ q_1 \\ p_2 \\ q_2 \end{pmatrix} = \begin{pmatrix} 1 & 1 & 0 & 0 \\ 1 & -1 & 0 & 0 \\ 0 & 0 & 1 & -1 \\ 0 & 0 & 1 & 1 \end{pmatrix} \begin{pmatrix} \alpha \\ \alpha' \\ \beta \\ \beta' \end{pmatrix} \tag{7}$$

to the system of differential equations (6), thereby transmuting these to the form

$$\begin{pmatrix} \dot{p}_1 \\ \dot{q}_1 \\ \dot{p}_2 \\ \dot{q}_2 \end{pmatrix} = -\frac{\Gamma_0}{8\pi\nu} \begin{pmatrix} B(\tau) & 0 & [A(\tau) - C(\tau)] & 0 \\ 0 & -B(\tau) & 0 & [A(\tau) + C(\tau)] \\ [\bar{A}(\tau) + \bar{C}(\tau)] & 0 & B(\tau) & 0 \\ 0 & [\bar{A}(\tau) - \bar{C}(\tau)] & 0 & -B(\tau) \end{pmatrix} \begin{pmatrix} p_1 \\ q_1 \\ p_2 \\ q_2 \end{pmatrix} \tag{8}$$

It may readily be seen from Eq. (8) that this system can be divided into two mutually independent simpler systems—namely,

$$\begin{pmatrix} \dot{p}_1 \\ \dot{p}_2 \end{pmatrix} = -\frac{\Gamma_0}{8\pi\nu} \begin{pmatrix} B(\tau) & [A(\tau) - C(\tau)] \\ [\bar{A}(\tau) + \bar{C}(\tau)] & B(\tau) \end{pmatrix} \begin{pmatrix} p_1 \\ p_2 \end{pmatrix} \tag{9}$$

$$\begin{pmatrix} \dot{q}_1 \\ \dot{q}_2 \end{pmatrix} = -\frac{\Gamma_0}{8\pi\nu} \begin{pmatrix} -B(\tau) & [A(\tau) + C(\tau)] \\ [\bar{A}(\tau) - \bar{C}(\tau)] & -B(\tau) \end{pmatrix} \begin{pmatrix} q_1 \\ q_2 \end{pmatrix} \tag{10}$$

with the initial conditions

$$\begin{bmatrix} p_1(0) \\ p_2(0) \end{bmatrix} = \begin{pmatrix} \alpha_0 + \alpha_0' \\ \beta_0 - \alpha_0' \end{pmatrix}$$
$$\begin{bmatrix} q_1(0) \\ q_2(0) \end{bmatrix} = \begin{pmatrix} \alpha_0 - \alpha_0' \\ \beta_0 + \beta_0' \end{pmatrix}$$

Since the function $B(\tau)$ is purely imaginary, Eqs. (9) and (10) may be simplified further by substituting

$$\begin{pmatrix} p_1 \\ p_2 \end{pmatrix} = \begin{pmatrix} \tilde{p}_1 \\ \tilde{p}_2 \end{pmatrix} e^{-\frac{\Gamma_0}{8\pi\nu}\int_0^\tau B(\tau_1)d\tau_1} \tag{11a}$$

$$\begin{pmatrix} q_1 \\ q_2 \end{pmatrix} = \begin{pmatrix} \tilde{q}_1 \\ \tilde{q}_2 \end{pmatrix} e^{+\frac{\Gamma_0}{8\pi\nu}\int_0^\tau B(\tau_1)d\tau_1} \tag{11b}$$

This calculation yields

$$\begin{pmatrix} \dot{\tilde{p}}_1 \\ \dot{\tilde{p}}_2 \end{pmatrix} = -\frac{\Gamma_0}{8\pi\nu} \begin{bmatrix} 0 & A(\tau) - C(\tau) \\ \bar{A}(\tau) + \bar{C}(\tau) & 0 \end{bmatrix} \begin{pmatrix} \tilde{p}_1 \\ \tilde{p}_2 \end{pmatrix} \tag{12}$$

$$\begin{pmatrix} \dot{\tilde{q}}_1 \\ \dot{\tilde{q}}_2 \end{pmatrix} = -\frac{\Gamma_0}{8\pi\nu} \begin{bmatrix} 0 & A(\tau) + C(\tau) \\ \bar{A}(\tau) - \bar{C}(\tau) & 0 \end{bmatrix} \begin{pmatrix} \tilde{q}_1 \\ \tilde{q}_2 \end{pmatrix} \tag{13}$$

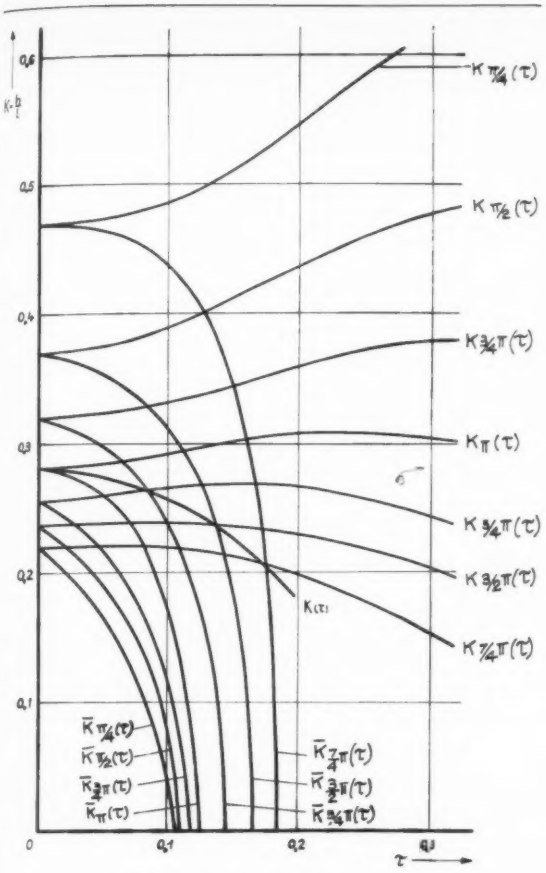

FIG. 2. Condition of stability.

The initial conditions remain invariant when subjected to the transformation (11a), (11b). By undoing the process of transformation just performed, it is possible to trace the path of the individual vortices—namely, for a vortex of the upper row of the street—

$$\begin{pmatrix} x_m \\ y_m \end{pmatrix} = \frac{1}{2}\begin{pmatrix} \tilde{p}_1 \\ \tilde{p}_2 \end{pmatrix} e^{-\left[\frac{\Gamma_0}{8\pi\nu}\int_0^\tau B(\tau_1)d\tau_1 - im\varphi\right]} + \frac{1}{2}\begin{pmatrix} \tilde{q}_1 \\ \tilde{q}_2 \end{pmatrix} e^{+\left[\frac{\Gamma_0}{8\pi\nu}\int_0^\tau B(\tau_1)d\tau_1 + im\varphi\right]} \quad (14)$$

and for a vortex of the lower row

$$\begin{pmatrix} x_n' \\ y_n' \end{pmatrix} = \frac{1}{2}\begin{pmatrix} 1 & 0 \\ 0 & -1 \end{pmatrix}\begin{pmatrix} \tilde{p}_1 \\ \tilde{p}_2 \end{pmatrix} e^{-\left[\frac{\Gamma_0}{8\pi\nu}\int_0^\tau B(\tau_1)d\tau_1 - i\left(n+\frac{1}{2}\right)\varphi\right]} + \frac{1}{2}\begin{pmatrix} 1 & 0 \\ 0 & 1 \end{pmatrix}\begin{pmatrix} \tilde{q}_1 \\ \tilde{q}_2 \end{pmatrix} e^{+\left[\frac{\Gamma_0}{8\pi\nu}\int_0^\tau B(\tau_1)d\tau_1 + i\left(n+\frac{1}{2}\right)\varphi\right]} \quad (15)$$

Since $B(\tau)$ is purely imaginary, the exponential functions occurring in Eqs. (14) and (15) cannot exceed the value unity. The requirement previously established for the system of solutions (α, α', β, β')—namely, that its value remain prescribably small—may now be applied to the system of solutions ($\tilde{p}_1$, $\tilde{p}_2$, $\tilde{q}_1$, $\tilde{q}_2$).

In his previous paper[3] the author has investigated the stability of the solution of a system of differential equations of the type of systems (12) and (13). The result of this investigation will be explained for the example of Eqs. (12) and (13). The elements of the matrices of Eqs. (12) and (13) are functions of τ, of the quotient $k = h/l$, and of the phase parameter φ. If the matrix elements, say, of the system (12), for a fixed value of φ are equated to zero, one arrives at certain functions $k_\varphi = k_\varphi(\tau)$ and $\bar{k}_\varphi = \bar{k}_\varphi(\tau)$ which derive their definition from this process. In the (k, τ)-plane both curves, provided they exist, circumscribe a region in which the two elements, for any set of (k, τ) values from this region, are of different sign. In this region enclosed by the curves, the solution of the system, in the sense discussed above, is stable. The border of this region does not belong to the stable region, except at the points that pertain to $k_\varphi = k_\varphi(\tau)$ and $\bar{k}_\varphi = \bar{k}_\varphi(\tau)$ at the same time.

In order to compute the stability range for given phase parameters, it is necessary to solve the following equations.

$$\left.\begin{aligned} A(\tau, k, \varphi) - C(\tau, k, \varphi) &= 0 \\ \bar{A}(\tau, k, \varphi) + \bar{C}(\tau, k, \varphi) &= 0 \\ A(\tau, k, \varphi) + C(\tau, k, \varphi) &= 0 \\ \bar{A}(\tau, k, \varphi) - \bar{C}(\tau, k, \varphi) &= 0 \end{aligned}\right\} \quad (16)$$

The solution was carried through by numerical and graphical methods for the phase parameters φ: $\pi/4$, $\pi/2, 3\pi/4, \pi, 5\pi/4, 3\pi/2, 7\pi/4$.

It is only necessary to solve the first two equations since the functions $A(\tau, k, \varphi)$, $\bar{A}(\tau, k, \varphi)$; $C(\tau, k, \varphi)$, $\bar{C}(\tau, k, \varphi)$, by virtue of their definition [Eqs. (6b)], satisfy the relations

$$\left.\begin{aligned} A(\tau, k, \varphi) &= A(\tau, k, 2\pi - \varphi) \\ \bar{A}(\tau, k, \varphi) &= \bar{A}(\tau, k, 2\pi - \varphi) \\ C(\tau, k, \varphi) &= -C(\tau, k, 2\pi - \varphi) \\ \bar{C}(\tau, k, \varphi) &= -\bar{C}(\tau, k, 2\pi - \varphi) \end{aligned}\right\} \quad (17)$$

In Fig. 2 the ratio k has been plotted along the ordinate and the nondimensional time τ has been plotted along the abscissa. Each of the curves of the family of curves plotted has been marked by its phase-parameter. First let us consider the stability regions themselves of the system (12). For the phase parameter $\varphi = \pi/4$, the stability range is bounded by the curves $k_{\pi/4}(\tau)$ and $\bar{k}_{\pi/4}(\tau)$. For $\tau = 0$ infinitely many solutions are possible. If perturbations with phase parameters $\varphi \to \pi$ are considered, the possible stability range is narrowed steadily. For $\pi = \varphi$ at $\tau = 0$, only $k = h/l = 0.281$ is feasible; at $\tau > 0$, however, there exists a stability range similar to the range that results from perturbation of a single vortex. If the phase parameter is increased above $\varphi = \pi$, it is found that there exist regions of peculiar form, each defined by a characteristic point for a certain $\tau > 0$ which must be common to all stable solutions for that particular phase parameter. If a general perturbation is considered, composed of perturbations of all per-

missible phase parameters, then evidently there remains only the linear multiplicity of the characteristic points as the only possible stable solution. This condition has been plotted in Fig. 2 and labeled $k = k(\tau)$. The stable vortex street, in agreement with von Kármán, for vanishing τ—i.e., vanishing viscosity or vanishing time—exists at the value $k = 0.281$.

The family of curves, Fig. 2, may also be regarded as a master diagram of the stability ranges of the system (13), as may be seen from Eqs. (17). It is only necessary to replace any given index φ by $2\pi - \varphi$. From this it follows in particular that the established stability condition satisfies Eqs. (12) and (13) at the same time, as required.

(5) Comments

The significance of the nondimensional time τ may be understood readily when regarding it as the square of the ratio of two lengths. Aside from a constant factor, $(4\nu t)^{1/2}$ is equal to the core radius of the real vortex, Eq. (1). Although some authors have hinted at the significance of the core radius for the stability problem, there exist, outside of Hooker's results, no experimental data. In view of this situation there is need for investigations that should furnish information whether the kinematic viscosity is adequate for the computation of the core radius or else, as may be suspected from experimental investigations,[6] whether turbulent momentum transport must also be taken into account.

(6) References

[1] von Kármán, Th., Göttinger Nachr., pp. 509–517, 1911; pp. 547–556, 1912.

[2] Hooker, S. G., Proc. Roy. Soc. (London), Vol. A154, pp. 67–89, 1936.

[3] Domm, U., Diss. Technische Universität Berlin-Charlottenburg, 1953. Extract to appear in Ing. Archiv (in print).

[4] Rosenhead, L., Advances in Applied Mechanics III, p. 185, 1953.

[5] Hamel, G., Jahresbericht der deutschen Mathm. Vereinigung, Vol. 25, p. 50, 1917.

[6] Wille, R., Jahrbuch der Schiffbautechnischen Gesellschaft, p. 176, 1952.

An Authorized Binding for
Journal of the Aeronautical Sciences

Arrangements have been made by the Institute of the Aeronautical Sciences for members and subscribers to have their Journals bound into distinctively designed books.

Twelve issues, January through December, bound in best grade blue washable buckram, imprinted with your name on cover, cost but $3.45 per volume.

Ship Journals parcel post insured. Within 30 days after receipt, bound volumes will be shipped prepaid in the U.S.A. Full remittance must accompany order.

Publishers' Authorized Bindery Service
(*Binders of all Journals*)

308 West Randolph St. Chicago 6, Ill.

Design Charts for Transient Temperature Distribution Resulting from Aerodynamic Heating at Supersonic Speeds*

JOSEPH KAYE† AND VICTOR C. M. YEH‡
Massachusetts Institute of Technology

SUMMARY

The transient temperature distribution in a vehicle resulting from aerodynamic heating at high supersonic speeds may be rapidly estimated by means of a set of design charts presented herein. These design charts are based on the analytical solution to the one-dimensional heat flow in a solid body of constant material properties when the boundary conditions are strongly dependent on time. The surface coefficient of heat transfer is taken to be a linear function of time of flight, and the temperature potential is also taken to be a linear function of time of flight. The design charts are presented in such a form that they may be used for cases where the surface coefficient of heat transfer and the temperature potential are much more complicated functions of time of flight than used here. The method of use of these design charts is illustrated with two examples based on a previous study of the transient temperature distribution in a wedge-shaped wing flying at supersonic speeds.

SYMBOLS

C = conductance ratio = hl/k
c_p = specific heat at constant pressure
h = surface coefficient of heat transfer
k = thermal conductivity
l = half-thickness of wing
M = Mach Number
N = position ratio = x/l
p = complex variable in definition of Laplace transform
q = rate of heat transfer
r = integers, 0, 1, 2, . . .
t = temperature
X = relative time, $\alpha\vartheta/l^2$
x = distance normal to chord of wing
Y = temperature-rise ratio = $\tau/\tau_p = (t - t_b)/(t_{aw} - t_w)$
z = defined by Eqs. (36) and (37)
Z = defined by Eq. (39)
α = thermal diffusivity = $k/\rho c_p$
ρ = density
τ = temperature difference
$\bar{\tau}$ = defined by Eq. (21)
ϑ = time
a,b,B,C_0, C_1,D_1,D_2 = constants

Subscripts

aw = adiabatic wall condition
b = initial condition
p = temperature potential
N = position
w = wall position

Received September 13, 1954.
* The authors are grateful to John Stekly for his assistance in the preparation of this paper.
† Professor of Mechanical Engineering.
‡ Formerly, Lecturer, Mechanical Engineering Department, College of the City of New York. Now, Assistant Professor, Department of Engineering Mechanics, New York University.

INTRODUCTION

THE DESIGNER OF AIRCRAFT, missiles, and other devices that move at high supersonic speeds must be able to obtain reasonable engineering solutions in a reasonable time to the difficult thermal problems that arise in such devices. The thermal problems resulting from aerodynamic heating are well known. For example, a simple calculation shows that for steady flight at a speed of 5,500 m.p.h. (or at a Mach Number of 8) at an altitude of 50,000 ft. the surface temperature of the vehicle will be of the order of 4,000°F. But the designer needs to determine rapidly the transient nonuniform temperature distribution from the start of the flight to the steady flight condition or for any specified flight program.

The general problem of calculation of the transient temperature distribution in three dimensions in a device moving at supersonic speeds is greatly complicated by many factors, such as the geometry, the variation of material properties with temperature, the time-dependent boundary conditions, and the state of the art in fluid mechanics and heat transfer at high speeds. If the problem is restricted to two-dimensional heat flow in a solid of simple geometry and with constant material properties, numerical methods of integration can be employed as in reference 1. If the problem is restricted further to one-dimensional heat flow in a solid of simple geometry and with constant material properties, then this problem with time-dependent boundary conditions can be solved by analytical means; such a solution is presented here and then is reduced to the form of useful design charts to permit rapid and reasonable estimates of the transient temperature distribution for many practical cases of aerodynamic heating.

In order to demonstrate the utility of these design charts, the present discussion will use the results obtained previously for a wedge-shaped wing flying at supersonic speeds. These results were obtained by numerical integration of the two-dimensional heat flow and also of the simpler one-dimensional heat flow in a solid body with constant material properties.

STATEMENT OF PROBLEM

Consider a device moving at variable supersonic speeds and assume the local portion under consideration is fairly thin, so that one-dimensional heat flow obtains. As the device moves through the atmosphere it

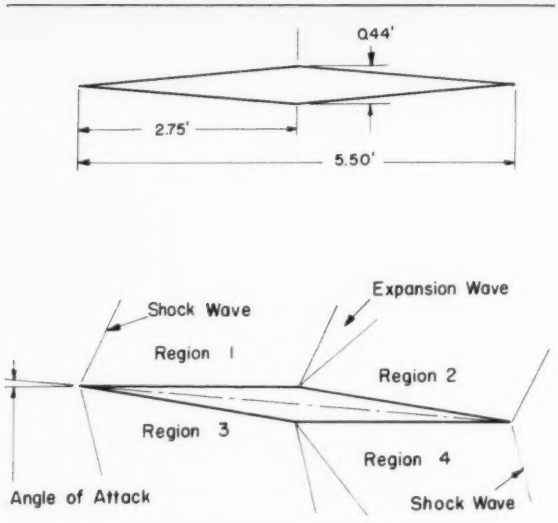

FIG. 1. Dimensions and airflow pattern of a wedge-shaped wing.

will rise in temperature, due to aerodynamic heating, and heat will be transferred into the device by conduction and away from the surface by radiation. Radiation is neglected here for the purpose of comparison with the results of reference 1. The problem is to determine or estimate rapidly the transient temperature distribution in the thin portion of the device for the case where the heat-transfer coefficient at a given location varies with time and the adiabatic wall temperature varies with time.

The problem can be illustrated by the wedge-shaped wing, shown in Fig. 1, used in reference 1. The problem is to determine the transient temperature distribution at point e along a line normal to the chord of the wing. Fig. 2 shows an enlargement of the wing at point e as well as the symbols used. As point e is moved to other positions along the wing, a succession of temperature distributions normal to the chord is obtained, and hence an approximate two-dimensional transient temperature distribution is produced.

ANALYSIS

Consider the general case of transient one-dimensional heat flow in a material of constant properties with the boundary conditions and the temperature potential dependent on time for the simple geometry shown in Fig. 2.

The differential equation is given by

$$[\partial^2 t(x, \vartheta)/\partial x^2] - (1/\alpha)[\partial t(x, \vartheta)/\partial \vartheta] = 0 \quad (1)$$

The three boundary conditions are as follows: At $\vartheta = 0$,

$$t = t_b \quad (2)$$

At $x = 0$,

$$\partial t/\partial x = 0 \quad (3)$$

At $x = 1$,

$$k(\partial t/\partial x) = h(t_{aw} - t_w) \quad (4)$$

The surface coefficient of heat transfer and the adiabatic wall temperature are time-dependent quantities, given by

$$h = f_1(\vartheta) \quad (5)$$

$$t_{aw} = f_2(\vartheta) \quad (6)$$

For convenience of solution and to save space, dimensionless groups and transformations are used. The resulting equations and boundary conditions are then solved by means of the Laplace transformation and auxiliary methods.

The following definitions and transformations are used:

Temperature rise

$$\tau \equiv t - t_b = \tau(x, \vartheta) \quad (7)$$

Temperature potential

$$\tau_p \equiv t_{aw} - t_w \quad (8a)$$

$$= \tau_{aw} - \tau_w = \tau(\vartheta) \quad (8b)$$

Temperature-rise ratio

$$Y \equiv \tau/\tau_p \quad (9a)$$

$$= (t - t_b)/(t_{aw} - t_w) \quad (9b)$$

Relative time

$$X \equiv \alpha\vartheta/l^2 \quad (10)$$

Position ratio

$$N \equiv x/l \quad (11)$$

Conductance ratio

$$C \equiv hl/k \quad (12)$$

Introducing these definitions, Eqs. (1) to (4) become

$$[\partial^2\tau(N,X)/\partial N^2] - [\partial\tau(N,X)/\partial X] = 0 \quad (13)$$

$$\tau(N,0) = 0 \quad (14)$$

$$\partial\tau(0,X)/\partial N = 0 \quad (15)$$

$$\partial\tau(1,X)/\partial N = C(X)\tau_p(X) \quad (16)$$

Previous work on the wedge-shaped wing[1] has shown that to a good approximation the variation of surface

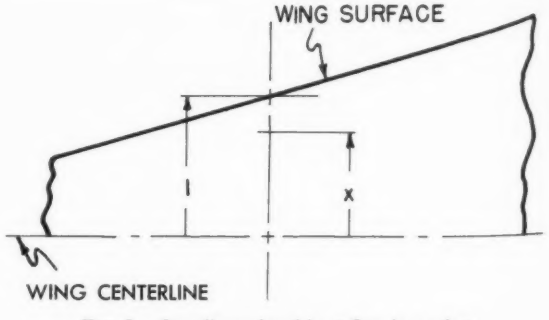

FIG. 2. One-dimensional heat flow in a wing.

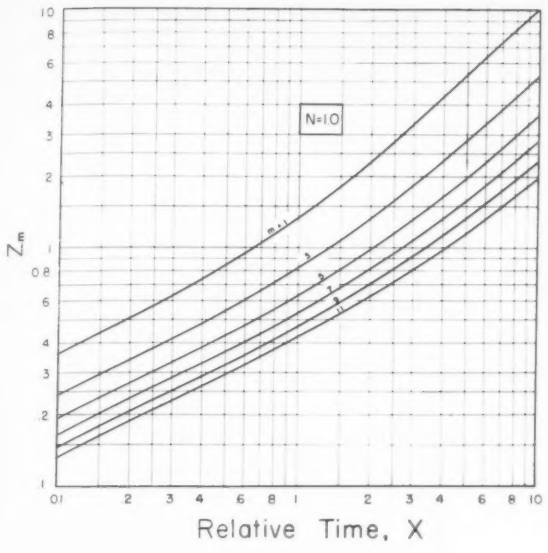

FIG. 3.

coefficient with time may be assumed to be linear and that the variation of temperature potential with time may also be assumed to be linear. These relations will be used merely as first approximations for the general one-dimensional heat flow problem. Then

$$h = a + b\vartheta \tag{17}$$

or $$C = al/k + (bl^3/k\alpha)(\alpha\vartheta/l^2) = C_0 + C_1X \tag{18}$$

and $$\tau_p = BX \tag{19}$$

where a, b, C_0, C_1, and B are constants.

Hence the boundary conditions given by Eq. (16) can be rewritten as

$$\partial\tau(1,X)/\partial N = (C_0 + C_1X)BX \tag{20}$$

The general problem of one-dimensional heat flow, defined by Eqs. (1) to (4) with the conditions of time-dependence of h and t_{aw} given by Eqs. (5) and (6), has been thus reduced to a relatively simple set of equations by use of a linear variation of h and τ_p with time, given by Eqs. (17) and (19). However, it is not necessary that h and τ_p vary linearly with time, since one can employ general variations in the form of general polynomials for the time dependence of h and of τ_p. The resulting general solution, to be published at a later date, then uses a double summation for the boundary conditions expressed in this analysis by the simple quadratic relation of Eq. (20). This general solution has also greater applicability than the present analysis limited to aerodynamic heating.

Defining the Laplace transform by

$$\bar{\tau}(p,N) \equiv \int_0^\infty e^{-pX}\tau(N,X)\,dX \tag{21}$$

and operating on Eq. (13) by this transform, we get the following subsidiary equation

$$[\partial^2\bar{\tau}(p,N)/\partial N^2] - p\bar{\tau}(p,N) + \tau(N,0) = 0 \tag{22}$$

But the initial condition in Eq. (14) permits the dropping of the last term in Eq. (22), so that it becomes

$$[\partial^2\bar{\tau}(p,N)/\partial N^2] - p\bar{\tau}(p,N) = 0 \tag{23}$$

The two boundary conditions, given by Eqs. (20) and (13) become

$$\vartheta\bar{\tau}(p,1)/\partial N = B[(C_0/p^2) + (2C_1/p^3)] \tag{24}$$

$$\partial\bar{\tau}(p,0)/\partial N = 0 \tag{25}$$

Hence the original partial differential equation, the initial condition, and the boundary conditions have been transformed to a set of three total differential equations that can be solved by usual methods.

The solution to the subsidiary equation, Eq. (23), is given by

$$\bar{\tau}(p,N) = D_1 \cosh N\sqrt{p} + D_2 \sinh N\sqrt{p} \tag{26}$$

Hence $$\partial\bar{\tau}(p,N)/\partial N = D_1\sqrt{p}\sinh N\sqrt{p} + D_2\sqrt{p}\cosh N\sqrt{p} \tag{27}$$

But from Eq. (25),

$$\partial\bar{\tau}(p,0)/\partial N = 0$$

and we get $D_2 = 0$,

$$\frac{\partial\bar{\tau}(p,N)}{\partial N} = D_1\sqrt{p}\sinh N\sqrt{p} \tag{28}$$

From Eqs. (24) and (28) we get

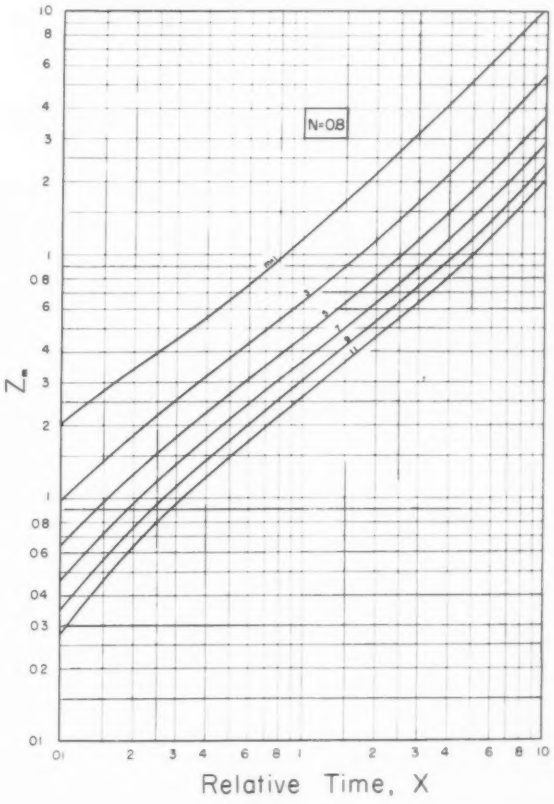

FIG. 4.

$$D_1 = [B/(\sqrt{p}\sinh\sqrt{p})]\,[(C_0/p^2) + (2C_1/p^3)] \quad (29)$$

Hence $$\bar{\tau}(p,N) = (B\cosh N\sqrt{p})/(\sinh\sqrt{p}) \times [(Co/p^{5/2}) + (2C_1/p^{7/2})] \quad (30)$$

In order to transform Eq. (30) back to the N-X plane, it was found necessary to change the hyperbolic functions in Eq. (30) by the binominal expansion into an infinite series as follows:

$$\left.\begin{aligned}\cosh N\sqrt{p}/\sinh\sqrt{p} &= (e^{N\sqrt{p}} + e^{-N\sqrt{p}}) \div [e^{\sqrt{p}}(1 - e^{-2\sqrt{p}})] \\ &= \sum_{r=0}^{\infty} [e^{-\sqrt{p}\,(2r+1-N)} + e^{-\sqrt{p}\,(2r+1+N)}]\end{aligned}\right\} \quad (31)$$

The desired inverse Laplace transform given on page 380 of *Conduction of Heat in Solids* by Carslaw and Jaeger is now written in terms of p, X, and the parameter x, as follows:

$$\mathfrak{L}^{-1}\left\{\frac{e^{-\sqrt{p}\,x}}{p^{1+n/2}}\right\} = (4X)^{n/2}\, i^n \operatorname{erfc}\left\{\frac{x}{2\sqrt{X}}\right\} \quad (32)$$

For the rth term of the infinite series which is formed by combining Eq. (31), with the first term in the first set of parenthesis in Eq. (30), we get

$$\mathfrak{L}^{-1}\left\{BC_0\left[\frac{e^{-\sqrt{p}\,(2r+1-N)}}{p^{1+3/2}} + \frac{e^{-\sqrt{p}\,(2r+1+N)}}{p^{1+3/2}}\right]\right\} = BC_0\left\{(4X)^{3/2}\left[i^3\operatorname{erfc}\frac{(2r+1-N)}{2\sqrt{X}} + i^3\operatorname{erfc}\frac{(2r+1+N)}{2\sqrt{X}}\right]\right\} \quad (33)$$

For the rth term of the infinite series which is formed by combining Eq. (31) with the second term in the first set of parenthesis in Eq. (30), we get

$$\mathfrak{L}^{-1}\left\{2BC_1\left[\frac{e^{-\sqrt{p}\,(2r+1-N)}}{p^{1+5/2}} + \frac{e^{-\sqrt{p}\,(2r+1+N)}}{p^{1+5/2}}\right]\right\} = 2BC_1\left\{(4X)^{5/2}\left[i^5\operatorname{erfc}\frac{(2r+1-N)}{2\sqrt{X}} + i^5\operatorname{erfc}\frac{(2r+1+N)}{2\sqrt{X}}\right]\right\} \quad (34)$$

The complete solution, transformed to the N-X plane, is given by the following infinite series:

$$\tau(N,X) = B\sum_{r=0}^{\infty}[C_0(4X)^{3/2}(i^3\operatorname{erfc} z + i^3\operatorname{erfc} z') + 2C_1(4X)^{5/2}(i^5\operatorname{erfc} z + i^5\operatorname{erfc} z')] \quad (35)$$

where $$z \equiv (2r + 1 - N)/2\sqrt{X} \quad (36)$$

$$z' \equiv (2r + 1 + N)/2\sqrt{X} \quad (37)$$

The analytical solution represented by Eq. (35) can be verified by showing that it satisfies simultaneously the original differential Eq. (13) and the three boundary conditions [Eqs. (14), (15), and (16)]. The solution can also be used to obtain the spatial and time temperature gradients; these will not be given here but in a later publication discussing the generalized solution for any variation of boundary conditions with time.

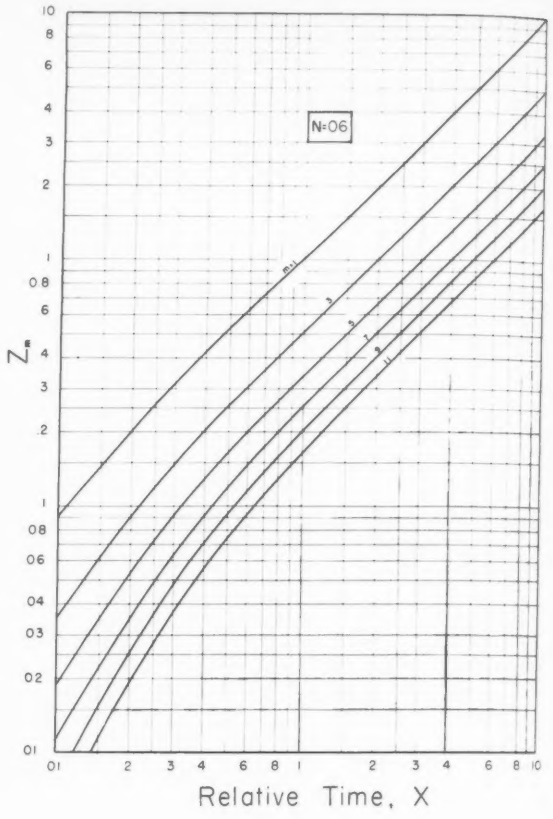

FIG. 5.

The complete solution given by Eq. (35) can be placed in a more useful form by eliminating the constant B of Eq. (19) since it is not zero and introducing the temperature-rise ratio of Eq. (9), as follows:

$$Y = (t - t_0)/(t_{aw} - t_w) = C_0 2^3\sqrt{X}\sum_{r=0}^{\infty}(i^3\operatorname{erfc} z + i^3\operatorname{erfc} z') + 2(2)^5 C_1 X^{3/2}\sum_{r=0}^{\infty}(i^5\operatorname{erfc} z + i^5\operatorname{erfc} z') \quad (38)$$

Let us next define, for brevity, a function Z_m, which includes the infinite sum of the repeated integrals of the error functions given in Eq. (38),

$$Z_m \equiv 2^m\left(\frac{m-1}{2}\right)!\,\sqrt{X}\sum_{r=0}^{\infty}(i^m\operatorname{erfc} z + i^m\operatorname{erfc} z') \quad (39)$$

where m is an integer indicating the order of the repeated integral of the error function.

The final result for the temperature distribution can be written as

$$Y = C_0 Z_3 + C_1 X Z_5 \quad (40)$$

where the constants C_0 and C_1 are defined in Eq. (18).

The transient temperature distribution, given by Eq. (40), can be computed in a straightforward way if the various Z_m functions are computed and arranged

in chart form. The next section describes these functions and illustrates their use for problems of aerodynamic heating.

Design Charts for Transient Temperature Distribution with Time-Dependent Boundary Conditions

The major objective of this paper is to present a set of useful design charts to permit the designer to predict the transient temperature distribution for one-dimensional heat flow in a thin body moving at supersonic speeds under conditions of aerodynamic heating. These design charts are based on the analytical solution given by Eq. (40), where the temperature-rise ratio, Y, is a function of the relative time, X, the position ratio, N, and certain arbitrary constants, dependent on the flight conditions. Since Z_m is a function only of relative time, X, and position ratio, N, it is simple to construct charts, each for a different value of N showing many values of Z for a large range of values of X. Such charts have different coordinates than those used in the well known Gurney-Lurie charts and the Hottel charts, constructed for the special case of boundary conditions that are independent of time.

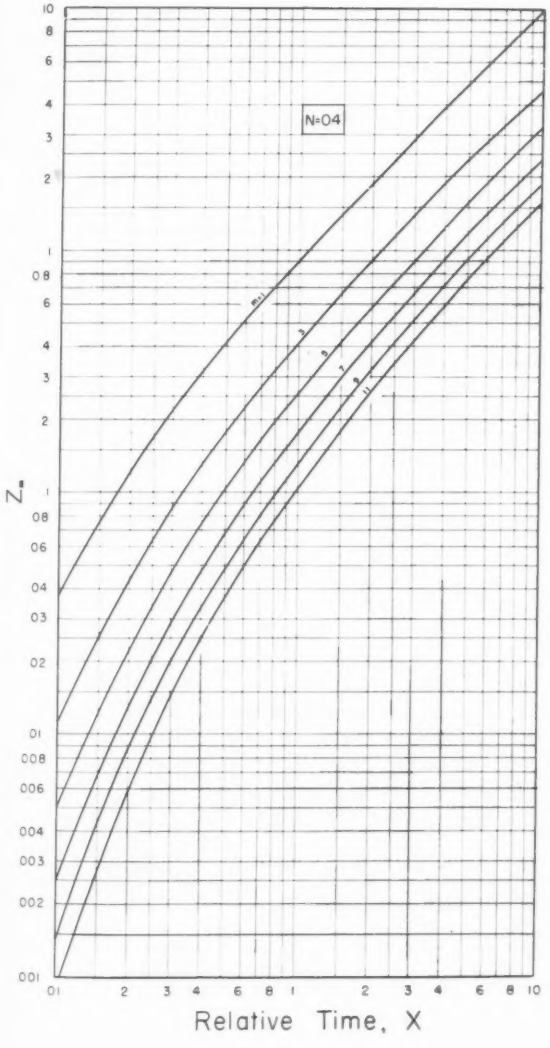

Fig. 6.

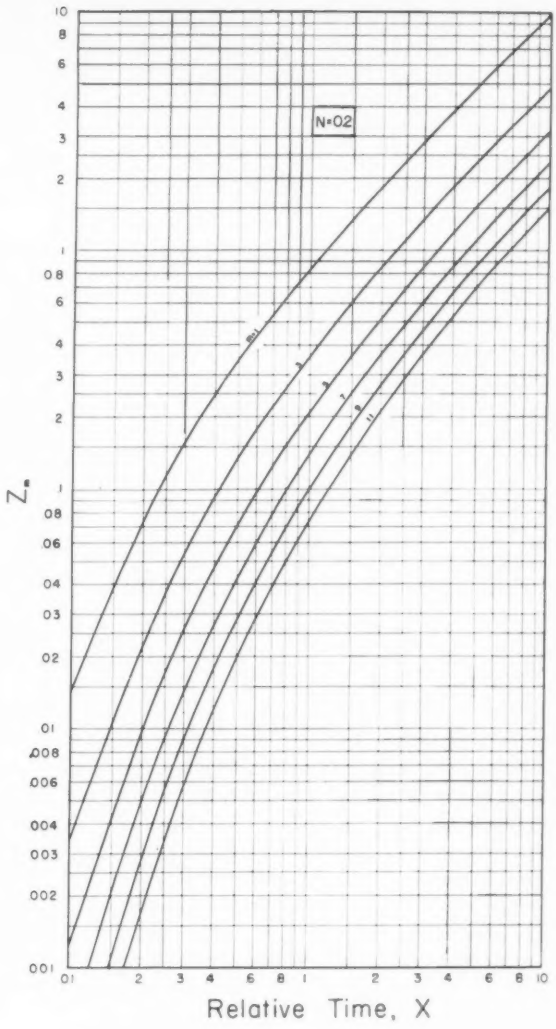

Fig. 7.

Six design charts have been constructed for values of the position ratio, N, equal to 1, 0.8, 0.6, 0.4, 0.2, and 0, shown in Figs. 3, 4, 5, 6, 7, and 8, respectively. Each of these six design charts contains the Z_m functions, Z_1, Z_3, Z_5, Z_7, Z_9, and Z_{11}, so that the charts may be used to solve problems that are more general than those considered in this paper. Various attempts were made to reduce the several lines for different values of Z_m to a common line, but in all cases tried a considerable loss in accuracy was introduced. The charts were computed with the aid of a recent tabulation of repeated integrals of the error function.[2]

The six design charts are presented in log-log form for several reasons. First the state of the art of heat-transfer coefficients for supersonic flow does not permit selection of this important parameter with an accuracy

of better than 20 per cent. Second, the properties of the material are assumed to be independent of temperature, but actually this factor introduces additional error at the higher temperatures. Third, the heat flow is not truly one-dimensional in a real case. Hence, it was decided to select scales for Y and X on these charts which would permit engineering estimates of fair accuracy.

Methods of Use of Design Charts

The design charts are used most easily by evaluating first the surface temperature of the device at the desired instant of time and then the internal temperatures by the following scheme.

At the surface, $N = 1$, and so

$$Y_1 \equiv \tau_1/\tau_p \equiv \tau_1/(\tau_{aw} - \tau_1) \tag{41}$$

If Eq. (41) is solved for τ_1, we get

$$\tau_1 = \tau_{aw} Y_1/(1 + Y_1) \tag{42}$$

For any internal position ratio, N, we have

$$Y_N \equiv \tau_N/\tau_p \equiv \tau_N/(\tau_{aw} - \tau_1) \tag{43}$$

Considering Eqs. (42) and (43), we get

$$\tau_N = \tau_{aw} Y_N/(1 + Y_1) \tag{44}$$

From the conditions of the types of problems considered here, X is computed first, the six charts entered at this value of X to produce the values of the desired functions of Z_m. Then the value of Y_1, at the surface, is computed from the final solution given by Eq. (40), or by variations of this solution. The surface temperature rise is computed from Eq. (42), once the adiabatic temperature rise, τ_{aw}, has been found from the conditions of the problem. The individual values of Y_n are then computed from the known values of Z_m for each value of the position ratio, N. Finally, Eq. (44) is used to compute the temperature rise τ_N at each value of N. Knowing the initial temperature, t_b, the actual temperature distribution is then found.

The method of using the design charts is illustrated by two detailed numerical examples. In order to save space these examples are selected from the previous study[1] for the transient temperature distribution in a wedge-shaped wing flying at supersonic speeds. In this study a wedge-shaped steel wing, with assumed constant properties, is initially flying steadily at a Mach Number of 1.4 at a constant altitude. It is suddenly subjected to a constant acceleration until it reaches a Mach Number of 6 and then is flown steadily at a Mach Number of 6. The two-dimensional heat flow in this wing was solved first in this study to obtain the transient temperature distribution in the wing. It was also shown that the two-dimensional heat-flow problem could be reduced to the solution of a series of one-dimensional heat flows at various positions along the chord of this wing. Both types of solutions were based on integration of the heat-flow equations by laborious numerical methods. The present analytical solution has been sought as a means of reducing significantly the labor of computations to get reasonable answers in a reasonable time.

The reader is referred to the previous study for the values of the properties of steel, for the variation of surface coefficient of heat transfer with position and with time or Mach Number, and for other details such as recovery factors used and variation of adiabatic wall temperatures with speed. For this reason only a minimum amount of repetition will be used in the examples taken from this study to illustrate the present analytical solutions.

Examples Illustrating Use of Design Charts

Example 1

Consider the wedge-shaped wing of the previous study[1] shown in Fig. 1 flying steadily at a Mach Number of 1.4 at an altitude of 50,000 ft.; suddenly it is accelerated to a Mach Number of 6 at a constant acceleration of 2 Mach Numbers per min. and then flown steadily at a Mach Number of 6. The half-thickness of the wing at 2 ft. from the leading edge is 0.10 ft. The problem is to determine the transient temperature distribution normal to the chord at 2 ft. from the leading edge as the Mach Number changes from 1.4 to 6. For purposes of illustration, only the temperature distribution when the wing first reaches a Mach Number of 6 will be computed here, since the analytical solution can be applied immediately to solve the problem for any instant of time without going through the entire history of solutions up to that time, as required in the laborious numerical integrations.

Solution by the Design Charts

From the previous study, the variation of the surface coefficient of heat transfer at 2 ft. from the leading edge is given by the approximate expression,

$$h = 25M - 15 \tag{a}$$

But

$$M = M_b + d\vartheta \tag{b}$$

where d is the acceleration. Hence, combining Eqs. (a) and (b)

$$h = 20 + 5\vartheta/6 \tag{c}$$

where ϑ is in seconds, and Eq. (c) is of the form of Eq. (17). When the properties of steel are inserted in Eq. (18), together with Eq. (c), we get

$$C = al/k + (bl^3/k\alpha)X$$

$$= 20 \times 0.1/22 +$$

$$[(5/6)(0.1 \times 0.1 \times 0.1 \times 3600)/(22 \times 0.384)]\,X$$

$$= 0.09091 + 0.3551\,X \tag{d}$$

where $C_0 = 0.09091$ and $C_1 = 0.3551$. The time of flight is $(6.0 - 1.4)/2 = 2.3$ min. Hence

$$X = \alpha\vartheta/l^2 = (0.384 \times 2.3)/(0.01 \times 60)$$

$$= 1.472$$

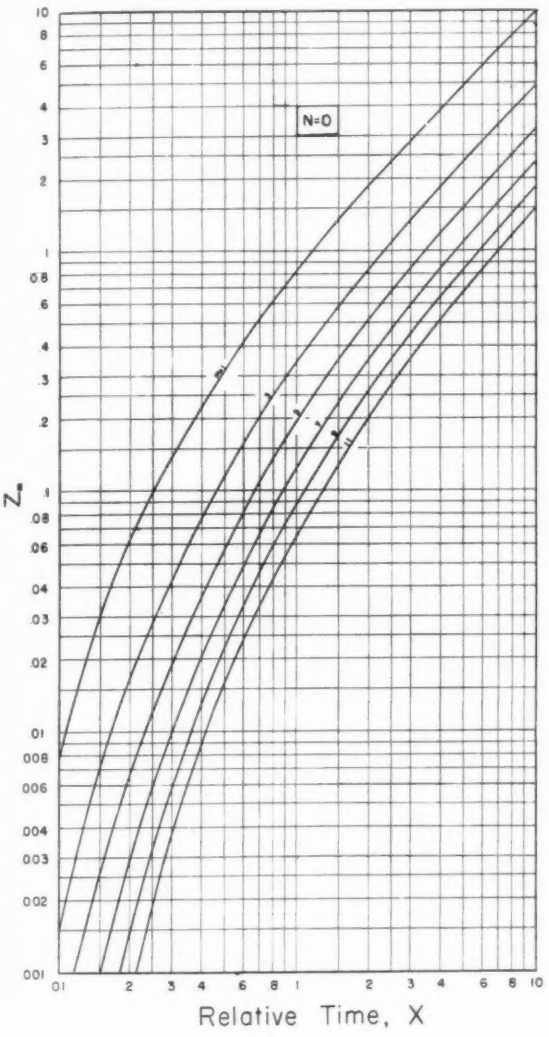

FIG. 8.

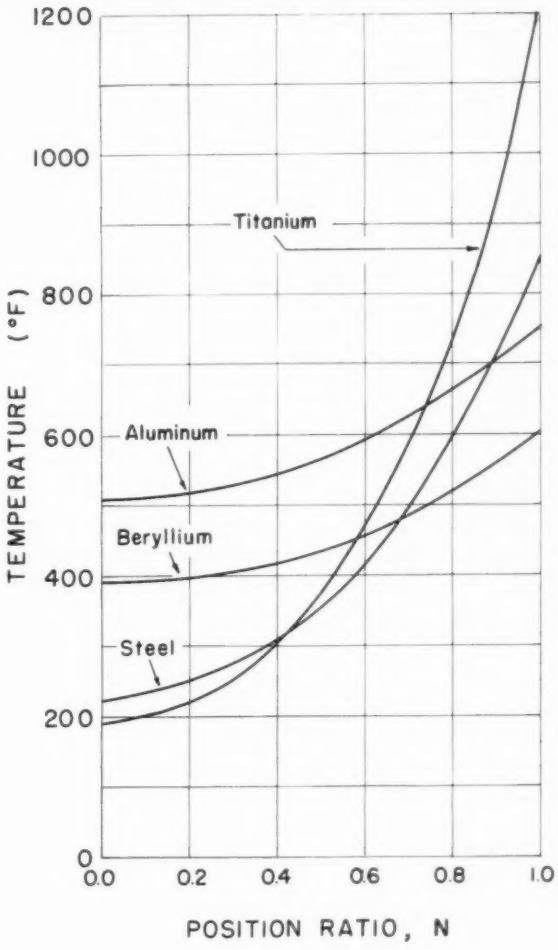

FIG. 9.

TABLE 1

Temperature Distribution at 2 feet from Leading Edge at Instant Mach 6 is Reached

	N=1	0.8	0.6	0.4	0.2	0
Z_2	1.050	0.875	0.744	0.652	0.600	0.582
Z_6	0.793	0.627	0.493	0.412	0.357	0.347
C_0Z_2	0.09546	0.07955	0.06764	0.05927	0.05455	0.05291
C_1XZ_2	0.4145	0.3278	0.2577	0.2154	0.1866	0.1814
Y	0.5100	0.4073	0.3253	0.2746	0.2412	0.2343
t_r (°F)	725.8	579.7	463.0	390.9	343.2	333.5
t_s (°F)	797	651	535	463	415	405
t_s'(°F)	792	643	530	445	---	394

TABLE 2

Properties of Materials and Constants for Example 2

Values	Aluminum Alloy (75ST)	Beryllium	Steel (Mild)	Titanium
Approx. M.P.(°F)	1250	2350	2750	3300
k (Btu/ft hr °F)	70	92	22	8.8
ρ (lbm/ft^3)	173	114	486	276
c_p(Btu/lbm °F)	0.23	0.52	0.118	0.13
α (ft^2/hr)	1.76	1.55	0.384	0.245
C_1	0.1183	0.1022	1.726	6.763

TABLE 3

Temperature Distribution At Instant Mach 6 is Reached in Wing of Example 2

		Aluminum	Beryllium	Steel	Titanium
X		2.999	2.641	0.6542	0.4174
Z_5	N=1	1.320	1.200	0.494	0.390
	0.8	1.148	1.025	.330	.231
	0.6	0.995	0.874	.221	.137
	0.4	.915	.800	.152	.0808
	0.2	.853	.734	.113	.0515
	0	.844	.728	.0975	.0405
$Y = C_1XZ_5$	N=1	0.4684	0.3240	0.5578	1.1009
	0.8	.4074	.2768	.3726	0.6521
	0.6	.3531	.2360	.2495	.3867
	0.4	.3247	.2160	.1716	.2281
	0.2	.3027	.1982	.1276	.1454
	0	.2995	.1966	.1101	.1143
τ(°F)	N=1	685.5	525.9	769.5	1126.1
	0.8	596.2	449.2	514.0	667.0
	0.6	516.8	383.0	344.2	395.6
	0.4	475.2	350.6	236.8	233.3
	0.2	443.0	321.7	176.0	148.7
	0	438.3	319.1	151.9	116.9
t(°F)	N=1	757	598	841	1198
	0.8	668	521	586	739
	0.6	588	455	416	467
	0.4	547	422	308	305
	0.2	515	393	248	220
	0	510	391	224	189

The desired solution is of the form of Eq. (40). Hence

$$Y = C_0Z_3 + C_1XZ_5 \tag{40}$$

so that Z_3 and Z_5 are found from each of the six design charts, Figs. 3–8, for the above value of X, and then the value of Y is obtained from Eq. (40) at each of the six position ratios in the wing. The values of Y are then combined as in Eqs. (42) and (44), to obtain the temperature rise,

$$\tau_1 = \tau_{aw}Y_1/(1 + Y_1) \tag{42}$$

$$\tau_N = \tau_{aw}Y_N/(1 + Y_1) \tag{44}$$

from the adiabatic temperature potential, for a recovery factor of 0.9, as used in the previous study[1]

$$\tau_{aw} = 2{,}220.7 - 71.7$$

$$= 2{,}149°\text{F}.$$

These calculations are summarized in Table 1.

The results of the numerical integration for the same problem, on a one-dimensional heat-flow basis, are shown in the bottom row of Table 1, labeled t'. The temperatures calculated with the aid of the design charts agree with the previously calculated temperatures, t', within the accuracy of the reading of the present design charts and within the accuracy of the finite-difference process used in the numerical integration with the relatively coarse network. For engineering purposes, both sets of temperatures represent excellent answers to the problem, but those based on the charts required only a small fraction of the time used to get the results based on the numerical integrations of the one-dimensional heat-flow equations.

The values of the Z functions shown in Table 1 were read from the original master charts with a maximum error of 2 or 3 digits in the third significant figure when the value of Z is less than unity. However, the values of the Z functions, read from Figs. 3 to 8, will have maximum reading errors of the order of five to eight digits in the third significant figure of Z. Where greater reading accuracy is warranted, tables of the Z functions with proper interpolation rules can be prepared.

It is evident that the analytical solution, based on the one-dimensional heat flow, can be used to predict with excellent accuracy the transient temperature distribution in the wing which results from two-dimensional heat flow, except near the leading and trailing edges. This result is based on the work done in the previous study[1] which showed that the calculations based on the one-dimensional heat flow agreed well with those based on two-dimensional heat flow. Hence the present design charts could be used to obtain the results of the previous study[1] in a much shorter period of time.

Example 2

Consider the wedge-shaped wing to be made from four different metals, such as aluminum alloy, beryllium, steel, and titanium. Initially the wing is flying steadily at a Mach Number of 1.4 at an altitude of 50,000 ft. and then is accelerated at a rate of 2 Mach Numbers per min. to a Mach Number of 6 and finally flown steadily at 6. At the point in question along the chord, the half-thickness is 0.15 ft., and the local heat-transfer coefficient is given approximately by

$$h = 36\,(M - 1.4)$$

Calculate the local temperature distribution when the wing just reaches a Mach Number of 6.

Table 2 summarizes the properties of the different metals used and also the values of C_1 of Eq. (40). Note that Eq. (40) reduces to a single term in the final solution for this particular example, since C_0 is zero. This simplification is a result of the particular linear form used above for the approximate relation between h and M.

Table 3 summarizes the calculation of the temperature distributions for the four materials, using the scheme described in detail in Example 1. The comparison of the temperature distributions is shown in Fig. 9. The important fact to be noticed in Fig. 9 is that the engineering results can be obtained quickly from the design charts at any instant of time without having to solve the entire history of the transient temperature.

Conclusions

Design charts have been prepared to permit rapid and reasonable estimates of the transient temperature distribution for many practical situations arising from aerodynamic heating at supersonic speeds. These design charts were prepared from the analytical solution for the one-dimensional heat flow in a solid body of constant properties when the local surface coefficient of heat transfer is a strong function of time and when

(*Continued on page 786*)

Gas Dynamic Behavior of Real Gases*

L. N. TAO†
Worthington Corporation

SUMMARY

Gas dynamic problems of real gases can be treated in a most general way by the use of the Beattie-Bridgeman equation of state and a specific heat depending upon temperature and pressure based on the spectroscopic measurements. The results in the form of gas dynamic relations between gas properties and geometrical quantities determining the flow configuration may be presented in terms of specified constants with the Crocco Number as independent variable.

(I) INTRODUCTION

IN THE TREATMENT OF GAS dynamic problems it is often assumed that the behavior of the medium is that of a perfect gas. In order to improve the accuracy of the solution for real gases, several investigators have treated the relations of the isentropic flow and the Rankine-Hugoniot flow through plane shock by means of various assumptions. By considering deviations from both definitions of a perfect gas, Tsien[1] and Eggers[2] have obtained the results for one-dimensional flow problems based on Van der Waals' and Berthelot's equations, respectively. Dealing with the variable specific heat, Tsien suggested a quadratic function of temperature for air only, and Eggers used an equation suitable for diatomic gases. While neglecting the deviation due to the thermal imperfectness, Durham[3] derived results for air with the Boyle-Charles equation of state and the mean value of the variable specific heat, and Korst[4] supplemented the result in dealing with the problems of two-dimensional shock configuration. Other attempts were based upon approximating special processes for a real gas: Walker[5] analyzed the problem on the discharge of gases through an orifice or nozzle employing an adiabatic equation $pv^m e^{\lambda T}$ = constant instead of pv^k = constant. Traupel[6] attacked the problems of a real gas by assuming that the compressibility factor of a gas can be considered as a constant for constant entropy, but this concept cannot be applied generally, since not all gases lend themselves to such an approximation.

In the present investigation for improving the accuracy in gas dynamic problems of the isentropic flow and normal and oblique shocks of real gases, a more generalized concept is introduced so that it may be applied to any gases. The Beattie-Bridgeman equation of state[7] is used as the thermodynamic relation of pressure, temperature, and density. Values of the specific heat as a function of temperature and pressure are obtained from spectroscopic data and the use of the Beattie-Bridgeman equation of state and represented in a descending polynomial. The gas dynamic relations are in a generalized manner in terms of the specific heat equation; these then may be applied to any gas after introducing proper numerical values for that gas.

Received October 19, 1954.

* This is abstracted from a doctoral dissertation submitted by the author in the Mechanical Engineering Department, University of Illinois.

† Formerly, Research Engineer. Now, Assistant Professor, Department of Mechanics, Illinois Institute of Technology.

(II) BEHAVIOR OF REAL GASES

Based on classical thermodynamics the real gas differs from an ideal gas in two significant ways, known as the thermal imperfectness and caloric imperfectness.

(A) The Equation of State

It is recognized that the simple equation of state for a perfect gas is only a first approximation for the behavior of the actual gas. Hence many modifications have been suggested; more than 50 equations[8] have been proposed to represent the actual gaseous behavior with closer agreement. Up to now it seems impossible to express the complete behavior of a substance over the entire range of the measured pressure and temperature with a simple equation.

Due to the impossibility of establishing a complete equation through the whole ranges, the empirical or semi-empirical equations arose. In the engineering field the most widely used equation by researchers is the Beattie-Bridgeman[7]

$$p = RT\rho^2(1 - \epsilon)\,[(1/\rho) + B] - A\rho^2 \qquad (1)$$

with

$$\epsilon = c\rho/T^3$$

$$B = B_0(1 - b\rho)$$

and

$$A = A_0(1 - a\rho)$$

This equation gives satisfactory results for the thermodynamic properties of real gases and fluids. This expression for the pressure-volume-temperature relationship over a wide range of temperatures and pressures gives 0.1 per cent to 0.2 per cent deviation for most gases. Hence this equation is used extensively here as the equation of state. The constants in the Beattie-Bridgeman equation have been determined for a number of common gases. Even though this equation is used for some uncommon gases and their numerical constants are not available, the constants may be evaluated approximately from the critical data by the suggestion of Maron and Turnbull[9] with the assumption

that the activity coefficient for most gases is the same at the same reduced pressure and temperature.

(B) *The Specific Heats*

To supplement the purely thermodynamic methods of finding the specific heats, in most cases superseded by methods based on the statistical molecular theory, the required molecular properties of gases may be derived from the analysis of their spectra. The spectral data give essentially the various possible energy levels of the given kind of molecule, and the statistical molecular theory provides a general law of the distribution of molecules among energy states. By the introduction of certain generalizations taken from quantum mechanics, the statistical method may be applied satisfactorily even when lacking detailed knowledge of the spectrum. These theoretical values of C_p and C_v are in excellent agreement with the best known experimental data.

As suggested by Kelly[10] it is possible to represent the molal heat capacities of most gases empirically over a wide range of temperature by means of three-constant equations of the form

$$C_{v_0} = a_1 + (a_2/T) + (a_3/T^2) \tag{2}$$

Such an equation, with empirically determined constants, can be fitted to the experimental data in many cases with a precision of one per cent over a range from 273°K. up to 1,000°K. Using the thermodynamic identities

$$(\partial C_p/\partial p)_T = -T(\partial^2 v/\partial T^2)_p$$
$$(\partial C_v/\partial v)_T = T(\partial^2 p/\partial T^2)_v \tag{3}$$

and integrating at constant temperature, we find

$$C_p = C_{p_0} - \int T\,(\partial^2 v/\partial T^2)_p\,dp \tag{4}$$
$$C_v = C_{v_0} + \int T\,(\partial^2 p/\partial T^2)_v\,dv \tag{5}$$

where C_{p_0} and C_{v_0} are functions of temperature only, and physically they are the corresponding values at zero pressure. Their relationship may be expressed as

$$C_{p_0} - C_{v_0} = R$$

and the integral parts of Eq. (5) may be determined by introducing the equation of state. Here applying the Beattie-Bridgeman equation of state, it becomes

$$C_p = C_{p0} + [(2A_0p)/(RT^2)] + (12cp/T^4) + [(Dp^2)/(RT^2)] - [(3Ep^3)/(R^2T^3)] \tag{6}$$

$$C_v = C_{v0} + f(v, T) = C_{v0} + (6c\rho R/T^3) \tag{7}$$

(III) Analysis

(A) *Isentropic Flow*

For the isentropic case from the basic equations of fluid flow we get

$$C_v dT + T(\partial p/\partial T)_\rho\, d(1/\rho) = 0$$

or

$$C_v dT - (T/\rho^2)\,(\partial p/\partial T)_\rho\, d\rho = 0 \tag{8}$$

The Beattie-Bridgeman equation is introduced in the form

$$p = \rho RT\,[1 - (c\rho/T^3)]\,(1 + B_0\rho - B_0b\rho^2) - A_0\rho^2(1 - a\rho)$$

or

$$= \rho RT[1 - (c\rho/T^3)]\,(1 + B_0\rho - D\rho^2) - (A_0\rho^2 - E\rho^3) \tag{9}$$

with $D = B_0b$ and $E = A_0a$. Hence $(\partial p/\partial T)_\rho$ may be derived from this equation and substituted into Eq. (8)

$$C_v dT - (RT/\rho)\,(1 + B_0\rho - D\rho^2)\,\rangle\,[1 + (2c\rho/T^3)]d\rho = 0 \tag{10}$$

Also, as discussed in the previous section we may write

$$C_v = C_{v_0} + f(v, T) = a_1 + (a_2/T) + (a_3/T^2) + (6c\rho R/T^3)$$
$$= C_i[1 + \alpha + (\beta/T) + (\gamma/T^2) + (6c\rho R/C_iT^3)] \tag{11}$$

where C_i is a constant that has the same value as the reference constant specific heat. With this, Eq. (11) becomes

$$C_i\{1 + \alpha + (\beta/T) + (\gamma/T^2) + [(6c\rho R)/(C_iT^3)]\}dT - (RT/\rho) \times (1 + B_0\rho - D\rho^2)\,[1 + (2c\rho/T^3)]d\rho = 0 \tag{12}$$

In classical thermodynamics any thermodynamic property of a pure substance may be expressed explicitly as a function of two other properties—e.g., $T = T(\rho, S)$. In the present case where the entropy is constant, it follows that for a specified entropy any property may be expressed explicitly by another single variable, $T = T(\rho)$.

Since all the terms inside the braces and brackets of Eq. (12) are rather small quantities in comparison with unity, the well known "perturbation approach" method is now applied. It is assumed that all the high-order terms, which actually appear in dimensionless quantities, are neglected, so that the solution of Eq. (12) presents itself as

$$T(\rho) = T_0(\rho) + \alpha T_\alpha(\rho) + \beta T_\beta(\rho) + \gamma T_\gamma(\rho) + B_0T_{B_0}(\rho) + DT_D(\rho) + cT_c(\rho) \tag{13}$$

This is substituted into Eq. (12). Since all the coefficients are independent of each other, the following set of equations must hold true.

$$C_i dT_0 - (R/\rho)T_0 d\rho = 0 \tag{14}$$
$$C_i(dT_\alpha + dT_0) - (R/\rho)T_\alpha d\rho = 0 \tag{15a}$$
$$C_i[dT_\beta + (dT_0/T_0)] - (R/\rho)T_\beta d\rho = 0 \tag{15b}$$
$$C_i[dT_\gamma + (dT_0/T_0^2)] - (R/\rho)T_\gamma d\rho = 0 \tag{15c}$$
$$C_i dT_{B_0} - (R/\rho)\,(T_{B_0} + \rho T_0)d\rho = 0 \tag{15d}$$
$$C_i dT_D - (R/\rho)\,(T_D - \rho^2 T_0)d\rho = 0 \tag{15e}$$
$$C_i dT_c + (6\rho R/T_0^3)dT_0 - (R/\rho)\,[T_c + (2\rho/T_0^2)]d\rho = 0 \tag{15f}$$

These linear equations are solved and Eq. (13) becomes

$$T = \lambda\rho^{k-1} - \alpha\lambda(k-1)\rho^{k-1}\log\rho + \beta + (\gamma/(2\lambda\rho^{k-1})] + B_0(k-1)\lambda\rho^k - D[(k-1)/2]\lambda\rho^{k+1} + C(2/\lambda^2)(k-1)D\rho^{3-2k} \quad (16)$$

where λ is an integration constant and $k = 1 + (R/C_v)$. With the initial condition T_0 and ρ_0 the complete solution is

$$\frac{T}{T_0} = \left(\frac{\rho}{\rho_0}\right)^{k-1}\left\{1 - \alpha(k-1)\log\frac{\rho}{\rho_0} - \frac{\beta}{T_0}\left[1 - \left(\frac{\rho}{\rho_0}\right)^{1-k}\right] - \frac{\gamma}{2T_0}\left[1 - \left(\frac{\rho}{\rho_0}\right)^{2-2k}\right] - B_0\rho_0(k-1)\left(1 - \frac{\rho}{\rho_0}\right) + D\rho_0^2\frac{k-1}{2}\left[1 - \left(\frac{\rho}{\rho_0}\right)^2\right] - \frac{2c\rho_0}{T_0^3}(k-1)\left[1 - \left(\frac{\rho}{\rho_0}\right)^{4-3k}\right]\right\} \quad (17)$$

To represent ρ/ρ_0 in terms of T/T_0, we get

$$\frac{\rho}{\rho_0} = \left(\frac{T}{T_0}\right)^{1/(k-1)}\left\{1 + \alpha\frac{1}{k-1}\log\frac{T}{T_0} + \frac{\beta}{T_0}\frac{1}{k-1}\left[1 - \left(\frac{T}{T_0}\right)^{-1}\right] + \frac{\gamma}{T_0^2}\frac{1}{2(k-1)}\left[1 - \left(\frac{T}{T_0}\right)^{-2}\right] + B_0\rho_0\left[1 - \left(\frac{T}{T_0}\right)^{1/(k-1)}\right] - \frac{D\rho_0^2}{2}\left[1 - \left(\frac{T}{T_0}\right)^{2/(k-1)}\right] + \frac{2c\rho_0}{T_0^3}\left[1 - \left(\frac{T}{T_0}\right)^{(4-3k)/(k-1)}\right]\right\} \quad (18)$$

Also with the aid of the equation of state, we get the following equations

$$\frac{p}{p_0} = \left(\frac{\rho}{\rho_0}\right)^k\left\{1 - \alpha(k-1)\log\frac{\rho}{\rho_0} - \frac{\beta}{T_0}\left[1 - \left(\frac{\rho}{\rho_0}\right)^{1-k}\right] - \frac{\gamma}{T_0^2}\frac{1}{2}\left[1 - \left(\frac{\rho}{\rho_0}\right)^{2-2k}\right] - B_0\rho_0 k\left(1 - \frac{\rho}{\rho_0}\right) + D\rho_0^2\frac{k+1}{2}\left[1 - \left(\frac{\rho}{\rho_0}\right)^2\right] + \frac{c\rho_0}{T_0^3}(3-2k)\left[1 - \left(\frac{\rho}{\rho_0}\right)^{4-3k}\right] + \frac{A_0\rho_0}{RT_0}\left[1 - \left(\frac{\rho}{\rho_0}\right)^{2-k}\right] - \frac{E\rho_0^2}{RT_0}\left[1 - \left(\frac{\rho}{\rho_0}\right)^{3-k}\right]\right\} \quad (19)$$

$$\frac{\rho}{\rho_0} = \left(\frac{p}{p_0}\right)^{1/k}\left\{1 + \alpha\frac{k-1}{k^2}\log\frac{p}{p_0} + \frac{\beta}{T_0}\frac{1}{k}\left[1 - \left(\frac{p}{p_0}\right)^{(1-k)/k}\right] + \frac{\gamma}{T_0^2}\frac{1}{2k}\left[1 - \left(\frac{p}{p_0}\right)^{[2(1-k)]/k}\right] + B_0\rho_0\left[1 - \left(\frac{p}{p_0}\right)^{1/k}\right] - D\rho_0^2\frac{k+1}{2k}\left[1 - \left(\frac{p}{p_0}\right)^{2/k}\right] - \frac{c\rho_0}{T_0^3}\frac{3-2k}{k}\left[1 - \left(\frac{p}{p_0}\right)^{(4-3k)/k}\right] - \frac{A_0\rho_0}{RT_0}\frac{1}{k}\left[1 - \left(\frac{p}{p_0}\right)^{(2-k)/k}\right] + \frac{E\rho_0^2}{RT_0}\frac{1}{k}\left[1 - \left(\frac{p}{p_0}\right)^{(3-k)/k}\right]\right\} \quad (20)$$

Similarly,

$$\frac{p}{p_0} = \left(\frac{T}{T_0}\right)^{k/k-1}\left\{1 + \alpha\frac{1}{k-1}\log\frac{T}{T_0} + \frac{\beta}{T_0}\frac{1}{k-1}\left[1 - \left(\frac{T}{T_0}\right)^{-1}\right] + \frac{\gamma}{T_0^2}\frac{1}{2(k-1)}\left[1 - \left(\frac{T}{T_0}\right)^{-2}\right] + \frac{D\rho_0^2}{2}\left[1 - \left(\frac{T}{T_0}\right)^{2/(k-1)}\right] + \frac{3c\rho_0}{T_0^3}\left[1 - \left(\frac{T}{T_0}\right)^{(4-3k)/(k-1)}\right] + \frac{A_0\rho_0}{RT_0}\left[1 - \left(\frac{T}{T_0}\right)^{(2-k)/(k-1)}\right] - \frac{E\rho_0^2}{RT_0}\left[1 - \left(\frac{T}{T_0}\right)^{(3-k)/(k-1)}\right]\right\} \quad (21)$$

and

$$\frac{T}{T_0} = \left(\frac{p}{p_0}\right)^{(k-1)/k}\left\{1 - \alpha\frac{k-1}{k^2}\log\frac{p}{p_0} - \frac{\beta}{T_0}\frac{1}{k}\left[1 - \left(\frac{p}{p_0}\right)^{(1-k)/k}\right] - \frac{\gamma}{T_0^2}\frac{1}{2k}\left[1 - \left(\frac{p}{p_0}\right)^{[2(1-k)]/k}\right] - \frac{D\rho_0^2}{2}\frac{k-1}{k}\left[1 - \left(\frac{p}{p_0}\right)^{2/k}\right] - \frac{c\rho_0}{T_0^3}\frac{3(k-1)}{k}\left[1 - \left(\frac{p}{p_0}\right)^{(4-3k)/k}\right] - \frac{k-1}{k}\frac{A_0\rho_0}{RT_0}\left[1 - \left(\frac{p}{p_0}\right)^{(2-k)/k}\right] + \frac{E\rho_0^2}{RT_0}\frac{k-1}{k}\left[1 - \left(\frac{p}{p_0}\right)^{(3-k)/k}\right]\right\} \quad (22)$$

In these equations if all the correction coefficients that exist in dimensionless quantity forms are zero, then those equations are reduced to those for a perfect gas.

For the explanation of such an isentropic flow, the characteristics and properties of a "Laval nozzle" are analyzed. First, from the energy principle and Eq. (18) we obtain

$$udu + d(p/\rho) + \{(pC_v dT)/[T(\partial p/\partial T)_\rho]\} = 0 \quad (23)$$

With the expressions for $(\partial p/\partial T)_\rho$ and C_v, this equation becomes

$$udu + d(p/\rho) + C_v\{1 + \alpha + (\beta/T) + (\gamma/T^2) - 3(3-2k)(C\rho/T^3) - [(A_0\rho)/(RT)] + [(E\rho^2)/(RT)]\}dT = 0 \quad (24)$$

Integration of this equation with the initial condition $u = 0$ at $T = T_0$ gives

$$\frac{1}{2}u^2 = \left(\frac{p_0}{\rho_0} - \frac{p}{\rho}\right) + T_0 C_i \left\{\left(1 - \frac{T}{T_0}\right) + \alpha\left(1 - \frac{T}{T_0}\right) - \frac{\beta}{T_0}\log\frac{T}{T_0} - \frac{\gamma}{T_0^2}\left[1 - \left(\frac{T}{T_0}\right)^{-1}\right] - \frac{3c\rho_0}{T_0^3}(k-1)\left[1 - \left(\frac{T}{T_0}\right)^{(3-2k)/(k-1)}\right] - (k-1)\frac{A_0\rho_0}{RT_0}\left[1 - \left(\frac{T}{T_0}\right)^{1/(k-1)}\right] + \frac{k-1}{2}\frac{E\rho_0^2}{RT_0}\left[1 - \left(\frac{T}{T_0}\right)^{2/(k-1)}\right]\right\} \quad (25)$$

Now we introduce the so-called "Crocco Number," which is defined as the ratio of the local velocity to the "Laval velocity"[11] or the maximum velocity attainable in the same direction. In the one-dimensional problems it is

$$W = u/u_{max} = u/[2\int c_p dT]^{1/2} = u/\{u^2 + [2/(k-1)]u_s^2\}^{1/2} \quad (26)$$

and its relation to the Mach Number is

$$M^2 = [2/(k-1)]\,[W^2/(1-W^2)] \quad (27)$$

or

$$W^2 = 1 - (1/\{1 + [(k-1)/2]M^2\}) \quad (28)$$

Such a variable is used because it transforms the infinite range of Mach Number to a range between zero and unity. Also it is rather widely spaced at the low speed, and hence, it gives less calculation error. Furthermore, it is simpler to handle in the derivation of formulas.

Before introducing the Crocco Number, the sonic velocity should be found. By the formula $u_s = (dp/d\rho)^{1/2}$ we find

$$u_s^2 = \frac{dp}{d\rho} = k\frac{p_0}{\rho_0}\left(\frac{\rho}{\rho_0}\right)^{k-1}\left\{1 - \alpha\frac{k-1}{k}\left(1 + k\log\frac{\rho}{\rho_0}\right) - \frac{\beta}{T_0}\left[1 - \frac{1}{k}\left(\frac{\rho}{\rho_0}\right)^{1-k}\right] - \frac{\gamma}{T_0^2}\frac{1}{2}\left[1 - \frac{2-k}{k}\left(\frac{\rho}{\rho_0}\right)^{2-k}\right] - B_0\rho_0 k\left(1 + \frac{k+1}{k}\frac{\rho}{\rho_0}\right) + D\rho_0^2\left[1 - \frac{k+2}{k}\left(\frac{\rho}{\rho_0}\right)^2\right] + \frac{c\rho_0}{T_0^3}(3-2k)\left[1 - \frac{4-2k}{k}\left(\frac{\rho}{\rho_0}\right)^{4-2k}\right] + \frac{A_0\rho_0}{RT_0}\left[1 - \frac{2}{k}\left(\frac{\rho}{\rho_0}\right)^{2-k}\right] - \frac{E\rho_0^2}{RT_0}\left[1 - \frac{3}{k}\left(\frac{\rho}{\rho_0}\right)^{3-k}\right]\right\} \quad (29)$$

The local sonic velocity is obtained simply by moving the reference point to the local state and is evaluated at this reference state, $p_0 = p$, $\rho_0 = \rho$, and $T_0 = T$. So it becomes

$$u_s^2 = k\frac{p}{\rho}\left[1 - \alpha\frac{k-1}{k} - \frac{\beta}{T}\frac{k-1}{k} - \frac{\gamma}{T^2}\frac{k-1}{k} + B_0\rho - D\rho^2\frac{k+1}{k} - \frac{c\rho}{T^3}\frac{(3-2k)(4-3k)}{k} - \frac{A_0\rho}{RT}\left(\frac{2-k}{k}\right) + \frac{E\rho^2}{RT}\left(\frac{3-k}{k}\right)\right] \quad (30)$$

With Eqs. (24), (25), (26), and (30), a relation between temperature and Crocco Number is found.

$$T/T_0 = (1 - W^2)\{1 + \alpha_1 t_1 + (\beta/T_0)t_2 + (\gamma/T_0^2)t_3 + B_0\rho_0 t_4 + D\rho_0^2 t_5 + (c\rho_0/T_0^3)t_6 + [(A_0\rho_0)/(RT_0)]t_7 + [(E\rho_0^2)/(RT_0)]t_8\} \quad (31)$$

For abbreviations let us put these dimensionless expressions $\alpha = z_1$, $\beta/T_0 = z_2$, $\gamma/T_0^2 = z_3$, $B_0\rho_0 = z_4$, $D\rho_0^2 = z_5$, $c\rho_0/T_0^3 = z_6$, $(A_0\rho_0)/(RT_0) = z_7$, and $(E\rho_0^2) \div (RT_0) = z_8$. Then

$$\frac{T}{T_0} = (1 - W^2)\left(1 + \sum_{i=1}^{8} z_i t_i\right) \quad (32)$$

where

$$t_1 = W^2$$

$$t_2 = [(k-1)/k]\,[W^2/(1-W^2)] - (1/k)\log(1-W^2)$$

$$t_3 = (1/k)\,[W^2(k-W^2)]/(1-W^2)^2\}$$

$$t_4 = [(k-1)/k] - 2(1-W^2)^{1/(k-1)} + [(k+1)/k](1-W^2)^{k/(k-1)}$$

$$t_5 = [(1-k)/k] + [2 + (1/k)](1-W^2)^{2/(k-1)} - [1 + (2/k)](1-W^2)^{(k+1)/(k-1)}$$

$$t_6 = \{[4(1-k)]/k\} + \{[(3-2k)(4-3k)]/k\} \times (1-W^2)^{(4-3k)/(k-1)} - \{[(4-3k)(2-k)]/k\} \times (1-W^2)^{(3-2k)/(k-1)}$$

$$t_7 = [(1-k)/k] + (2/k)(1-W^2)^{(2-k)/(k-1)} + [1 - (3/k)](1-W^2)^{1/(k-1)}$$

$$t_8 = [(k-1)/2k] - (3/k)(1-W^2)^{(3-k)/(k-1)} + \{[7/2k] - (1/2)\}(1-W^2)^{2/(k-1)}$$

By the substitution of Eq. (31) into Eqs. (21) and (18) the following equations are obtained.

$$\frac{p}{p_0} = (1 - W^2)^{k/(k-1)}\left(1 + \sum_{i=1}^{8} z_i \pi_i\right) \quad (33)$$

where

$$\pi_1 = [k/(k-1)]t_1 + [1/(k-1)]\log(1-W^2)$$

$$\pi_2 = [k/(k-1)]t_2 - [1/(k-1)]\,[W^2/(1-W^2)]$$

$$\pi_3 = [k/(k-1)]t_3 + [1/(k-1)] \times \{1 - [1/(1-W^2)^2]\}$$

$$\pi_4 = [k/(k-1)]t_4$$

$$\pi_5 = [k/(k-1)]t_5 + (1/2) - (1/2)(1-W^2)^{2/k-1}$$

$$\pi_6 = [k/(k-1)]t_6 + 3 - 3(1-W^2)^{(4-3k)/(k-1)}$$

$$\pi_7 = [k/(k-1)]t_7 + 1 - (1-W^2)^{(2-k)/(k-1)}$$

$$\pi_8 = [k/(k-1)]t_8 - 1 + (1-W^2)^{(3-k)/(k-1)}$$

and

$$\frac{\rho}{\rho_0} = (1 - W^2)^{1/(k-1)} \left(1 + \sum_{i=1}^{8} z_i d_i\right) \qquad (34)$$

where

$$d_1 = [t_1/(k-1)] + [1/(k-1)] \log (1 - W^2)$$
$$d_2 = [t_2/(k-1)] - [1/(k-1)]\,[W^2/(1 - W^2)]$$
$$d_3 = [t_3/(k-1)] + \{1/[2(k-1)]\} \times \{1 - [1/(1 - W^2)^2]\}$$
$$d_4 = [t_4/(k-1)] + 1 - (1 - W^2)^{1/(k-1)}$$
$$d_5 = [t_5/(k-1)] - (1/2) + (1/2)\,(1 - W^2)^{2/(k-1)}$$
$$d_6 = [t_6/(k-1)] + 2 - 2(1 - W^2)^{(4-2k)/(k-1)}$$
$$d_7 = t_7/(k-1)$$
$$d_8 = t_8/(k-1)$$

As the correction factors are evaluated with the numerical values for a specific gas, the deviation of the real gas from the perfect gas can be determined. If all the correction coefficients vanish, these equations will be reduced to the well-known formulas for perfect gas.

Furthermore, in the one-dimensional isentropic flow through a Laval nozzle the cross-sectional area and the wall force function also play important roles. They are analyzed in the following: From the continuity equation we get

$$d(\rho u) = 0 \qquad (35)$$

For convenience in application the reference point is taken from the critical cross section, which is indicated by an asterisk instead of the previous stagnation point. Thus

$$\rho u A = \rho^* u^* A^* \qquad (36a)$$

$$A/A^* = (\rho^*/\rho_0)\,(\rho_0/\rho)\,(W^*/W) \qquad (36b)$$

At this particular section it is easily verified from the energy equation that W^* is equal to $[(k-1)/(k+1)]^{1/2}$. By substitutions of ρ^*/ρ_0 and ρ_0/ρ into Eq. (36b), Eq. (36b) is solved.

$$\frac{A}{A^*} = \frac{1}{W}\left[\frac{k+1}{2}(1 - W^2)\right]^{1/(1-k)} \left(\frac{k-1}{k+1}\right)^{1/2} \times \left(1 + \sum_{i=1}^{8} z_i S_i\right) \qquad (37)$$

where

$$S_1 = [1/(k+1)] + [1/(k-1)] \log [2/(k+2)] - [t_1/(k-1)] - [1/(k-1)] \log (1 - W^2)$$

$$S_2 = -[1/(2k)] - \{1/[k(k-1)]\} \times \log [2/(k+2)] - [t_2/(k-1)] + [1/(k-1)]\,[W^2/(1 - W^2)]$$

$$S_3 = [(k^2+1)/(4k)] - \{(k+1)^2/[8(k-1)]\} - [t_3/(k-1)] + \{(1 - W^2)^{-2}/[2(k-1)]\}$$

$$S_4 = [(k+1)/(2k)] + [2/(k+1)]^{1/k-1} \times [-(k+2)/k] - [t_4/(k-1)] - (1 - W^2)^{1/(k-1)}$$

$$S_5 = -(1/k) + [2/(k+1)]^{2/(k-1)} \times \{[(k+2)\,(k+3)]/[2k(k+1)]\} - [t_5/(k-1)] - (1/2)\,(1 - W^2)^{2/(k-1)}$$

$$S_6 = -(4/k) + [2/(k+1)]^{(4-2k)/(k-1)}\,(3 - 2k) \times (\{(4 - 3k)/[k(k+1)]\} + [1/(k+1)]\}) - [t_6/(k-1)] + 2(1 - W^2)^{(4-3k)/(k-1)}$$

$$S_7 = -(1/k) + [2/(k+1)]^{(2-k)/(k-1)} \times \{4/[k(k+1)]\} - [t_7/(k-1)]$$

$$S_8 = [1/(2k)] - [2/(k+1)]^{(3-k)/(k-1)} \times \{4/[k(k+1)]\} - [t_8/(k-1)]$$

The wall force function F is defined as

$$F = pA + \rho u^2 A \qquad (38)$$

Hence, expressed in dimensionless form it becomes

$$F/F^* = [(p/p_0)/(p^*/p_0)]\,(A/A^*) \{[1 + (\rho u^2/p)]/[1 + (\rho^* u^{*2}/p^*)]\} \qquad (39)$$

Then with the aid of the equation of state we get

$$\frac{\rho u^2}{p} = \frac{2kW^2}{(k-1)(1 - W^2)}\left[1 - \alpha\frac{k-1}{k} - \frac{\beta}{T}\left(\frac{k-1}{k}\right) - \frac{\gamma}{T^2}\left(\frac{k-1}{k}\right) + B_0\rho - D\rho^2\frac{k+1}{k} - \frac{c\rho}{T^3}\frac{(3-2k)\,(4-3k)}{k} - \frac{A_0\rho}{RT}\left(\frac{2}{k} - 1\right) + \frac{E\rho^2}{RT}\left(\frac{3}{k} - 1\right)\right] \qquad (40)$$

Therefore Eq. (39) becomes

$$\frac{F}{F^*} = \frac{(k+1)W^2 + (k-1)}{2W(k^2-1)^{1/2}}\left(1 + \sum_{i=1}^{8} z_i j_i\right) \qquad (41)$$

where

$$j_1 = \pi_1 + S_1 - \frac{1}{k-1}\log\frac{2}{k+1} - \frac{1}{k+1} - \frac{2(k-1)W^2}{(k-1) + (k+1)W^2}$$

$$j_2 = \pi_2 + S_2 + \frac{1}{2} + \frac{1}{k-1}\log\frac{2}{k+1} - \frac{2(k-1)W^2}{(k+1)W^2 + (k-1)}\,\frac{1}{(1 - W^2)}$$

$$j_3 = \pi_3 + S_3 + \frac{k-1}{8} - \frac{2(k-1)W^2}{(k+1)W^2 - (k-1)}\,\frac{1}{(1 - W^2)^2}$$

$$j_4 = \pi_4 + S_4 - 1 + \frac{k+2}{k+1}\left(\frac{2}{k+1}\right)^{1/(k-1)} + \frac{2kW^2}{(k+1)W^2 + (k-1)}\,(1 - W^2)^{1/(k-1)}$$

$$j_5 = \pi_5 + S_5 + \frac{1}{2} - \frac{k+3}{2(k+1)}\left(\frac{2}{k+1}\right)^{2/(k-1)} - \frac{2(k+1)W^2}{(k+1)W^2 + (k-1)}\,(1 - W^2)^{2/(k-1)}$$

$$j_6 = \pi_6 + S_6 + 1 + \left[3 - \frac{2(4-3k)(3-2k)W^2}{(k+1)W^2 + (k-1)}\right](1-W^2)^{(4-3k)/(k-1)}$$

$$j_7 = \pi_7 + S_7 - \left(\frac{1}{k+1}\right)\left(\frac{2}{k+1}\right)^{(2-k)/(k-1)} - \frac{2(2-k)W^2}{(k+1)W^2 + (k-1)}(1-W^2)^{(2-k)/(k-1)}$$

$$j_8 = \pi_8 + S_8 + \frac{1}{2} + \frac{2(3-k)W^2}{(k+1)W^2 + (k-1)} \times (1-W^2)^{(3-k)/(k-1)}$$

(B) The Normal Shock

The continuity equation, the momentum equation, and the energy equation for the one-dimensional shock are

$$\rho_2 u_2 - \rho_1 u_1 = 0 \tag{42a}$$

$$\rho_2 u_2^2 - \rho_1 u_1^2 + p_2 - p_1 = 0 \tag{43a}$$

$$\int C_v dT + \int \left(\frac{\partial I}{\partial v}\right)_T d\left(\frac{1}{\rho}\right) + \frac{p_2}{\rho_2} - \frac{p_1}{\rho_1} + \frac{1}{2}(u_2^2 - u_1^2) = 0 \tag{44a}$$

where subscripts 1 and 2 refer to the upstream and downstream flows, respectively. By introducing the Crocco Number, they become

$$\rho_2 W_2 - \rho_1 W_1 = 0 \tag{42b}$$

$$p_2 - p_1 + u_m^2(\rho_2 W_2^2 - \rho_1 W_1^2) = 0 \tag{43b}$$

$$\int C_v\left[1 + \alpha + \frac{\beta}{T} + \frac{\gamma}{T^2} + 6(k-1)\frac{c\rho}{T^3}\right]dT + \frac{p_2}{\rho_2} - \frac{p_1}{\rho_1} + \frac{3cR\rho_1}{T_1^2} - \frac{3cR\rho_2}{T_2^2} - A_0(\rho_2 - \rho_1) + \frac{E}{2}(\rho_2^2 - \rho_1^2) + \frac{1}{2}u_m^2(W_2^2 - W_1^2) = 0 \tag{44b}$$

The "Laval" velocity can be evaluated from either one of the following equations

$$u_m^2 = 2\int C_p dT$$

or

$$= u_s^2\left(\frac{2}{k-1}\frac{1}{1-W^2}\right) \tag{45}$$

Here the second form is used, since it can be expressed in terms of the properties and the Crocco Number

$$u_m^2 = \frac{2k}{k-1}\frac{1}{1-W_1^2}\frac{p_1}{\rho_1}\left[1 - z_1\frac{k}{k-1} - z_2\frac{k-1}{k} - z_3\frac{k-1}{k} + z_4 - z_5\frac{k+1}{k} - z_6\frac{(3-2k)(4-3k)}{k} - z_7\frac{2-k}{k} + z_8\frac{3-k}{k}\right] \tag{46}$$

Then the three equations with the substitution of "Laval" velocity and the equation of state have four unknowns ρ_2, T_2, p_2, and W_2. Although it is a very tedious procedure, by the elimination of W_2, ρ_2, and T_2, they yield

$$\frac{k}{k-1} - \frac{k}{k-1}\frac{p_2}{p_1} - \left(1 - \frac{p_2}{p_1}\right) - \frac{1-W_1^2}{2W_1^2}\frac{p_2}{p_1}\left(1 - \frac{p_2}{p_1}\right) - \frac{[1-(p_2/p_1)]^2(k-1)(1-W_1^2)}{4kW_1^2} + z_1\left\{-\frac{(k-1)(1-W_1^2)}{2kW_1^2}\frac{p_2}{p_1}\left(1-\frac{p_2}{p_1}\right) + \frac{1}{k-1}\left(1-\frac{p_2}{p_1}\right)\left[1 + \frac{(k-1)(1-W_1^2)}{2kW_1^2}\frac{p_2}{p_1}\right] - \left(1-\frac{p_2}{p_1}\right)^2 \times \frac{(k-1)^2(1-W_1^2)}{4k^2W_1^2}\right\} + z_2\left\{-\frac{(k-1)(1-W_1^2)}{2kW_1^2}\frac{p_2}{p_1}\left(1-\frac{p_2}{p_1}\right) - \frac{1}{k-1}\left(\log\frac{p_2}{p_1}\right)\left[1 + \left(1-\frac{p_2}{p_1}\right) \times \frac{(k-1)(1-W_1^2)}{2kW_1^2}\right] - \left(1-\frac{p_2}{p_1}\right)^2\frac{(k-1)^2(1-W_1^2)}{4k^2W_1^2}\right\} + z_3\left\{-\frac{(k-1)(1-W_1^2)}{2kW_1^2}\frac{p_2}{p_1}\left(1-\frac{p_2}{p_1}\right) - \frac{1}{k-1}\left\{1 - \frac{2kW_1^2}{[1-(p_2/p_1)](k-1)(1-W_1^2)}\right\} - \left(1-\frac{p_2}{p_1}\right)^2\frac{(k-1)^2(1-W_1^2)}{4k^2W_1^2}\right\} + z_4(0) + z_5\left[\frac{k}{k-1}\frac{p_2}{p_1}\left(1 - \left\{\frac{2kW_1^2}{(k-1)(1-W_1^2)[1-(p_2/p_1)] + 2kW_1^2}\right\}^2\right) - \frac{1-W_1^2}{2W_1^2}\frac{p_2}{p_1}\left(1-\frac{p_2}{p_1}\right) \times \left\{\frac{2kW_1^2}{(k-1)(1-W_1^2)[1-(p_2/p_1)] + 2kW_1^2} + \frac{1}{k}\right\} - \frac{p_2}{p_1}\frac{[1-(p_2/p_1)](k-1)(1-W_1^2)}{(k-1)(1-W_1^2)[1-(p_2/p_1)] + 2kW_1^2} - \frac{[1-(p_2/p_1)]^2(k-1)(1-W_1^2)}{4k^2}\right] + z_6\left[\frac{k}{k-1}\frac{p_2}{p_1}\left(1 - \left(\frac{p_1}{p_2}\right)^3 \times \left\{\frac{2kW_1^2}{(k-1)(1-W_1^2)[1-(p_2/p_1)] + 2kW_1^2}\right\}^4\right) - \frac{1-W_1^2}{2W_1^2}\left(1-\frac{p_2}{p_1}\right)\left(\frac{(3-2k)(4-3k)}{k} - 1 + \left\{\frac{2kW_1^2}{(k-1)(1-W_1^2)[1-(p_2/p_1)] + 2kW_1^2}\right\}^4\left(\frac{p_1}{p_2}\right)^2\right) + \left(1-\frac{p_2}{p_1}\right) - \frac{[1-(p_2/p_1)]^2(k-1)(i-W_1^2)}{4kW_1^2} \times$$

$$\left[\frac{(3-2k)(4-3k)}{k}-1\right]-\left\{1-\frac{2kW_1^2}{(k-1)(1-W_1^2)[1-(p_2/p_1)]+2kW_1^2}\left(\frac{p_1}{p_2}\right)\right\}-3\left(1-\left(\frac{p_1}{p_2}\right)^2\times\left\{\frac{2kW_1^2}{(k-1)(1-W_1^2)[1-(p_2/p_1)]+2kW_1^2}\right\}^2\right)-3\left\{1-\frac{2kW_1^2}{(k-1)(1-W_1^2)[1-(p_2/p_1)]+2kW_1^2}\right\}\Bigg]+$$

$$z_7\left[\frac{k}{k-1}\frac{p_2}{p_1}\left(1-\frac{p_1}{p_2}\left\{\frac{2kW_1^2}{(k-1)(1-W_1^2)[1-(p_2/p_1)]+2kW_1^2}\right\}\right)-\frac{1-W_1^2}{2W_1^2}\left(1-\frac{p_2}{p_1}\right)\left(\frac{2}{k}-2+\frac{p_1}{p_2}\left\{\frac{2kW_1^2}{(k-1)(1-W_1^2)[1-(p_2/p_1)]+2kW_1^2}\right\}^2\right)+\left(1-\frac{p_2}{p_1}\right)-\frac{2(k-1)(1-W_1^2)[1-(p_2/p_1)]}{(k-1)(1-W_1^2)[1-(p_2/p_1)]+2kW_1^2}+\frac{[1-(p_2/p_1)]^2(k-1)^2(1-W_1^2)}{2k^2W_1^2}\right]+z_8\left[\frac{k}{1-k}\frac{p_2}{p_1}\times\left\{1-\frac{p_1}{p_2}\frac{2kW_1^2}{(k-1)(1-W_1^2)[1-(p_2/p_1)]+2kW_1^2}\right\}-\frac{1-W_1^2}{2W_1^2}\left(1-\frac{p_2}{p_1}\right)\left(\frac{3}{k}-2+\left\{\frac{2kW_1^2}{(k-1)(1-W_1^2)[1-(p_2/p_1)]+2kW_1^2}\right\}^3\left(\frac{p_1}{p_2}\right)\right)-\left(1-\frac{p_2}{p_1}\right)+\frac{3}{2}\left(1-\left\{\frac{2kW_1^2}{(k-1)(1-W_1^2)[1-(p_2/p_1)]+2kW_1^2}\right\}^2\right)+\left(1-\frac{p_2}{p_1}\right)\frac{(k-1)(3-2k)(1-W_1^2)}{4k^2W_1^2}\right]=0 \quad (47)$$

It is possible to simplify the solution of this equation by ignoring all the high-order terms of these dimensionless correction factors, so that

$$\frac{p_2}{p_1}=\left(\frac{p_2}{p_1}\right)_0+\sum_{i=1}^{8}\left(\frac{p_2}{p_1}\right)_i z_i \quad (48)$$

Substitute this solution into Eq. (47). Since all the z_i's are independent of each other, each of them must equal zero. Equation (47) is now reduced to

$$\frac{k}{k-1}-\frac{k}{k-1}\left(\frac{p_2}{p_1}\right)_0-\frac{1-W_1^2}{2W_1^2}\left(\frac{p_2}{p_1}\right)_0\left[1-\left(\frac{p_2}{p_1}\right)_0\right]-\left[1-\left(\frac{p_2}{p_1}\right)_0\right]-\frac{k-1}{4k}\frac{1-W_1^2}{W_1^2}\left[1-\left(\frac{p_2}{p_1}\right)_0\right]=0 \quad (49)$$

Its solution is

$$(p_2/p_1)_0=1 \quad (50a)$$

or

$$=[(k+1)^2W_1^2-(k-1)^2]/[(k^2-1)(1-W_1^2)] \quad (50b)$$

Ignoring the trivial solution, the nontrivial solution is the same as that derived for perfect gas.

While these expressions involving Z_i are solved and their solutions are substituted back into Eq. (48)

$$\frac{p_2}{p_1}=\frac{(k+1)^2W_1^2-(k-1)^2}{(k^2-1)(1-W_1^2)}\left(1+\sum_{i=1}^{8}z_i\Delta_i\right) \quad (51)$$

where

$$\Delta_1=2\frac{k-1}{k+1}\frac{(k-1)-(k+1)W_1^2}{(k+1)^2W_1^2-(k-1)^2}$$

$$\Delta_2=\frac{(k^2-1)(1-W_1^2)W_1^2}{(k+1)^2W_1^2-(k-1)^2}\left[-\frac{4}{(k+1)(1-W_1^2)}+\frac{2}{(k+1)W_1^2-(k-1)}\log\frac{(k+1)^2W_1^2-(k-1)^2}{(k+1)^2(1-W_1^2)W_1^2}\right]$$

$$\Delta_3=\frac{(k^2-1)(1-W_1^2)W_1^2}{(k+1)^2W_1^2-(k-1)^2}\left\{-\frac{4}{(k+1)(1-W_1^2)}+\frac{2[(k+1)W_1^2+(k-1)]}{(k+1)^2W_1^2-(k-1)^2}\right\}$$

$$\Delta_4=0$$

$$\Delta_5=\frac{(k-1)(1-W_1^2)}{(k-1)-(k+1)W_1^2}\left\{\left[1-\frac{k+1}{k-1}W_1^2+\frac{2W_1^2}{k(k-1)(1-W_1^2)}\right]\frac{(k+1)^2W_1^2-(k-1)^2}{(k^2-1)(1-W_1^2)}-\frac{2W_1^2}{k(k-1)(1-W)_1^2}\right\}$$

$$\Delta_6=\frac{(k^2-1)(1-W_1^2)2(4-3k)W_1^2}{(k+1)^2W_1^2-(k-1)_2}\left\{-\frac{2(3-2k)}{(k^2-1)(1-W_1^2)}+\frac{(k+1)(1-W_1^2)}{(k+1)^2W_1^2-(k-1)^2}\times\left[\left(\frac{k+1}{k-1}\right)^2W_1^4+\frac{k+1}{k-1}W_1^2+1\right]-4k\frac{(k+1)W_1^2+(k-1)}{(k+1)^2W_1^2-(k-1)^2}\right\}$$

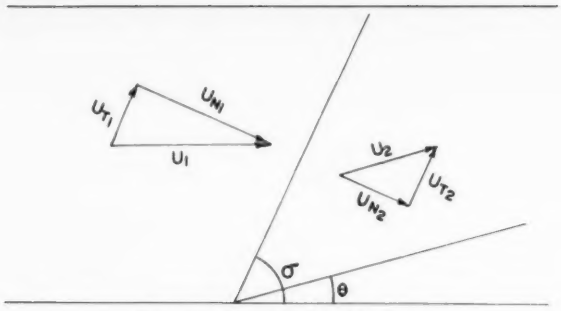

FIG. 1. Oblique shock diagram.

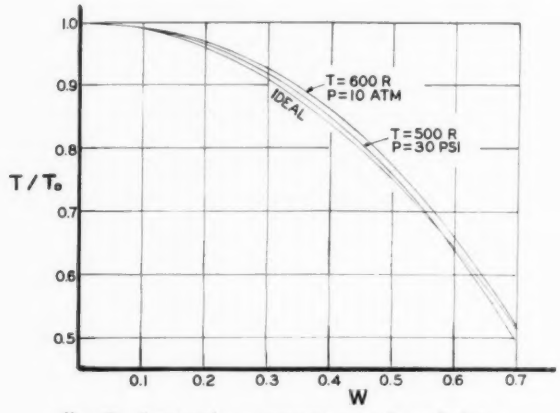

FIG. 2. Isentropic: temperature ratio variations.

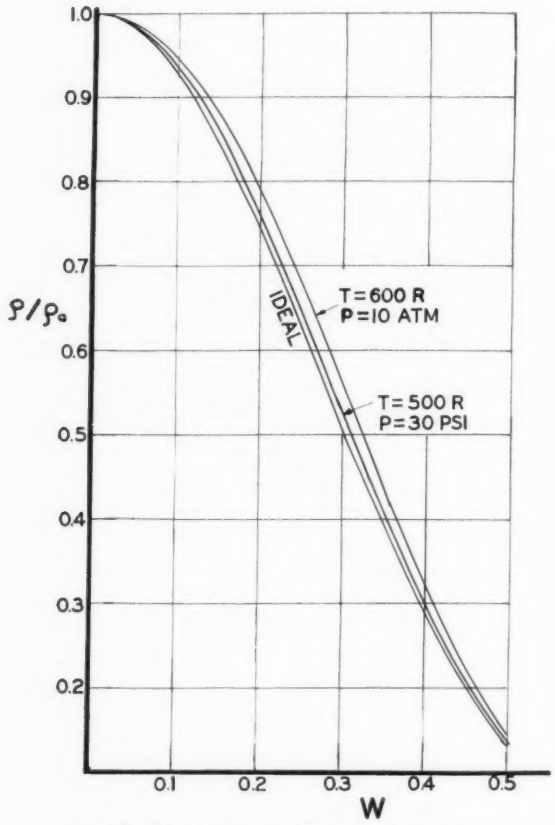

FIG. 3. Isentropic: density ratio variations.

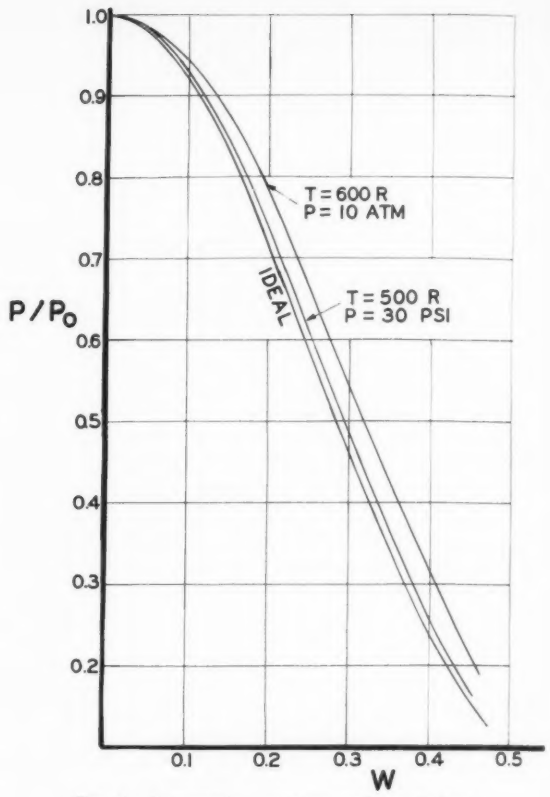

FIG. 4. Isentropic: pressure ratio variations.

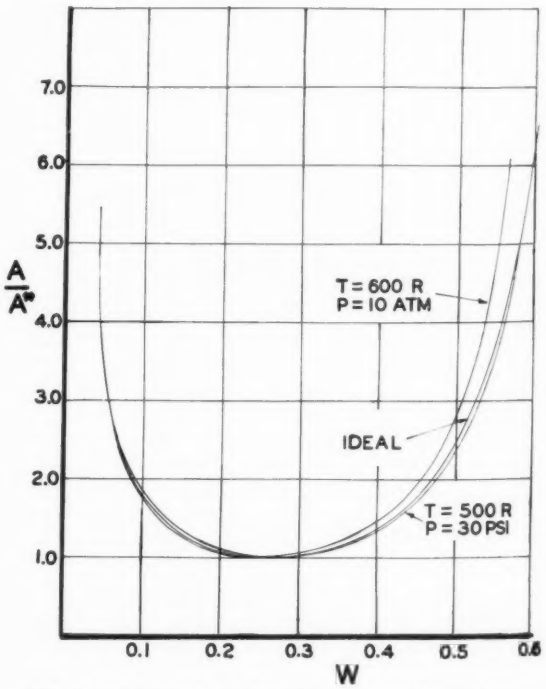

FIG. 5. Isentropic: cross-sectional area ratio variations.

$$\Delta_7 = \frac{(k^2-1)(1-W_1^2)}{(k+1)^2W_1^2-(k-1)^2}\left[\frac{4(k-2)W_1^2}{(k^2-1)(1-W_1^2)} - \frac{2(k-2)W_1^2}{k-1}\right]$$

$$\Delta_8 = \frac{(3-k)(k+1)(1-W_1^2)}{(k+1)^2W_1^2-(k-1)^2}\left[\frac{4W_1^2}{(k+1)(1-W_1^2)} - \frac{k+1}{k-1}W_1^4 - W_1^2\right]$$

This equation leads to the solution of the density ratio between upstream and downstream flow

$$\frac{\rho_2}{\rho_1} = \frac{k+1}{k-1}W_1^2\left(1+\sum_{i=1}^{8} z_i g_i\right) \tag{52}$$

where

$$g_1 = \{[(k+1)^2W_1^2-(k-1)^2]/[2k(k-1)]\}\Delta_1) + \{[(k+1)W_1^2-(k-1)]/k\}$$

$$g_2 = \{[(k+1)^2W_1^2-(k-1)^2]/[2k(k-1)]\}\Delta_2) + \{[(k+1)W_1^2-(k-1)]/k\}$$

$$g_3 = \{[(k+1)^2W_1^2-(k-1)^2]/[2k(k-1)]\}\Delta_3) + \{[(k+1)W_1^2-(k-1)]/k\}$$

$$g_4 = \{[(k+1)^2W_1^2-(k-1)^2]/[2k(k-1)]\}\Delta_4) - \{[(k+1)W_1^2-(k-1)]/(k-1)\}$$

$$g_5 = \frac{(k+1)^2W_1^2-(k-1)^2}{2k(k-1)}\Delta_5 + \frac{(k+1)[(k+1)W_1^2-(k-1)]}{k(k-1)}$$

$$g_6 = \frac{(k+1)^2W_1^2-(k-1)^2}{2k(k-1)}\Delta_6 + \frac{(3-2k)(4-3k)}{k}\left[\frac{(k+1)W_1^2-(k-1)}{k-1}\right]$$

$$g_7 = \frac{(k+1)^2W_1^2-(k-1)^2}{2k(k-1)}\Delta_7 + \frac{2-k}{k}\left[\frac{(k+1)W_1^2-(k-1)}{k-1}\right]$$

$$g_8 = \frac{(k+1)^2W_1^2-(k-1)^2}{2k(k-1)}\Delta_8 + \frac{3-k}{k}\left[\frac{(k+1)W_1^2-(k-1)}{k-1}\right]$$

With the pressure and density ratio equations the temperature ratio is then found with the help of the equation of state. It is

$$\frac{T_2}{T_1} = \frac{1}{1-W_1^2}\left[1-\left(\frac{k-1}{k+1}\right)^2\frac{1}{W_1^2}\right]\times\left(1+\sum_{i=1}^{8} z_i h_i\right) \tag{53}$$

where

$$h_1 = \Delta_1 - g_1$$

$$h_2 = \Delta_2 - g_2$$

$$h_3 = \Delta_3 - g_3$$

$$h_4 = \Delta_4 - g_4 + 1 - [(k+1)/(k-1)]W_1^2$$

$$h_5 = \Delta_5 - g_5 - 1 + \{[(k+1)/(k-1)]W_1^2\}^2$$

$$h_6 = \Delta_6 - g_6 - 1 + \left(\frac{k+1}{k-1}W_1^2\right)^4\left[\frac{(k^2-1)(1-W_1^2)}{(k+1)^2W_1^2-(k-1)^2}\right]^3$$

$$h_7 = \Delta_7 - g_7 - 1 + \left(\frac{k+1}{k-1}W_1^2\right)^2\left[\frac{(k^2-1)(1-W_1^2)}{(k+1)^2W_1^2-(k-1)^2}\right]$$

$$h_8 = \Delta_8 - g_8 + 1 - \left(\frac{k+1}{k-1}W_1^2\right)^3\left[\frac{(k^2-1)(1-W_1^2)}{(k+1)^2W_1^2-(k-1)^2}\right]$$

The downstream Crocco Number may be evaluated directly from the continuity equation,

$$W_2 = W_1(\rho_1/\rho_2) \tag{54}$$

or

$$W_2 = \frac{k-1}{k+1}\frac{1}{W_1}\left(1+\sum_{i=1}^{8} z_i\omega_i\right) \tag{55}$$

where

$$\omega_i = -g_i$$

(C) *The Oblique Shock*

In addition to the one-dimensional shock the oblique shock is analyzed here. Generally in such problems the velocity is resolved into two components—i.e., the normal and tangential components with respect to the shock wave. Based on the previously stated concepts, the tangential velocity components do not change before and after the shock, and the normal velocity components behave as in normal shock.

Before we analyze any further the oblique shock, the Crocco Number in such flow should be discussed. Due to the addition of a velocity parallel to the shock wave front from the view of normal shock, the maximum

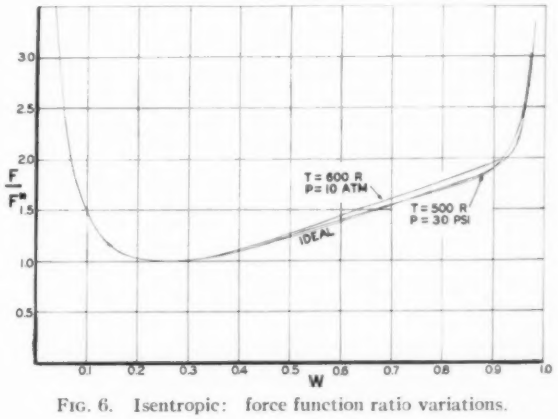

FIG. 6. Isentropic: force function ratio variations.

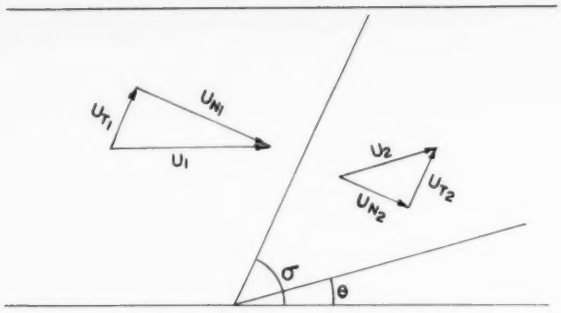

FIG. 1. Oblique shock diagram.

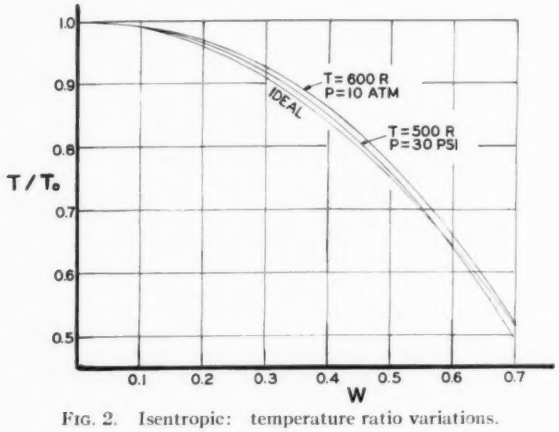

FIG. 2. Isentropic: temperature ratio variations.

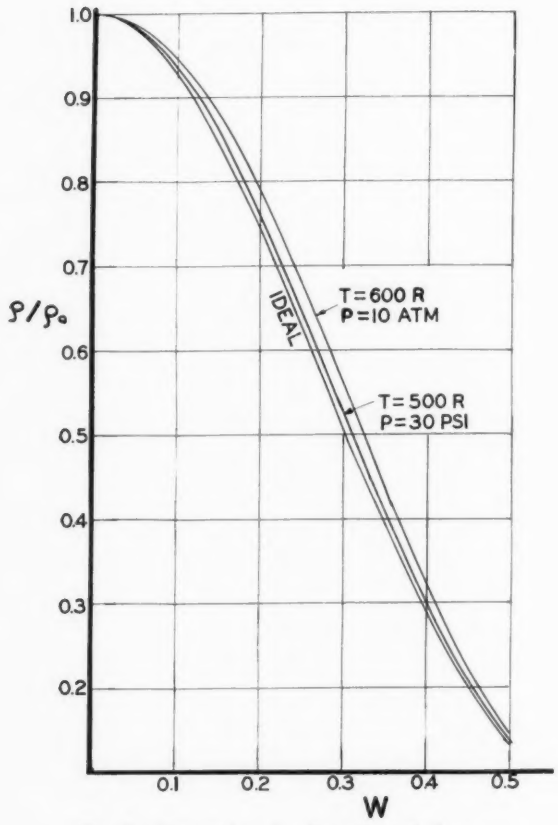

FIG. 3. Isentropic: density ratio variations.

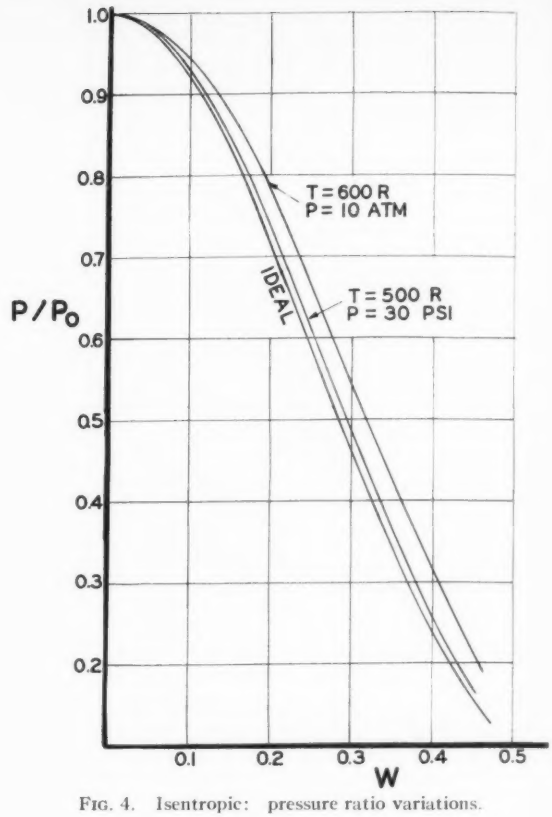

FIG. 4. Isentropic: pressure ratio variations.

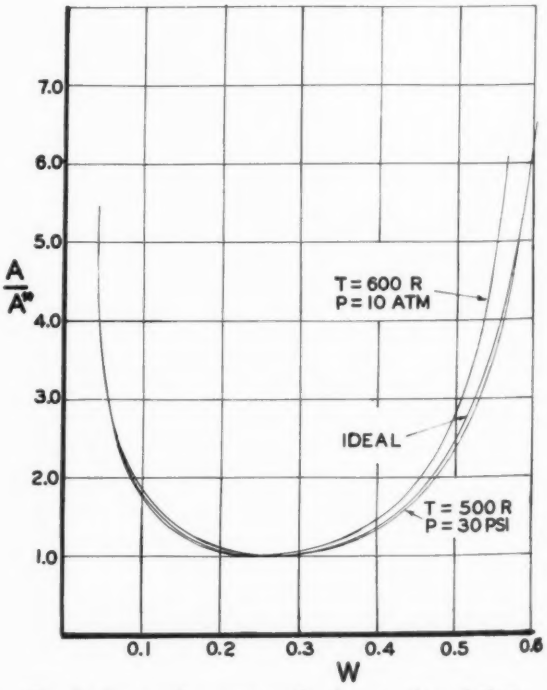

FIG. 5. Isentropic: cross-sectional area ratio variations.

$$\Delta_7 = \frac{(k^2-1)(1-W_1^2)}{(k+1)^2W_1^2-(k-1)^2}\left[\frac{4(k-2)W_1^2}{(k^2-1)(1-W_1^2)} - \frac{2(k-2)W_1^2}{k-1}\right]$$

$$\Delta_8 = \frac{(3-k)(k+1)(1-W_1^2)}{(k+1)^2W_1^2-(k-1)^2}\left[\frac{4W_1^2}{(k+1)(1-W_1^2)} - \frac{k+1}{k-1}W_1^4 - W_1^2\right]$$

This equation leads to the solution of the density ratio between upstream and downstream flow

$$\frac{\rho_2}{\rho_1} = \frac{k+1}{k-1}W_1^2\left(1+\sum_{i=1}^{8} z_i g_i\right) \qquad (52)$$

where

$$g_1 = \{[(k+1)^2W_1^2-(k-1)^2]/[2k(k-1)]\}\Delta_1) + \{[(k+1)W_1^2-(k-1)]/k\}$$

$$g_2 = \{[(k+1)^2W_1^2-(k-1)^2]/[2k(k-1)]\}\Delta_2) + \{[(k+1)W_1^2-(k-1)]/k\}$$

$$g_3 = \{[(k+1)^2W_1^2-(k-1)^2]/[2k(k-1)]\}\Delta_3) + \{[(k+1)W_1^2-(k-1)]/k\}$$

$$g_4 = \{[(k+1)^2W_1^2-(k-1)^2]/[2k(k-1)]\}\Delta_4) - \{[(k+1)W_1^2-(k-1)]/(k-1)\}$$

$$g_5 = \frac{(k+1)^2W_1^2-(k-1)^2}{2k(k-1)}\Delta_5 + \frac{(k+1)[(k+1)W_1^2-(k-1)]}{k(k-1)}$$

$$g_6 = \frac{(k+1)^2W_1^2-(k-1)^2}{2k(k-1)}\Delta_6 + \frac{(3-2k)(4-3k)}{k}\left[\frac{(k+1)W_1^2-(k-1)}{k-1}\right]$$

$$g_7 = \frac{(k+1)^2W_1^2-(k-1)^2}{2k(k-1)}\Delta_7 + \frac{2-k}{k}\left[\frac{(k+1)W_1^2-(k-1)}{k-1}\right]$$

$$g_8 = \frac{(k+1)^2W_1^2-(k-1)^2}{2k(k-1)}\Delta_8 + \frac{3-k}{k}\left[\frac{(k+1)W_1^2-(k-1)}{k-1}\right]$$

With the pressure and density ratio equations the temperature ratio is then found with the help of the equation of state. It is

$$\frac{T_2}{T_1} = \frac{1}{1-W_1^2}\left[1-\left(\frac{k-1}{k+1}\right)^2\frac{1}{W_1^2}\right]\times\left(1+\sum_{i=1}^{8} z_i h_i\right) \qquad (53)$$

where

$$h_1 = \Delta_1 - g_1$$

$$h_2 = \Delta_2 - g_2$$

$$h_3 = \Delta_3 - g_3$$

$$h_4 = \Delta_4 - g_4 + 1 - [(k+1)/(k-1)]W_1^2$$

$$h_5 = \Delta_5 - g_5 - 1 + \{[(k+1)/(k-1)]W_1^2\}^2$$

$$h_6 = \Delta_6 - g_6 - 1 + \left(\frac{k+1}{k-1}W_1^2\right)^4\left[\frac{(k^2-1)(1-W_1^2)}{(k+1)^2W_1^2-(k-1)^2}\right]^3$$

$$h_7 = \Delta_7 - g_7 - 1 + \left(\frac{k+1}{k-1}W_1^2\right)^2\left[\frac{(k^2-1)(1-W_1^2)}{(k+1)^2W_1^2-(k-1)^2}\right]$$

$$h_8 = \Delta_8 - g_8 + 1 - \left(\frac{k+1}{k-1}W_1^2\right)^3\left[\frac{(k^2-1)(1-W_1^2)}{(k+1)^2W_1^2-(k-1)^2}\right]$$

The downstream Crocco Number may be evaluated directly from the continuity equation,

$$W_2 = W_1(\rho_1/\rho_2) \qquad (54)$$

or

$$W_2 = \frac{k-1}{k+1}\frac{1}{W_1}\left(1+\sum_{i=1}^{8} z_i\omega_i\right) \qquad (55)$$

where

$$\omega_i = -g_i$$

(C) *The Oblique Shock*

In addition to the one-dimensional shock the oblique shock is analyzed here. Generally in such problems the velocity is resolved into two components—i.e., the normal and tangential components with respect to the shock wave. Based on the previously stated concepts, the tangential velocity components do not change before and after the shock, and the normal velocity components behave as in normal shock.

Before we analyze any further the oblique shock, the Crocco Number in such flow should be discussed. Due to the addition of a velocity parallel to the shock wave front from the view of normal shock, the maximum

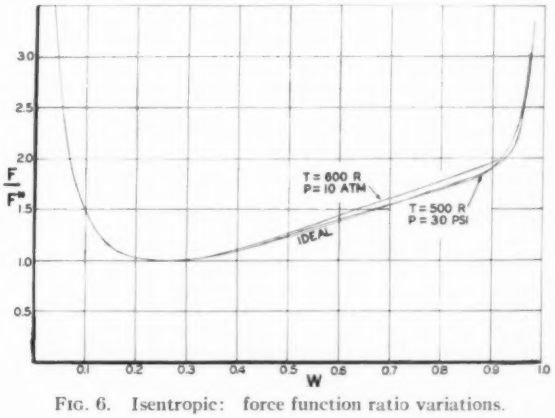

FIG. 6. Isentropic: force function ratio variations.

velocity attainable of the normal component is not equal to

$$u_m \quad \text{or} \quad \{u^2 + [2/(k-1)]u_s^2\}^{1/2}$$

but

$$\{u_n^2 + [2/(k-1)]u_s^2\}^{1/2}$$

or

$$(u_m^2 - u_2^2)^{1/2}$$

Hence it is

$$W_n = u_n/(u_m^2 - u_t^2)^{1/2} \tag{56a}$$

$$W_t = u_t/(u_m^2 - u_n^2)^{1/2} \tag{56b}$$

and

$$W = u/u_m \tag{57}$$

And the relations of their Crocco Number are derived as

$$W^2 = \{[W_n^2(1 - W_t^2)]/(1 - W_n^2W_t^2)\} + \{[W_t^2(1 - W_n^2)]/(1 - W_n^2W_t^2)\} \tag{58}$$

$$W_n^2 = W^2[\sin^2\sigma/(1 - W^2\cos^2\sigma)] \tag{59a}$$

$$W_t^2 = W^2[\cos^2\sigma/(1 - W^2\sin^2\sigma)] \tag{59b}$$

From Fig. 1 we can see that

$$\tan(\sigma - \theta) = u_{n_2}/u_{t_2} = (W_{n_2}/W_{t_2})\,[(1 - W_{t_2}^2)/(1 - W_{n_2}^2)]^{1/2} \tag{60}$$

As stated

$$u_{t_2} = u_{t_1}$$

it is

$$W_{t_2} = W_{t_1}(u_{mt_1}/u_{mt_2}) \tag{61}$$

and with

$$u_{m_2}^2 = [2/(k-1)]u_s^2 + u_{n_2}^2 + u_{t_2}^2 \tag{62}$$

Eq. (61) becomes

$$W_{t_2} = W_{t_1}(u_{s_1}/u_{s_2})\,[(1 - W_{t_2}^2)/(1 - W_{t_1}^2)]^{1/2} \tag{63}$$

Therefore by substituting W_{t_2} into Eq. (60) we get

$$\tan(\sigma - \theta) = W_{n_2}/W_{t_1}[(1 - W_{t_1}^2)/(1 - W_{n_2}^2)]^{1/2} \tag{64}$$

Then by Eq. (55) of normal shock, W_{n_2} is substituted in terms of W_{n_1}, we get

$$\tan(\sigma - \theta) = \tan(\sigma - \theta)_c\left(1 + \sum_{i=1}^{8} z_i\phi_i\right) \tag{65}$$

where

$$\tan(\sigma - \theta)_c = [(k-1)/(k+1)] \times [1/(W_{n_1}W_{t_1})]\,[(1 - W_{t_1}^2)/(1 - W_{n_1}^2)]^{1/2} \tag{66}$$

and

$$\phi_1 = \Delta_1$$

$$\phi_2 = \Delta_2 + \frac{k-1}{k}\left[1 - \frac{(1 - W_{n_1}^2)\,(k+1)^2W_{n_1}^2}{(k+1)^2W_{n_1}^2 - (k-1)^2}\right]$$

$$\phi_3 = \Delta_3 + \frac{k-1}{k}\left\{1 - \left[\frac{(1 - W_{n_1}^2)\,(k+1)^2W_{n_1}^2}{(k+1)^2W_{n_1}^2 - (k-1)^2}\right]^2\right\}$$

$$\phi_4 = -g_4$$

$$\phi_5 = \Delta_5 + \frac{k+1}{k}\left[1 - \left(\frac{k+1}{k-1}\right)^2 W_{n_1}^2\right]$$

$$\phi_6 = \Delta_6 + \frac{(3-2k)\,(4-3k)}{k} \times \left\{1 - \frac{k+1}{k-1}W_{n_1}^2\,\frac{(1 - W_{n_1}^2)\,(k+1)^6W_{n_1}^6}{[(k+1)^2W_{n_1}^2 - (k-1)^2]^3}\right\}$$

$$\phi_7 = -g_7$$

$$\phi_8 = \Delta_8 - \left(\frac{3}{k} - 1\right)\left[1 - \left(\frac{k+1}{k-1}\right)^2 \times \frac{(1 - W_{n_1}^2)\,(k+1)^2W_{n_1}^2}{(k+1)^2W_{n_1}^2 - (k-1)^2}\right]$$

$\tan(\sigma - \theta)_c$ is defined for perfect gas and can be easily obtained from gas tables or a shock polar diagram.

With the initial state and geometrical configuration, the true upstream Crocco Number may be found by this equation. Then the normal component of this number is calculated; so all the properties and characteristics of the oblique shock may be determined by the use of the normal shock equations in the preceding section.

(IV) Discussion and Conclusion

As for numerical calculations of real gas behavior, it is necessary to specify the initial condition because correction factors of real gases are dependent upon the initial conditions. The formulas derived in the previous section have been applied to Freon-12 with the constants in the Beattie-Bridgeman equation, Eq. (1), determined by Buffington-Gilkey,[12] as follows.

$$A_0 = 6.12$$
$$B_0 = 0.078$$
$$a = 0.0404$$
$$b = 0.0824$$
$$c = 0$$

Values of P are in lbs. per sq.in.; values of ρ are in lbs. per cu.ft.; and values of T in °R. The constants in the specific heat equation, Eq. (9), determined from Raman spectroscopic measurements by Bradley[13] and infra-red spectroscopic measurements recently by Plyler-Benedict[14] are as follows.

$$a_1 = 26.768$$
$$a_2 = -8.3862 \times 10^3$$
$$a_3 = 5.5825 \times 10^5$$

A series of calculations have been performed and tabulated with the Crocco Number as the independent variable.[15]

In order to compare the ideal and real gas behaviors, the following assumptions are made: The fictitious ideal gas has $k = 1.14$ and $C_v = 14.21$ B.t.u. per lb.-

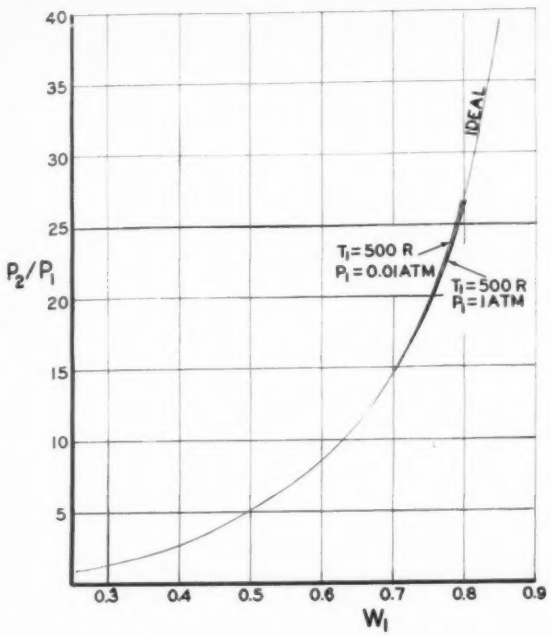

FIG. 7. Normal shock: pressure ratio variations.

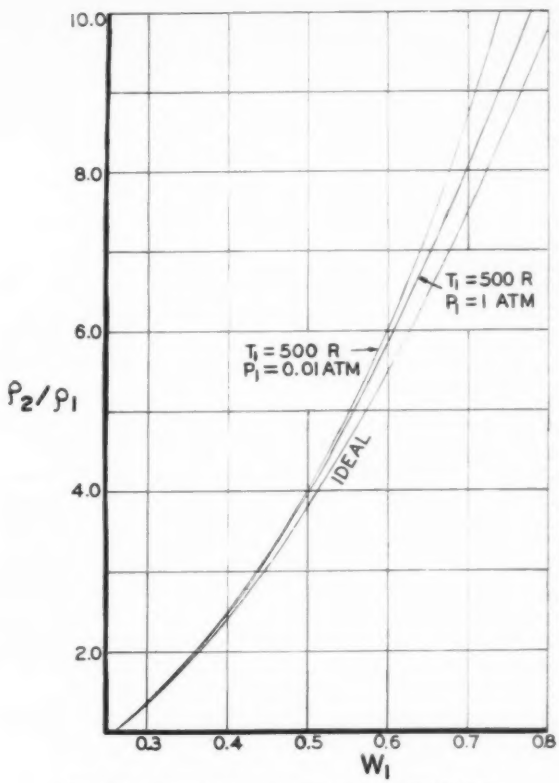

FIG. 8. Normal shock: density ratio variations.

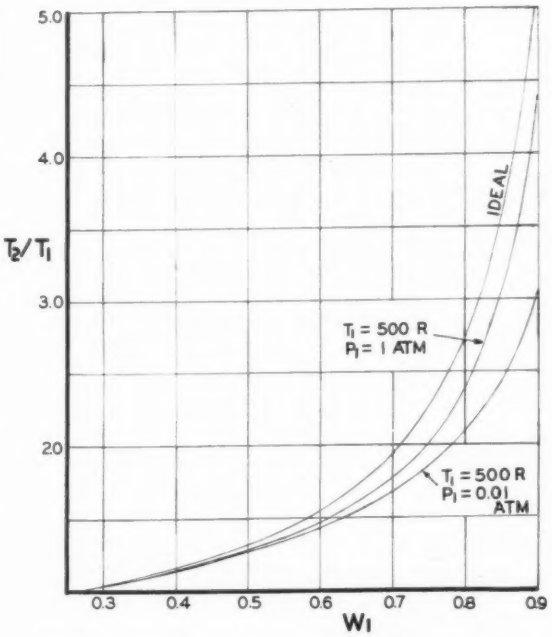

FIG. 9. Normal shock: temperature ratio variations.

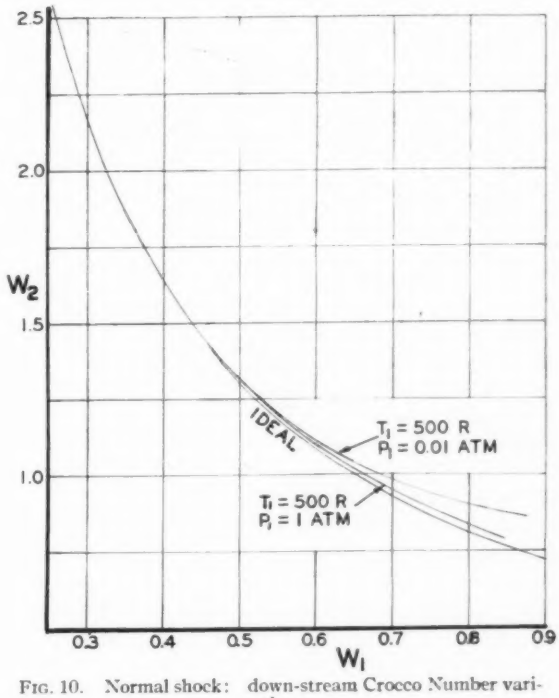

FIG. 10. Normal shock: down-stream Crocco Number variations.

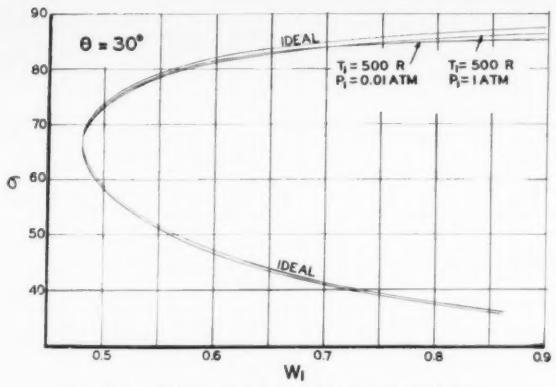

FIG. 11. Oblique shock: Mach angle variations.

mole-F, which are the numerical values at room conditions, while for the real gas the following initial conditions are chosen.

(1) For isentropic flow the reference state was specified to be the stagnation state, and the initial states were selected as (a) p = 30 lbs. per sq.in. and T = 500°R., (b) p = 10 atmospheres and T = 600°R., where the reference state of case (a) for the fictitious ideal gas applies with reasonable accuracy also for case (b).

(2) In the calculations for shock relations, the state in front of the stationary shock was selected as the reference state and the initial states were chosen as (a) p = 1 atmosphere and T = 500°R. (b) p = 1/100 atmosphere and T = 500°R.

In the oblique shock problems, a wedge angle θ = 30° was selected as an additional reference condition to the above listed initial states in both cases. In these examples the initial states of lower pressure refer to the case that the real gas approaches the behavior of a semiperfect gas with only the caloric imperfectness being of appreciable influence, while the other ones are leading to results influenced by both imperfectnesses. All these calculations are presented in graphical forms, Figs. 2–11.

In isentropic flow the pressure change deviates more from the ideal case than either the density or temperature change at the same state or Crocco Number, while in the shock problems, on the contrary, the pressure has less deviation. Also it is observed that the influences due to two imperfectnesses are generally of opposite direction so that they compensate each other partly. No numerical percentage of deviations are given, since these values will be different for different assigned k and C_v values of the ideal case.

In this investigation additional phenomena should be discussed: First there is the heat capacity lag or the relaxation time required for the specific heat to change with a change of temperature. This time lag is mainly due to the fact that vibrational energy requires more collisions per molecule to attain a new temperature than the translational and rotational energies, and hence it reaches the equilibrium state after a longer interval. Kantrowitz[16] found that if such time intervals are comparable with or shorter than the time required for the gas to absorb its full heat capacity due to the change of temperature, the gas will not have reached its equilibrium state of energy. In this case the transfer of energy from parts of the heat capacity which have more than their share to parts that have less than their share will be an irreversible process and will increase the entropy of the gas and consequently will decrease the total head of the gas. However, this may be made insignificant by lowering the rate of change of the temperature. As in the shock problems, Bethe and Teller[17] observed that the heat capacity lag will increase the thickness of the shock. This simply means a broadening of the region of transition. As long as both the downstream and upstream positions are at a distance from the shock, this consideration may be ignored without great bearing on the accuracy.

Another possible effect that should be discussed is the chemical dissociation of the gas at high temperature. Such dissociation will lead to changes in the energy level of the gas; it will falsify the basic assumption of the energy equation. But this can be avoided by suitable adjustment not allowing the gas to exceed its dissociation temperature.

From the foregoing investigations the following conclusions may be drawn. Gas dynamic problems can be treated in a most general way by the use of the Beattie-Bridgeman equation of state and a specific heat depending upon temperature and pressure based on the spectroscopic measurements. The results in the form of gas dynamic relations between the properties of the gas and geometrical quantities determining the flow configurations may be presented in terms of specified constants with the Crocco Number as independent variable.

ACKNOWLEDGMENT

The paper is abstracted from the author's thesis written under the supervision of Dr. H. H. Korst and Professor W. N. Espy, Professors of Mechanical Engineering, University of Illinois. The author is heartily grateful for their valuable guidance.

REFERENCES

[1] Tsien, H. S., *One-Dimensional Flows of a Gas Characterized by van der Waal's Equation of State*, Jour. of Math. and Phy., Vol. 25, No. 6, pp. 301–324, 1947.

[2] Eggers, A. J., *One-Dimensional Flow of Imperfect Diatomic Gas*, NACA TN No. 1861, 1949.

[3] Durham, F. P., *Supersonic Flow with Variable Specific Heat*, Jour. of Appl. Mech. ASME Trans., Vol. 74, pp. 57–62, 1952.

[4] Korst, H. H., *Discussion on Durham's "Supersonic Flow with Variable Specific Heat,"* Jour. of Appl. Mech. ASME Trans., Vol. 74, p. 405, 1952.

[5] Walker, W. J., *The Effect of Variable Specific Heats on the Discharge of Gases Through Orifices or Nozzles*, Phil. Mag., Vol. 143, pp. 589–592, 1922.

[6] Traupel, W., *Zur Dynamik realer Gase*, Forsch. auf dem Geb. des Ing. Wes., Vol. 18, No. 1, pp. 3–9, 1952.

[7] Beattie, J. A., and Bridgeman, O. C., *A New Equation of State for Fluids*, Proc. of Amer. Acad. Arts and Sci., Vol. 63, No. 5, pp. 229–308, 1928.

(*Continued on page 794*)

Acoustics in Relation to Aerodynamics*

E. G. RICHARDSON†

University of Durham
King's College, Newcastle-upon-Tyne, England

AT THE BEGINNING of the century, it was customary to regard sound and fluid dynamics almost as two aspects of the same subject. The great names in this subject such as Rayleigh and Lamb were equally conversant with both. With the rise of technical acoustics and aeronautics as separate subjects in which the exponents of one group had little interest in the doings of the other, a dichotomy has taken place. The cleavage has been increased by the fact that the modern worker in acoustics requires an expert knowledge of electronics, whereas the instrumentation of aerodynamics has remained on the whole nonelectrical. Recent events, particularly the approach of aircraft speeds to that of sound and the increased speeds of ships, have, however, brought a new rapprochement between the two subjects.

Turbulence as an Acoustic Phenomenon

It is with Rayleigh that the story starts, in the era of Osborne Reynolds when scientists were trying to find the conditions under which a laminar "boundary layer" (to use the modern term) in the flow over the walls of a pipe would become unstable and so lead to turbulence. Rayleigh's idea was to take a steady gradient of velocity at the wall and impose on it a simple harmonic disturbance of finite amplitude to see whether the gradient in progressing remained stable. His mathematics showed that certain gradients were always unstable, some neutral. Later Prandtl, von Kármán, and Noether severally sought solutions of the boundary-layer equations for given boundary conditions in which they overlaid the steady stream with periodic fluctuations whose amplitude and wavelength depended on distance from the wall.

The experimental method which this line of thought suggests is to impose on a steady stream a simple harmonic modulation of small amplitude and moderate frequency and to examine the transformation of the flow by this superposed fluctuation to see how closely it approximates in properties to a naturally turbulent stream, particularly in respect to (1) rise and decay of the fluctuations, and (2) development of characteristic distribution of velocity across the stream. The devices which have been employed to produce the desired simple harmonic motion in the course of the fluid comprise (1) tangential oscillation of part of a smooth wall over which the fluid passes, (2) passage of the fluid over a rigid corrugated solid boundary, and (3) passage over a flexible boundary. The latter may take the form of a pennant or the fluid may be forced out of a linear orifice to impinge on a wedge so that the jet is set in sinusoidal oscillation between fluid boundaries as in the familiar method of producing edge tones (see below).

Most illuminating from the point of view of the architecture of turbulence are the experiments of the first type (Richardson and Tyler[1]) in which a pipe has a loose section interposed between the entrance cone and the main portion of the pipe which is connected at its other end to an aspirator. The loose section is mounted on the end of a long connecting rod to a crank with adjustable throw on the axle of an electric motor. Air is first aspirated through the pipe at a speed just below the critical value and the gradient of velocity explored at various sections of the pipe downstream from the mobile portion. This is next set in operation and the velocity traverses redetermined. Whereas the former profile was parabolic, it has now gone over into the steeper logarithmic type characteristic of turbulent flow, which can in fact be reproduced in the untouched flow in the pipe by making the entry more abrupt, or copied at a larger scale by increasing the speed of aspiration above the critical. Finally the distribution of velocity amplitude with the piston alone in operation—i.e., no through draught—is obtained. The latter distribution can be deduced theoretically on the assumption of laminar flow. For a displacement wave of periodic form $a \sin \omega t$ having pulsatance ω the velocity amplitude $a\omega$ reaches a maximum at a distance δ from the wall of the pipe, such that

$$\sqrt{\omega}\,\delta/\nu = 2.28$$

ν being the kinematic viscosity of the fluid (see Fig. 1, curves at left).

The disturbances of all frequencies are not equally amplified and some may be damped, though this depends also on the Reynolds Number of the flow. A re-examination of the earlier results showed a variation of amplification coefficient with frequency exhibited in Fig. 2, the broken line giving the theoretical variation (with square root of frequency). Such variations have also been shown in recent measurements by Schubauer and Skramstad and others[2, 2a, 2b] who also built loud-speaker diaphragms into the wall of a low turbulence wind tunnel with similar intention.

It may be objected that this artificial turbulence does not correspond with nature in that the pulsatance ω is

Received September 9, 1954.

* This paper was presented at the Langley Aeronautical Laboratory, NACA, Langley Field, Va., July 2, 1954.

† Reader in Physics.

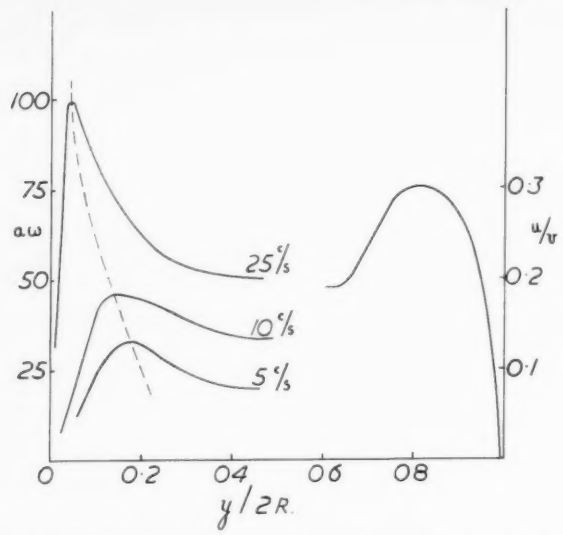

FIG. 1. Amplitude of velocity fluctuation in pipe of radius R; y, distance from wall. *Left*, in sound waves; *right*, in turbulent flow, u root mean square axial fluctuations, U mean stream velocity.

not monochromatic in real turbulence but is more like a band spectrum embracing a range of frequencies requiring a Fourier series in the solution. To the extent that such partial vibrations may in practice have different damping coefficients so that the spectrum changes *en marchant*, our idealized picture of turbulent flow requires modification; but it is certainly a fact that natural turbulence shows velocity profiles and distributions of intensity of fluctuation precisely similar to those in our developed flow. Thus Fage and Townend[3] in their ultra-microscopic investigation of turbulent flow in pipes have found peaks in the fluctuations near the walls like those shown, for the sake of comparison, on the right of Fig. 1.

Although it seems then well established that turbulence in wind tunnels has its origin in a quasi-periodic disturbance, there seems to be no practical relationship between the frequency of the naturally induced oscillation and any other parameter of the flow, such as the Reynolds Number of the flow or the roughness of the walls. Any simplified periodicity that remains after a sufficiently long passage is to be ascribed to the greater damping of the high frequencies, which are, however, constantly replenished by new disturbances engendered at the walls.

More is known about the onset of oscillation in the wake of an obstacle, such as a cylinder in a steady stream. Even at very low Reynolds Numbers a slight divagation of the wake is sufficient to set the wake pendulating just as though it were a free jet of liquid from a nozzle, set in motion by a slight vibration communicated to the nozzle. At a somewhat higher Reynolds Number, the stationary vortices which are set up behind the obstacle take part in the oscillation of the wake and give rise to the familiar procession of vortices down the wake, which, especially if the obstacle is capable of sympathetic vibration, lead to the aeolian tones well known in acoustics.

This motion is maintained by the disturbing action of the detachment of vortices from one half of the boundary layer on the pressure gradient along the other half. There are, as Holtzmark *et al*[4] have recently remarked, deviations from ideal flow in the boundary layer, leading to peaks of velocity near to the cylinder wall corresponding to those already remarked in pipe flow.

All these oscillations, if of sufficient frequency and amplitude, give rise to sound. Which leads one to the question: Is there indeed any difference between such velocity fluctuations and more conventional sound sources? One necessity obviously is that the velocity changes should induce local pressure changes, to be then propagated with the speed of sound through the fluid. An instance of velocity waves not giving rise to sound waves is to be found in the propagation of shear vibrations. If a disc is oscillating about its axis in a viscous fluid it does not compress the fluid which bathes it and so it produces no sound.

CORRELATIONS IN VELOCITY AND SOUND FIELDS

In a turbulent fluid flow there exists a correlation in the statistical sense between the *motions* at two points in a field, but there is no fixed relationship (in time) such as one expects in the field of a sound source.

One could say that correlations in a field of flow are vectorial whereas those in a sound field are rather of scalar type.

An attempt to find a correlation between pressure fluctuations in a wind tunnel, picked up on a hot-wire microphone with streamlined nose, and the noise of the fan, picked up on a moving coil microphone, has been made by Schuh and Winter[5] at the Royal Aeronautical Establishment at Farnborough. They analyzed the frequency spectrum of both types of disturbance, but were unable to establish a sure correlation between them. Nevertheless, it is recognized in aeronautical research establishments that in building a wind tunnel of low turbulence, noise is a factor which must be considered. When all other disturbing factors are eliminated, it is now possible to reduce the intensity of turbulence

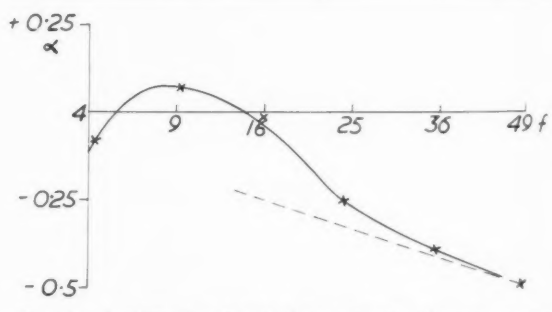

FIG. 2. Amplification ($+\alpha$) of periodic disturbances, propagated along a pipe, 5-in. diameter at mean speed 3 ft. per sec., in relation to frequency. Full line, experimental; broken line, theoretical.

(expressed as a ratio of the fluctuation to the mean wind) to 1/3 per cent, which probably represents the fluctuation associated with the sound output of the propeller and other unavoidable sources.

Acoustics of Jets

Interest in jet noise has revived interest in another old problem, that of the "edge tone." An unassisted jet produces an impure sound but may by some form of resonance or interference be persuaded to produce a series of pure tones. One way of doing this is to communicate harmonic vibration to the nozzle from which the jet issues (Fig. 3a). Another way is to let an air or water jet impinge on a sharp wedge. If the distance from slit to edge is kept constant and air at low pressure admitted to the wind chest behind the slit, the pitch of the edge tone rises with efflux velocity (with some jumps of frequency at certain pressures), while if the wind pressure is kept constant and the wedge moved away from the slit, an opposite effect on the pitch occurs. After the alternate vortex street behind an obstacle in a stream had been observed and studied, a similar vortex system was invoked to explain what could be seen in an edge-tone jet, although it was recognized that the eddies do not emerge full-grown from the slit but gather strength as they are carried toward the edge (see Fig. 3b).

About twenty years ago, two rival theories of the edge tone were current. One regarded the phenomenon as purely acoustic—each time a vortex hit the edge a sound wave signalled back to the edge to start another one. The author thought that he had disposed of this theory by opening another jet alongside the principal one and showing that the postulated sound wave is unable to set this subsidiary jet into pendulation; but recently Powell[6] and Nyborg[7] have revived this acoustic hypothesis. The second theory was a hydrodynamic one, based on the writer's[8] observation that a secondary vortex system is set up in the boundary layer alongside the wedge, and that these have to fall into line with the main system to form two vortex streets, one each side of the wedge. Curle[9] has recently taken up and extended this theory, showing that the hydrodynamic reaction on the fluid debouching from the slit results from the alternating transverse velocity at the tip without the intervention of any sound signal. At low velocities, when the edge tone results from a simple periodic pendulation, it ought surely to be possible to give a purely hydrodynamic explanation to the phenomenon. It may be noted, indeed, that pendulations similar to those of edge tones may be produced when underwater jets strike an opposing wedge at speeds far too low to engender sound waves in the water.[7]

Reverting to the unassisted jet (from a circular orifice), one may assume that the origin of the hissing noise which accompanies the efflux of air at moderate speeds is to be found in shearing forces, both within the nozzle and outside where a "surface of discontinuity"—as Helmholtz called it—exists between the fast moving

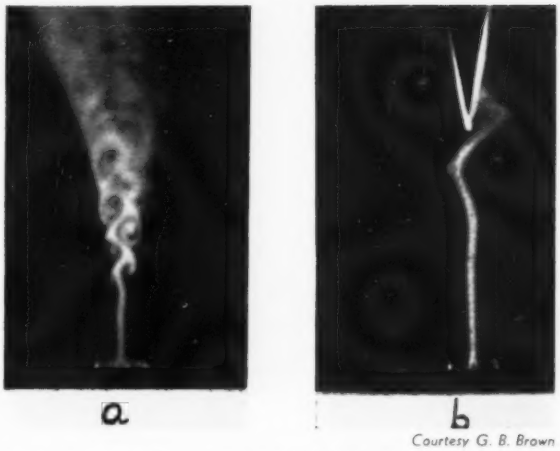

Courtesy G. B. Brown

Fig. 3. Jets in air made visible by admixture of smoke; (a) periodic disturbance communicated to nozzle, (b) jet impinging on a wedge.

and the more or less stationary air. Here boundary layers engendering turbulence are to be found, at first apparent as small eddies or high-frequency fluctuations; but farther down the jet these roll up into larger ones, involving fluctuations of lower frequency. Examination of the spectrum of open-air turbulence with hot wires and of the associated sound spectrum with microphones show them to be closely parallel. At any rate, confirmation of the statement about the relative size of the jet eddies can be found when one traces back the sound picked up from the microphone to its origins, the high-frequency sources then being revealed as located near the nozzle, while the low-frequency sources are to be found farther downstream and carried with the jet.

When the speed of efflux from the nozzle exceeds that of sound in the gas, a change in the disposition of the jet ensues. Schlieren photographs show that the jet alternately expands and contracts, while it is crisscrossed with a system of shock waves originating at the nozzle and reflected at the confines of the jet. The phenomenon is now acoustic rather than hydrodynamic in mechanism. One can, for example, let the supersonic jet—from a circular nozzle—impinge on a coaxial metal ring to produce edge tones of a definite frequency, but only if one places the round edge near one of the zones of instability at which the shock waves are reflected. Presumably in this case there is resonance of the waves reflected from the ring with those set up at the nozzle, as suggested by Wachsmuth for the low-speed edge tones. The jet-edge system just described is, in fact, the basis of the Hartmann generator in which, by constructing the apparatus on a miniature scale (nozzle about 0.5 mm. in diameter, jet-edge separation about 1 mm.) this investigator was able to construct a source of ultrasonic frequency.

A jet of supersonic velocity is, in fact an efficient transducer of kinetic into acoustic power, some of it audible, some ultrasonic. It has been suggested by Richards and others[10, 10a, 10b] that the origin of this

excess noise (above that of a merely turbulent jet) arises from the interaction of the shock waves with the turbulent boundary layer or "surface of discontinuity." On this idea the zones of instability aforesaid will become potent sources of sound. The sound field around the jet will then be rather like that of light in front of an optical grating—that is to say, there will be directions in which the energy from different sources will constructively and destructively interfere—and there is some experimental evidence, from polar curves of supersonic jets, which supports this.

These conclusions are fairly well supported by experiments on model jets. Such "smoothing" of the polar curves for intensity in comparison with theory as is observed can probably be ascribed to the scattering of the sound as it passes through the turbulent field.

Thermo-Acoustic Phenomena

Another phenomenon of respectable antiquity which has been resuscitated in this gas-turbine age is the "singing flame." Actually, this was the first problem given to the author when in 1922 he went to the late Prof. C. H. Lees of London and said that he wanted to start research in acoustics. Indeed, the writer believed that, as a result of his efforts, the matter had been decently buried, but two symposia held at the Massachusetts Institute of Technology in 1952 and 1954 have dealt *inter alia* with these thermo-acoustic phenomena.

The sounds generated in jet engines and rocket tubes by the combustion of fuel at some point therein hark back to the Rijke tube experiment. This scientist found that when a heated gauze was placed in the *lower* half of a vertical open tube, the latter sounded its natural frequency vigorously as long as the gauze remained hotter than the air column. The interest to physicists in these oscillations lies in the peculiar manner in which they are maintained. It seems that the heat is in most cases applied to the gas for a small fraction only of the period of vibration to give a compressional impulse to the fluid locally. As long, however, as this impulse occurs at the right phase, the vibration of the column is maintained. In effect, as Rayleigh showed, this means that the source of heat must be located in the lower half of the tube, but the obverse phenomenon, ascribed to Boscha, in which a column of hot air is caused to sing by the application of cold in the *upper* section, has been suggested as the cause of noise in certain cooling towers of power plants.

The relevance of these thermo-acoustic oscillations to the burning of pyrotechnics and rockets containing solid propellants was illustrated at the 1952 Symposium by Maxwell[11] and by Smith and Springer,[12] all of whom found instability and changes in the rate of combustion when the rocket started to "whistle." The latter pair of authors, verifying an idea put forward by Grad,[13] suggest that the erratic combustion of aircraft rockets arises from the production of sounds which are usually one or another of the proper frequencies of the pipe formed by the hollowed-out center or external annulus of the rocket charge.

Sound Scattering and Turbulence

The mode of attenuation of sound in the open air has become another matter of urgent interest since the noise level of aircraft propulsion has risen so alarmingly. Generally speaking in a fluid, apart from a fall of intensity from the source due to the increase in surface area of the wave front, the sound amplitude falls off with the square of the frequency, so that the ultrasonic and high sonic frequencies in a jet noise are fairly rapidly attenuated with distance. This effect is magnified often by the humidity of the atmosphere.

The early investigators on the propagation of sound in the atmosphere used either subjective observation or objective apparatus incapable of following rapid fluctuations. Consequently they were obliged to explain their results in terms of the continuing meteorological elements like mean wind and temperature, though they recognized that certain meteorological conditions led to an irregular signal when picked up at a distance from a steady source. It is only recently with the introduction of sensitive electrical devices that studies of the fluctuations in the signal received from a steady source of sound have been possible.

Another important effect is due to scattering of the sound by the eddies which exist in the atmosphere whenever it is turbulent—which, near the ground, is almost always. This turbulence is, to within a few inches of the ground, isotropic, that is to say, the eddies are of symmetrical form and of size from many yards down to an inch or two. As such they scatter sound rather in the fashion that the globules of water in a fog scatter light. The relevant parameter is the relation between circumference of the scattering entity (eddy) and the wave length. The air velocity in and around an eddy is of course fluctuating so that the scattering of sound is inconstant, rather like the flickering of the light from stars due to atmospheric variations of density.

These departures from the classical laws of sound propagation are to be ascribed to the turbulent nature of the atmosphere. The normal velocity c of sound in still air or in steady streaming is locally replaced by $c \pm \Delta c$, consequently we should expect a scattering of the sound from the direct path on the basis of the mean correlation coefficient R of turbulent motions over the path from source to listening post. Attempts have been made to set up theories which regard the eddy length as playing the part of the regions of abnormal refractive index which appear in Rayleigh's theory of light scattering, with its dependence on wave length λ and on the volume of the scattering entity in the form of v or l^3, l being the mean eddy diameter. There is, however, this difference, that the atmosphere is a medium of variable acoustic refrangibility without variable density—in the absence of thermal currents.

Lighthill[14] has applied his theory of sound generated

aerodynamically to this problem and has shown that the energy scattered per unit time from unit volume is

$$(8\pi^2 u^2/\lambda^2)\cdot(lI/c^2)$$

I being the incident sound intensity, l the mean eddy diameter, and u^2 the mean square velocity fluctuation.

It may be objected that such scattering does not attenuate sound but merely redistribute it. While this is true for a point source, whenever the source is directional as most jet sounds are, at any rate for the higher frequencies, scattering tends to smooth out the polar curve of intensity distribution and to upset phase relationships between sounds arriving at the listener by different paths, so that in fact the decibel loss per 1,000 ft. is greater in such an atmosphere than it would be in still fluid, the loss increasing with the square of the velocity fluctuation as Lighthill's formula shows.

The author[15] has carried out measurements of velocity fluctuations, by hot wires; temperature fluctuations, by thermocouples; sound intensity at a distance up to 100 ft. from a pure tone source, by microphones; and verified a number of features of the principles above expounded. In particular he has shown that some correlation exists between the fluctuations of sound intensity over the test range and intermediate fluctuations in both wind and temperature. Fig. 4 shows, for example, simultaneous fluctuations of velocity (as variations of hot-wire resistance) and sound intensity picked up at a height of 6 ft. over a grassy field. Such records, though they do not show an exact correlation between turbulence and sound propagation, do illustrate the effect of turbulent conditions on the root mean square sound pressure fluctuation within the medium, particularly when eddies comparable in size with the wave length of the sound are concerned.

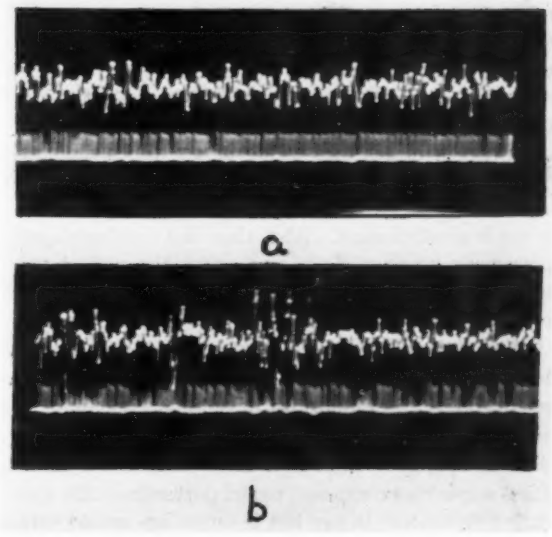

FIG. 4. Simultaneous records of velocity fluctuations in open air (*above*) and sound intensity (*below*)—*a*, sound of 4,000 cycles per sec., *b*, sound of 7,500 cycles per sec.

ACOUSTIC RELAXATION IN AERODYNAMICS

Finally, reference should be made to some acoustic aspects of the use of freons and other vapors to replace air in supersonic wind tunnels. The raison d'être of the substitution is, of course, to attain a given Mach Number in the flow for a smaller expenditure of power, since these vapors have low values of the velocity of sound. They have different values also for the ratio of specific heats γ but the users are prepared to correct for this and seem to be able to do so with success at least for Mach Numbers of the order of unity as a recent report by von Doenhoff, Braslow, and Schwartzberg[16] shows.

Certain questions arise, however, as to the exact correspondence of fields of flow even when the Reynolds Number and Mach Number are correct. The principal questions are:

(1) Does the change in γ significantly alter the flow field and, if it does, can a correction be made for this?

(2) Is the equation of state of the same form?

(3) Will the vapor condense due to the lowering of temperature in an expansion?

With regard to the variation of flow field with γ, von Doenhoff, Braslow, and Schwartzberg[16] have shown that, at a particular speed, variation of γ can be compensated by a change in the relative thickness of the model although a change in γ from 1.4 in air to 1.13 in freon involves an almost negligibly small change in the thickness/chord ratio. The speed range over which freon is an adequate substitute for air is, however, limited and is in fact from low speeds up to about 1.2 times the speed of sound.

If the relaxation time differs from that of air the whole flow pattern may be altered and some of the energy stays in the vibrational mode. The work of Miyahara and the author on the velocity of sound in the freons is pertinent. The relaxation time in freon 12, for example, is 1.5×10^{-7} sec. whereas that in air at sea level is 10^{-5} sec. This means that a shock taking place in freon at a local $M = 2$ ($U = 300$ m. per sec.) at a distance of 1/20 mm. in front of the nose would be completely relaxed in this distance, whereas the shock front in air would be scarcely affected in the corresponding passage. This one would think must affect the local pressure on the model.[17]

Chapman[18] who has recently examined the presumed behavior of models in substitute vapor tunnels in relation to full-scale flight at high altitudes points out that the important parameter in this connection is not the relaxation time itself but the product of it and the thermal capacity of the molecules in vibration. He shows that thermal capacity lag should be important in boundary layers at low Reynolds Numbers or high Mach Numbers. It may be important at high altitudes, so that to this extent, a tunnel filled with a relaxing vapor or mixtures of vapors may be superior to one filled with atmospheric air, especially for hypersonic flow.

Proximity of conditions in the working fluid to the critical state affect both questions (2) and (3). Assuming, say, van der Waals' equation, it would be possible

to make some modifications of the thermodynamic expressions for the pressures and temperatures in terms of the constants a and b of the equation, but a general formula of correction would be difficult to obtain. It has been estimated that the temperature may rise in places to a value of γ^{-1} times the static temperature. This sets a limit to the temperature at which a tunnel containing a vapor can be operated to avoid condensation. Also, there is a disadvantage in power consumption if one works near the critical state, for then the velocity and attenuation of sound are rapidly changing.

This rules out carbon tetrafluoride (one which has been suggested), but we are making sound measurements on the hexafluorides of sulphur, selenium and tellurium which look promising.

What precisely the high absorption coefficient in these vapors (as compared to air) portends in this application is difficult to say but it must, one would think, have an effect on the devolution of the shock wave front.

References

[1] Richardson, E. G., and Tyler, E., *Synthetische Turbulenz*, Vol. 32, p. 509, 1931.

[2] Schubauer, G. B., and Skramstad, H. K., *Laminar Boundary Layer Oscillations and Stability of Laminar Flow*, Journal of the Aeronautical Sciences, Vol. 14, No. 1, p. 69, 1947.

[2a] Tollmien, W., *Die Entstehung der Turbulenz*, Nach. Wiss. Ges., Göttingen, Math.-Phys. Klasse, p. 21, 1929.

[2b] Schlichting, H., *Berechnung der Anfachen kleine Störungen bei der Plattenströmung*, Z. f. ange. Math. u. Mech., Vol. 13, p. 171, 1933.

[3] Fage, A., and Townend, H. C. H., *Examination of Turbulent Flow with the Ultramicroscope*, Proc. Roy. Soc., Vol. 135A, p. 656, 1932.

[4] Holtzmark, J., Johnsen, I., Sikkeland, T., and Skavlem, S., *Boundary Layer Near a Cylindrical Obstacle in an Oscillating Incompressible Fluid*, Journal of the Acoustical Society of America, Vol. 26, p. 26, 1954.

[5] Schuh, H., and Winter, K. J., *R.A.E. Low Turbulence Wind Tunnel, Part III, Measurement of Turbulence Intensity and Noise with Improved Apparatus*, R.A.E. Rep. Aero., 2412, 1951.

[6] Powell, A. J., *Edge Tones and Associated Phenomena*, Acustica, Vol. 3, p. 233, 1953.

[7] Nyborg, W. L., *Self Maintained Oscillations of a Jet in a Jet-Edge System, Parts I and II*, Journal of the Acoustical Society of America, Vol. 26, p. 174, 1954.

[8] Richardson, E. G., *Edge Tones*, Proc. Phys. Soc. London, Vol. 43, p. 460, 1931.

[9] Curle, N., *Mechanics of Edge Tones*, Proc. Roy. Soc., Vol. 216A, p. 412, 1953.

[10] Richards, E. J., *Jet Engine Noise*, J. Roy. Aero. Soc., Vol. 58, pp. 221–223, 1954.

[10a] Hubbard, H. H., and Lassiter, L. W., *Experimental Studies of Noise from Subsonic Jets in Still Air*, NACA TN 2757, 1952.

[10b] Lilley, G. M., and Westley, R., *The Noise Field from a Small Jet and Methods for its Reduction*, Coll. Aeronautics Rep. 53, 1952; see also J. Roy. Aero. Soc., Vol. 58, p. 235, 1954.

[11] Maxwell, W. R., *Pyrotechnic Whistles*, Fourth Symposium on Combustion, p. 906, Williams and Wilkins, Baltimore, 1953.

[12] Smith, R. P., and Springer, D. F., *Sonic Cause of Instability in Rockets*, Fourth Symposium on Combustion, pp. 893–905, Williams and Wilkins, Baltimore, 1953.

[13] Grad, H., *Straight Pipe Jet Motors*, Comm. Pure and Appl Maths., Vol. 2, pp. 71–77, 1949.

[14] Lighthill, M. J., *Energy Scattered from Interaction of Turbulence with Sound Waves*, Proc. Roy. Soc., Vol. 211A, pp. 564–585, 1952.

[15] Richardson, E. G., *Fine Structure of Atmospheric Turbulence in Relation to the Propagation of Sound Near the Ground*, Proc. Roy. Soc., Vol. 203A, p. 412, 1952.

[16] Von Doenhoff, A. E., Braslow, A. L., and Schwartzberg, M. A., *Studies of the Use of Freon 12 as a Wind-Tunnel Testing Medium*, NACA TN 3000, 1954.

[17] Kantrowitz, A., *Effects of Heat Capacity Lag in Gas Dynamics*, J. Chem. Phys., Vol. 10, p. 145, 1942.

[18] Chapman, D. R., *Some Possibilities of Using Gas Mixtures Other than Air in Aerodynamic Research*, NACA TN 3226, 1954.

The Ultimate Strength of Multiweb Box Beams in Pure Bending

ROBERT A. NEEDHAM*

University of California, Los Angeles

ABSTRACT

A method for predicting the ultimate bending strength of multiweb box beams having formed sheet metal webs is presented. Equations are derived on the assumption that the ultimate moment is reached when local crippling occurs at the junctions of the webs and the compression skin. The proposed theory is compared with 49 beams fabricated from 75S-T6 sheet and tested by the NACA. The agreement between tests and theory was extremely good.

NOTATION

b	=	flange width of shear web, in.
B	=	total width of box, in.
C_e	=	edge support coefficient for compression crippling, dimensionless
E	=	Young's modulus in compression, ksi.
E_s	=	secant modulus in compression, ksi
E_t	=	tangent modulus in compression, ksi.
F_{cy}	=	compression yield stress (0.002 offset), ksi.
$F_{0.7}$	=	0.7 secant yield stress, ksi.
F_{ccs}	=	compression crippling stress of skin, ksi.
F_{ccw}	=	compression crippling stress of flange of shear web, ksi
h	=	equivalent box height, in.
h_e	=	effective box height, in.
$\bar{M}$	=	allowable bending moment of interior web unit, in.lb.
$\bar{M}_0$	=	exterior web correction, in.lb.
m	=	allowable moment per inch of box width, in.lb./in.
n	=	number of webs in box
P_f	=	allowable load in compression flange, lb.
t_s	=	skin thickness, in.
t_w	=	web thickness, in.
w_e	=	von Kármán effective width, in.
x	=	exponent in Ramberg-Osgood equation, dimensionless
η	=	inelastic compression modulus ratio, dimensionless
b'/t	=	equivalent flange b/t, dimensionless
k	=	$1.03\sqrt{\eta}\sqrt[4]{E/F_{cy}}$

INTRODUCTION

RECENT TRENDS IN WING DESIGN are toward the use of heavy skin surfaces employing various schemes of stabilizing the compression cover. The more common types under investigation include multiweb, post-stiffening, double skin, and deep stringer constructions. Of the various types of structural configurations for the thin wing, the multiweb box consisting of heavy plate surfaces with a series of moderately light sheet metal webs appears promising, both from the standpoint of simplicity of construction and structural efficiency. In its simplest form, the multiweb box is shown in Fig. 1a. For the purpose of analysis, the wing structural box is idealized as shown in Fig. 1b. The variable height, h, of the actual box is replaced by an "equivalent" height, $\bar{h}$, resulting in a rectangular box of the same width, B, and number of webs as the actual wing.

The ultimate strength of a multiweb box beam in pure bending will be reached when the crippling stress at the junction of the webs and skin on the compression surface is reached. Failure may or may not be preceded by skin buckling, depending upon the proportions and material of the box. Crushing of the webs normal to the plane of the skin (general instability) can be eliminated as a failure mode in a well-proportioned box since there is adequate experimental evidence to indicate that the crushing forces in the webs are small.[1]

BENDING STRENGTH OF MULTIWEB BOX BEAMS

Consider the rectangular box beam of Fig. 2a which has n vertical webs riveted to the upper and lower skins. In the analysis that follows, the following is assumed.

(1) Spanwise rivet spacing is such that inter-rivet buckling is precluded.

(2) The distance b_1 (Fig. 2b) is a minimum consistent with good fabricating practice.

(3) The effective bending element contributed by a vertical web is an equal angle having leg widths b and a thickness t_w.

(4) The effective bending element contributed by the skin consists of two effective widths of skin, w_e, having a thickness t_s.

(5) All vertical webs are of the same thickness, the upper and lower skins are the same thickness, and the flange width, b, is constant for all flanges.

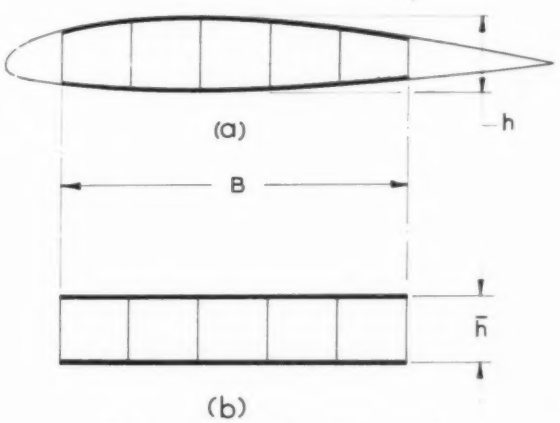

FIG. 1. Actual and idealized wing box.

Received November 3, 1954.

* Associate Research Engineer.

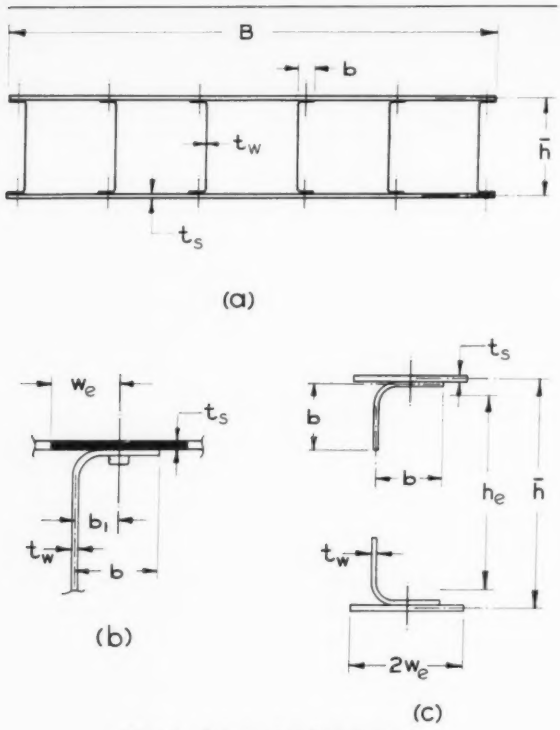

FIG. 2. Interior bending element.

On the basis of the above assumptions, the effective bending section of an interior web-skin combination is shown in Fig. 2c.

In a recent paper[2] the author presented a method of predicting the compression crippling stress of formed sheet metal structural shapes. The proposed method was based on the assumption that a formed structural shape consisting of a series of flat plate elements could be treated as a series of angle sections possessing various degrees of edge support parallel to the direction of loading. A general equation of the form

$$F_{cc} = (C_e\sqrt{F_{cy}E})/(b'/t)^{0.75} \qquad (1)$$

was developed from extensive tests of channel- and angle-sections of 24S-T plain (unclad) and 24S-T3 and 75S-T6 clad sheet. Fig. 3 illustrates the significance of C_e and b'. Eq. (1) can be placed in convenient nondimensional form by plotting $F_{cc}/\sqrt{F_{cy}E}$ against (b'/t). Such a plot, applicable to the alloys mentioned above, is shown in Fig. 4.

Well-proportioned box beams of the type under consideration will fail in bending when the local crippling stress at the web-skin junction is reached. In isolated cases, the material of the web will be different from the material of the skin, and stresses in excess of the proportional limit of one of the materials of the combination will result in a stress of a different magnitude in the other. A close approximation of the local crippling failure of these combinations can be obtained by assuming equal strains at the point of attachment of the web and the skin. Consider the skin-web combination of Fig. 2b. The crippling stress, F_{ccw}, of the assumed web angle can be obtained from Eq. (1). Since both flanges of the angle are supported (one flange by the web and the other by the skin riveting) the edge support coefficient, C_e, of 0.366 is used (Fig. 3c). The crippling stress in the sheet ($= F_{ccs}$) at the web crippling stress is obtained from the combined compression stress-strain diagrams of the two materials, as shown in Fig. 5. A "weighted" crippling stress of the skin-web combination is obtained in the usual manner from

$$F_{cc} = [(F_{ccw})t_w b + (F_{ccs})t_s w_e]/(t_w b + t_s w_e) \qquad (2)$$

Only the more usual case of identical materials in the webs and the skin will be treated here. At failure, the total axial load in the compression flange is given by

$$P_f = F_{cc}[n(2w_e t_s + 2bt_w) - 2w_e t_s] = 2w_e t_s F_{cc}\{n[(bt_w)/(w_e t_s) + 1] - 1\} \qquad (3)$$

where $2w_e$ is the effective width of the skin acting at the web flange stress and n is the number of webs in the box.

For purposes of analysis, the *structural index*, as suggested by Shanley,[3] will be introduced here. For the "wide column"—i.e., the entire compression flange of the box—the structural index becomes M/Bh_e^2. Note that M/B represents the moment per inch of chord, m. If the resisting moment at failure is defined by $P_f h_e$, Eq. (3) becomes

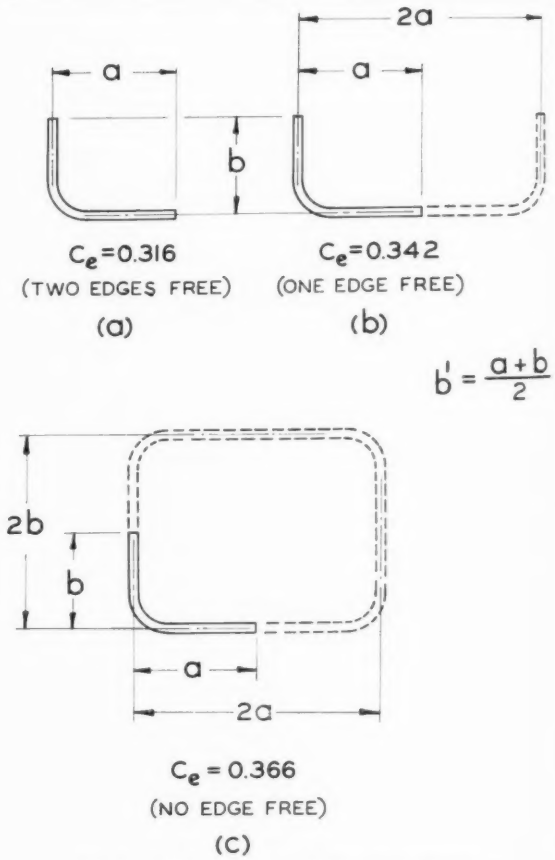

FIG. 3. Edge support coefficients for crippling.

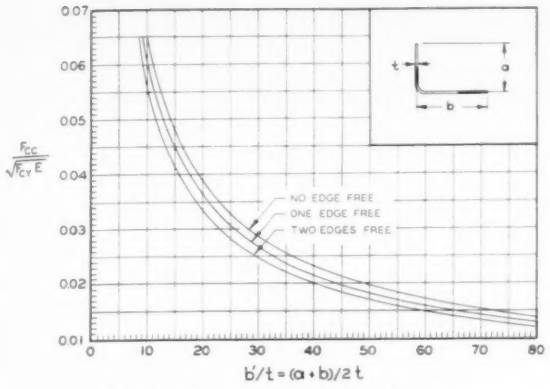

FIG. 4. Dimensionless crippling stress.

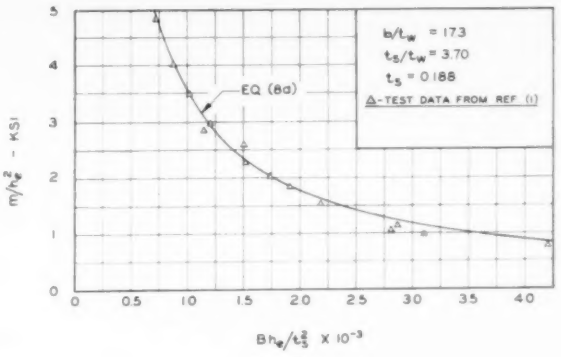

FIG. 7.

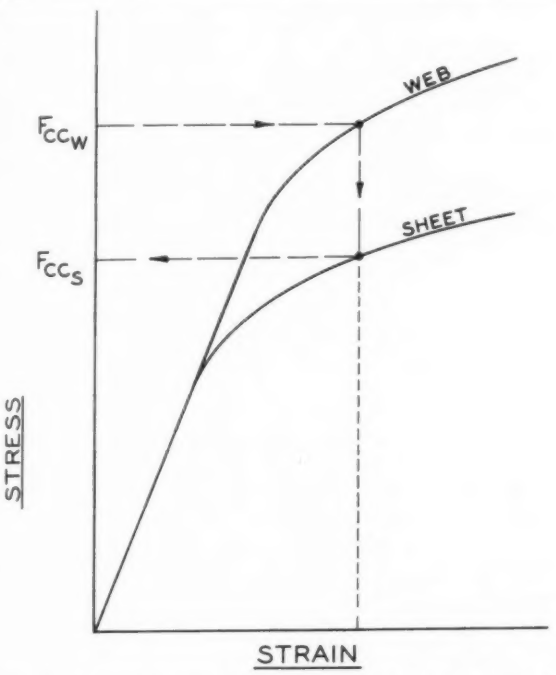

FIG. 5. Method of obtaining stress in sheet (web and sheet of two different materials).

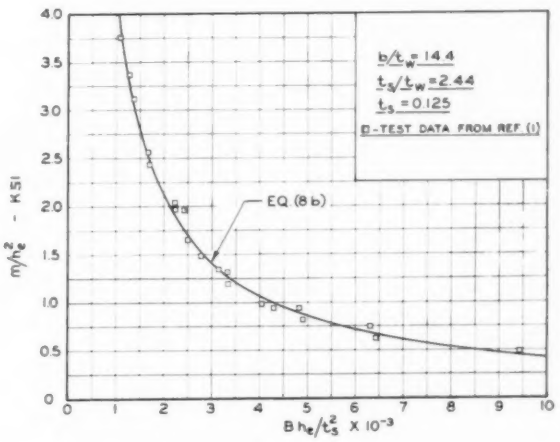

FIG. 8.

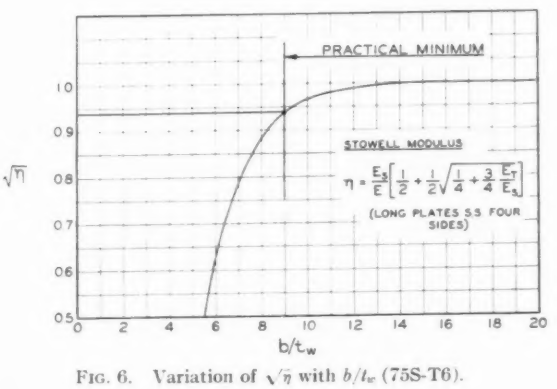

FIG. 6. Variation of $\sqrt{\eta}$ with b/t_w (75S-T6).

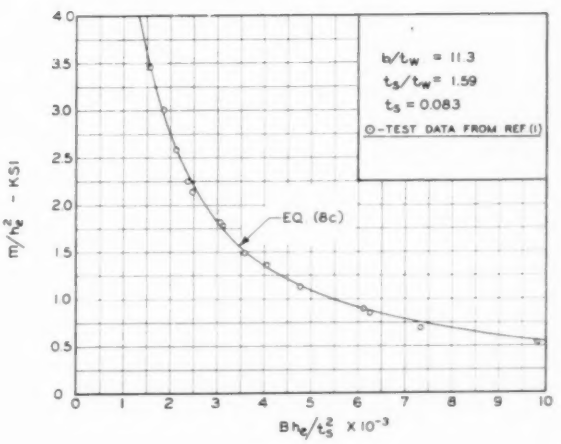

FIG. 9.

$$m/h_e^2 = [(2w_e t_s)/(Bh_e)]F_{cc}\{n[(bt_w)/(w_e t_s) + 1] + 1\} \quad (4)$$

The effective width of sheet may be obtained from the von Kármán equation[4] modified to account for inelastic effects. This equation is

$$w_e/t = 0.85\sqrt{\eta}\,\sqrt{E/F_{cc}} \quad (5)$$

Values of η are obtainable from Stowell's Equation[5] for long plates simply supported on four edges—viz.,

$$\eta = (E_s/E)[(1/2) + (1/2)\sqrt{(1/4) + (3/4)(E_t/E_s)}] \quad (6)$$

Substituting Eqs. (1) and (5) in Eq. (4) and simplifying

$$\frac{m}{h_e^2} = \frac{k\sqrt{F_{cy}E}}{(Bh_e/t_s^2)(b/t_w)^{3/4}} \times \left\{n\left[\frac{2C_e(b/t_w)^{3/4}}{k(t_s/t_w)^2} + 1\right] - 1\right\} \quad (7)$$

where $k = 1.03\sqrt{\eta}\,\sqrt[4]{E/F_{cy}}$.

Comparison Between Theory and Test

A well-proportioned aluminum alloy box beam of the type under consideration will develop a stress at the junction of the webs and the skin close to the yield stress of the material, in which case, $E_s/E \cong 0.7$ and $E_t/E \cong 0.2$. The corresponding value of η [Eq. (6)] is 0.59. In any case, however, η can be obtained from Eq. (6) at the web flange crippling stress, $F_{cc} = 0.366\sqrt{F_{cy}E}/(b/t_w)^{3/4}$, and the stress-strain diagram of the material.

Reference 1 contains the results of 53 pure bending tests of 75S-T6 multiweb box beams of the type for which Eq. (7) was developed. Of the 53 tests, 49 had four vertical webs; hence, in Eq. (7), $n = 4$. The average value of F_{cy} for these tests was 72,200 lbs. per sq.in. Assuming a value of Young's modulus of 10,500 ksi, Eq. (7) becomes

$$\frac{m}{h_e^2} = \frac{3{,}100{,}000\sqrt{\eta}}{(Bh_e/t_s^2)(b/t_w)^{3/4}} \times \left\{4\left[\frac{0.204(b/t_w)^{3/4}}{\sqrt{\eta}\,(t_s/t_w)^2} + 1\right] - 1\right\} \quad (8)$$

The tests of reference 1 were divided into three groups. Within each group the following quantities were held constant:

Specimen numbers	b/t_w	t_s/t_w	Av. skin thickness, t_s
1–14	17.3	3.70	0.188
15–35	14.4	2.44	0.125
40–53	11.3	1.59	0.083

To facilitate the determination of $\sqrt{\eta}$, Fig. 6 was prepared.* Since reference 1 did not contain compressive stress-strain diagrams, the Ramberg-Osgood equation,[6]

$$E\epsilon/F_{0.7} = (F/F_{0.7}) + (3/7)(F/F_{0.7})^x$$

with a value of x of 10, was assumed to hold. The 0.7 secant yield stress was obtained from the equation[7]

$$F_{0.7} = (F_{cy})^{x/(x-1)}/(E/214.3)^{1/(x-1)}$$

Values of $\sqrt{\eta}$ for the three ratios of b/t_w are listed below.

Specimen numbers	b/t_w	$F_{cc} = \frac{0.366\sqrt{F_{cy}E}}{(b/t_w)^{0.75}}$	F_{cc}/F_{cy}	$\sqrt{\eta}$
1–14	17.3	35,700	0.520	1.000
15–35	14.4	43,200	0.598	0.998
40–53	11.3	51,700	0.716	0.980

Eq. (8) becomes:

for specimens 1–14 ($h_e = \bar{h} - 0.062b$)

$$m/h_e^2 = 3{,}570{,}000/(Bh_e/t_s^2) \quad (8a)$$

for specimens 15–35 ($h_e = \bar{h} - 0.138b$)

$$m/h_e^2 = 4{,}240{,}000/(Bh_e/t_s^2) \quad (8b)$$

and for specimens 40–53 ($h_e = \bar{h} - 0.192b$)

$$m/h_e^2 = 5{,}490{,}000/(Bh_e/t_s^2) \quad (8c)$$

These equations are compared with the test data from reference 1 in Figs. 7, 8, and 9. In the above equations, h_e is the distance between flange centroids (Appendix B).

Design Curves

The development of design curves for predicting the ultimate moment of a multiweb box beam in pure bending can be simplified by considering a "unit" of the beam as made up of a single interior web and its accompanying effective width of skin (Fig. 2c). If $\bar{P}_f$ is the allowable flange load per web,

$$\bar{P}_f = F_{cc}(2w_e t_s + 2bt_w)$$

and the allowable moment, $\bar{M}$, per interior web is

$$\bar{M} = \bar{P}_f h_e = 2w_e t_s h_e F_{cc}\{[(bt_w)/(w_e t_s)] + 1\} \quad (9)$$

Dividing Eq. (9) by $h_e t_s^2$

$$\bar{M}/(h_e t_s^2) = 2F_{cc}(w_e/t_s)\{[(b/t_w)/(w_e/t_s)](t_w/t_s) + 1\}$$

and from Eqs. (1) and (5)

$$\frac{\bar{M}}{h_e t_s^2} = \frac{k\sqrt{F_{cy}E}}{(b/t_w)^{3/4}}\left[\frac{0.732(b/t_w)^{3/4}}{k(t_s/t_w)^2} + 1\right] \quad (10)$$

Eq. (10) is plotted for 75S-T6 aluminum alloy (minimum guaranteed properties) in Fig. 10 for those cases where $t_s \geq t_w$ and $50 \geq b/t_w \geq 9$.†

* See Appendix A for development of Fig. 6.

† For the type of construction under consideration, a value of b/t_w of about 9 represents the practical minimum due to clearance problems in installing web-flange rivets.

A multiweb box having n-webs will develop a bending moment equal to n-times the value given by Eq. (10). For precise results, however, a correction must be introduced to account for the fact that the exterior webs each have but one effective width of skin. It is therefore necessary to subtract the amount of resisting moment due to $2w_e$ of skin. This correction, expressed in terms of the parameter $\bar{M}/h_e t_s^2$, is derived in a manner analogous to Eq. (10), is given by

$$\bar{M}_0/(h_e t_s^2) = (k\sqrt{F_{cy}E})/(b/t_w)^{3/4} \qquad (11)$$

and is plotted for 75S-T6 in Fig. 11.

As an example of the use of the design charts, assume a 75S-T6 multiweb box beam of the following proportions.

$t_w = 0.051$ in.
$t_s = 0.125$ in.
$\bar{h} = 3.76$ in.
$b = 0.74$ in.
$n = 8$
$t_s/t_w = 2.45$
$b/t_w = 14.5$
$h_e = 3.66$ in. [Eq. (B-1), Appendix B]

From Fig. 10 $\bar{M}/h_e t_s^2 = 1{,}320{,}000$ lbs. per sq.in. From Fig. 11 $\bar{M}_0/h_e t_s^2 = 1{,}120{,}000$ lbs. per sq.in. The allowable bending moment for the box is

$$M = (n \times 1{,}320{,}000 - 1{,}120{,}000)h_e t_s^2$$
$$= 9{,}440{,}000 \times 3.66 \times (0.125)^2$$
$$= 540{,}000 \text{ in.lb.}$$

References

[1] Pride, R. A., and Anderson, M. S., *Experimental Investigation of the Pure Bending Strength of 75S-T6 Aluminum Alloy Multiweb Beams with Formed Channel Webs*, NACA TN 3082, March, 1954.

[2] Needham, R. A., *The Ultimate Strength of Aluminum Alloy Formed Structural Shapes in Compression*, Journal of the Aeronautical Sciences, Vol. 21, No. 4, p. 217, April, 1954.

[3] Shanley, F. R., *Principles of Structural Design for Minimum Weight*, Journal of the Aeronautical Sciences, Vol. 16, No. 3, p. 133, March, 1949.

[4] von Kármán, Th., Sechler, E. E., and Donnell, L. H., *The Strength of Thin Plates in Compression*, ASME Trans., APM-54-5, Vol. 54, No. 2, June 30, 1932.

[5] Stowell, E. Z., *A Unified Theory of the Plastic Buckling of Columns and Plates*, NACA TN 1556, April, 1948.

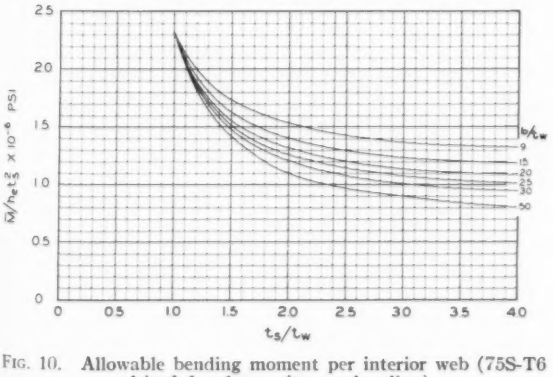

FIG. 10. Allowable bending moment per interior web (75S-T6 multiweb box beams in pure bending).

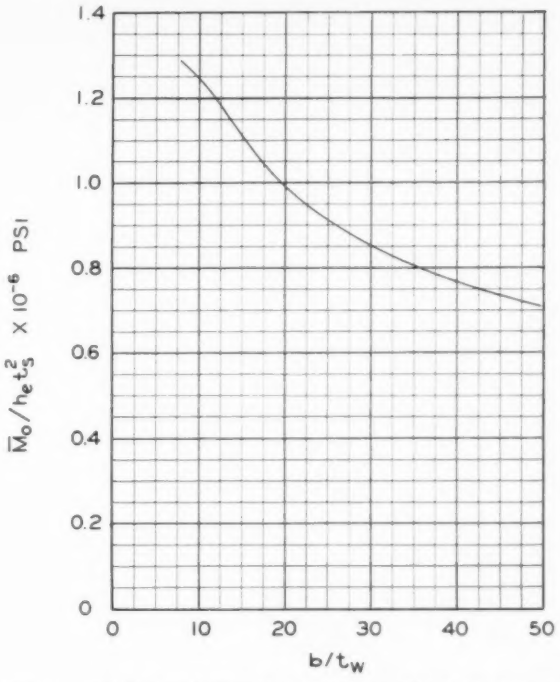

FIG. 11. Exterior web correction (75S-T6 multiweb box beams in pure bending).

[6] Ramberg, W., and Osgood, W. R., *Description of Stress-Strain Curves by Three Parameters*, NACA TN 902, July, 1943.

[7] Needham, R. A., *Permanent Buckling of Sheet-Stringer Panels at Elevated Temperatures*, WADC TR 53-209, July, 1953.

Appendix A

The plot of $\sqrt{\eta}$ vs. b/t_w (Fig. 6) was obtained as follows: For a given material, such as 75S-T6 aluminum alloy, values of $\sqrt{\eta}$ as a function of stress were obtained from the stress-strain diagram and Stowell's Equation [Eq. (6)]. Rewriting Eq. (1) with $C_e = 0.366$ (angle sections supported on two edges),

$$F_{cc}/F_{cy} = [0.366/(b/t_w)^{3/4}]\sqrt{E/F_{cy}} \qquad (A\text{-}1)$$

The quantity $\sqrt{\eta}$ can also be expressed as a function of F_{ce}/F_{cy} by assuming the stress, F_c, obtained from the stress-strain diagram, equal to F_{cc} and dividing all values of F_{cc} by the yield stress. Thus Eq. (A-1) becomes

$$F_{cc}/F_{cy} = (0.366\sqrt{E/F_{cy}})/(b/t_w)^{3/4} = f(\sqrt{\eta}) \qquad (A\text{-}2)$$

from which $\sqrt{\eta}$ is expressed in terms of b/t_w as in Fig. 6.

Appendix B

The effective height, h_e, of the element shown in Fig. 2c is obtained from the relation

$$h_e = \bar{h} + 2\bar{y} \qquad (B\text{-}1)$$

where

$$y = \frac{b}{2}\left\{\left(\frac{1}{2}\,\frac{b}{t_w} + \frac{t_s}{t_w} + 1\right)\Big/\left[\frac{b}{t_w} + \frac{w_e}{t_s}\left(\frac{t_s}{t_w}\right)^2\right]\right\} \tag{B-2}$$

Eq. (B-2) was derived assuming the centroid of the angle at a distance $b/4$ from the median line of the leg of the angle that is riveted to the cover sheet. The ratio w_e/t_s is obtained from Eqs. (5) and (1) as

$$w_e/t_s = 1.365k(b/t_w)^{1/3}$$

where, as before, $k = 1.03\sqrt{\eta}\,\sqrt[4]{E/F_{cy}}$.

Design Charts for Transient Temperature Distribution . . .

(*Continued from page 762*)

the temperature potential for heat-transfer from the boundary layer to the wall is also a function of time. The design charts represent many possible solutions not considered here for lack of space. The generalization of the present analytical solution of the one-dimensional heat flow problem to other cases will be given in a separate publication, but the present design charts will not be changed.

The methods of using these design charts are illustrated by two detailed numerical examples, based on a previous study[1] of a wedge-shaped wing moving at supersonic speeds. These examples show that the design charts yield answers that are as accurate as those obtained previously by laborious numerical integration of the heat-flow equations. Furthermore, the time required to obtain the answers with the use of the design charts is a small fraction of the time needed in numerical integrations, since the entire history need not be computed when using the design charts. It is also evident that the two-dimensional heat flow in a thin object moving at supersonic speeds can be solved using the design charts by obtaining a series of solutions for one-dimensional heat flows adjacent to one another, each normal to the chord of the object.

References

[1] Kaye, J., *The Transient Temperature Distribution in a Wing Flying at Supersonic Speeds*, Journal of the Aeronautical Sciences, Vol. 17, No. 12, pp. 787–808, December, 1950.

[2] Kaye, J., *A Table of the First Eleven Repeated Integrals of the Error Function*, J. Math. and Phys., M.I.T. (to be published).

Notice to Contributors

Manuscripts submitted for publication *must* be double- or triple-spaced originals. There should be wide margins on both sides of the sheets and triple spacing around formulas to allow for the marking of directions for the printer.

Original drawings (jet black India ink on white paper or tracing cloth) should accompany the manuscript. *(Blueprints are not acceptable.)* Photographs *must* be on glossy white paper. The smallest lettering on 8- by 10-in. figures should be no less than 1/4 in. high.

Only the simplest formulas should be typewritten; all others should be carefully written in pen and ink. The difference between capital and lower-case letters and Greek symbols should be clearly distinguished.

See Inside Back Cover of this issue for further details

A Rigorous Method for Finding the Lift of a Certain Class of Airfoils and Remarks on the Meaning of Schrenk's Approximate Rule

OTTO LAPORTE* AND HIDEO YOSHIHARA†
University of Michigan

Introduction

SOME YEARS AGO, one of the authors[1] published a method for finding on the basis of the lifting line theory, the exact lift distribution for a certain rather general class of airfoils. With the exception of the elliptic plan form this had previously only been possible by elaborate numerical methods. While for a given plan form these latter methods will still have to be used, it seems desirable to have exact solutions available for a plan form family characterized by two parameters, namely, aspect ratio and taper.

The plan form which is investigated in the following has zero sweep and is given by

$$c(y) = c_0\sqrt{[1 - (2y/b)^2]}\,\sqrt{[1 - t(2y/b)^2]} \quad (1)$$

In this formula, y is the span coordinate, b is the span, c is the chord at y, c_0 is the maximum chord at the center of the wing. The occurrence of a second constant t, which may be called the taper constant, is new. For $t = 0$ the above plan form degenerates into the elliptic one; for t between 0 and 1 wings, which are more tapered than an ellipse; and for t between 0 and -1 wings blunter than the ellipse result. In the paper cited, only untwisted wings were discussed. Since that time it has been possible (1) to shorten and simplify the analysis given there to a certain degree, and (2) to extend the theory to the case of twisted wings—i.e., to cases where the angle of attack is a function of y. These developments constitute the first part of this paper.

In this way, exact lift formulas are available for the first time for a comparatively wide class of plan forms. It seems, therefore, an inviting prospect to investigate to what extent the approximate method of Schrenk[2] compares with the exact formulas. Although this approximate method is widely used in the industry, any theoretical justification has been lacking.

It is seen that for untwisted wings Schrenk's rule arises out of a simple approximation performed on our rigorous formulas. Since the meaning of this approximation can be recognized in general, there results a generalization of Schrenk's rule which is independent of plan form and applicable to any kind of twist or even discontinuous α distribution.

Description of the Method

According to Trefftz,[3] the problem of the wing regarded as a lifting line may be reduced to the following potential problem in the y, z plane perpendicular to the direction of flight: a potential function $\varphi(y, z)$ satisfying Laplace's equation

$$\Delta\varphi = 0 \quad (2)$$

which possesses a line of discontinuity or a branch cut on the y axis for y between $-(b/2)$ and $(b/2)$. This line of discontinuity is the projection of the wing of span b on to the y, z plane. On the upper side of this slit $\varphi(x, y)$ must satisfy the following boundary condition:‡

$$\left(\frac{\partial\varphi}{\partial z}\right)_{z=0} - \frac{8\varphi(y, 0)}{mc(y)} = -V\alpha(y) \quad (3)$$

Furthermore,

$$\varphi(y, +0) = -\varphi(y, -0) \quad (4)$$

while the normal derivative is continuous. In Eq. (3), V is the velocity of the air at infinity, $\alpha(y)$ is the angle of attack which may vary arbitrarily as a function of span, $c(y)$ is the chord or plan form and m is the slope of the lift curve as it results from the infinite span theory. The connection between the potential and the section lift at y or the downwash velocity is given by

$$l(y) = 4\rho V\varphi(y, 0); \qquad w(y) = [\partial\varphi(y, z)/\partial z]_{z=0} \quad (5)$$

In potential theory a problem such as the present one is called a boundary value problem of the "third kind," because a linear combination of the function and its normal derivative (in fact, a linear combination with a variable coefficient) is to assume a given value. It may be noted, for future reference, that if the function φ itself is to assume given values we have a boundary value problem of the "first kind," while if the normal derivative is prescribed on the boundary the boundary value problem is said to be of the "second kind."

The reason why the present problem does not lend itself readily to analytic attack is that a variable coef-

Received November 3, 1954.

* Professor of Physics.

† Formerly, University Fellow, Rackham School of Graduate Study, University of Michigan. Now, Chief, Theoretical Aerodynamics Section, Wright Air Development Center, USAF.

‡ See e.g., reference 4, pp. 98–112.

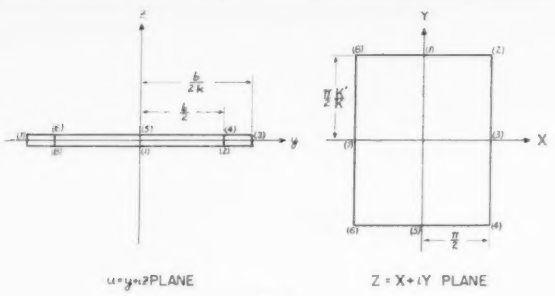

FIG. 1.

ficient occurs in Eq. (3). Thus in the past, solutions have usually been obtained by more or less numerical methods. (The only exception to this is the elliptic wing.) The idea underlying the present paper is the following: if in the y, z plane a conformal transformation to new variables, say X and Y, is carried out the differential equation (2) is not affected. Because of the occurrence of the first derivative, however, the boundary condition (3) will change; in fact each transformation $(y, z) \rightarrow (X, Y)$ will cause a new variable coefficient to appear both in the φ term and on the right-hand side of Eq. (3). We propose to carry out a conformal transformation and then to choose such a chord function $c(y)$ that in the new variables a boundary condition with constant coefficients results. This new problem will then be treated with standard methods.

First Type of Conformal Mapping of the Trefftz Plane into a Rectangle

We regard y and z as one complex variable by putting[4]

$$u = y + iz$$

It should be remembered that the trace of the wing is a slit on the real axis extending from $y = -(b/2)$ to $+(b/2)$. The region outside this slit will now be mapped onto a complex plane

$$Z = X + iY$$

by means of the function*

$$u = (b/2K)ns[(2/\pi)KZ, K] \qquad (6)$$

In this equation Z is the complex variable. k is a constant parameter called the modulus which we will assume to be real and between 0 and 1, K is the complete elliptic integral of the first kind of k. $ns(x, K)$ is the reciprocal of the elliptic function[5] $sn(x, k)$ of argument x and modulus k. The mapping of Eq. (6) is illustrated in Fig. 1 by denoting corresponding points in the two planes by identical numbers. The essential features arise as follows:

(a) $Z = 0$ gives, since sn of vanishing argument vanishes, the infinitely distant point $u = \infty$.

(b) The upper or lower sides of the rectangle $Z = X \pm i(\pi/2)\ (K'/K)$, where $K' = K(k')$ with $k^2 + k'^2 = 1$, map, respectively, into the lower or upper side of the slit along the real axis of the u plane between $y = \pm(b/2)$. This is seen by calculating

$$u = (b/2k)ns(2/\pi)K[X \pm i(\pi/2)\ (K'/K) \mp i\epsilon(\pi/2K)]$$

A small increment ϵ is added here, to enable us to investigate not only points on, but also points near, the sides of the rectangle. We obtain[6]

$$u = (b/2)\ [sn(2/\pi)KX \mp i\epsilon cn(2/\pi)KX\ dn(2/\pi)KX] \qquad (7)$$

Thus both edges of the rectangle become the real y axis from $-(b/2)$ to $+(b/2)$. We have therefore to imagine that the u plane is cut open along this piece of its real axis.

(c) We turn to the sides of the rectangle by calculating the u values which go with $Z = \pm(\pi/2) + iY$:

$$u = (b/2k)ns[\pm K + i(2/\pi)KY]$$

that is to say,

$$y = \pm(b/2k)dn[(2/\pi)KY, K'] \qquad (7')$$

Since dn of a real argument is real (and even) u will be real. The corners of the rectangle $Y = \pm(\pi/2)\ (K'/K)$ must give the same map points as under (b); since $dn(\pm K', k') = k$ we get, indeed, $u = \pm b/2$. As Y diminishes from $+\ \pi K'/2K$ to zero, dn increases from k to 1. The points in the u plane which correspond to the midpoints of the two vertical sides of the rectangle are therefore the points $u = y = \pm b/2k$. Since k is less than 1, they lie beyond $\pm b/2$. One sees in this way that the branch cut on the real axis has to be lengthened to $\pm(b/2k)$.

Solution of the Problem in the Z Plane for Tapered Wings

The boundary value problem in the "physical" u plane was stated in the first section. Since by Eqs. (6) this u plane is mapped into the Z plane, the boundary value problem should be restated in terms of this new variable. It is clear that the solution of the problem requires the construction of a velocity potential $\varphi(X, Y)$, satisfying Laplace's equation (with X and Y as independent variables) which fulfills different boundary conditions on the various sides of the rectangle.

Eq. (3) states the boundary condition for $z = +0$, $|y| \leq (b/2)$. Since this line becomes the lower side of the rectangle, $Y = -(\pi/2)\ (K'/K)$; $|X| \leq (\pi/2)$, it is clear that now the boundary condition is

$$\left(\frac{\partial \varphi}{\partial Y}\right)_{Y=-\pi K'/2K} - \frac{8}{mc}\left(\frac{du}{dZ}\right)_{Y=-\pi K'/2K} \varphi\left(X, -\frac{\pi K'}{2K}\right) = -V\alpha\left(\frac{du}{dZ}\right)_{Y=-\pi K'/2K} \qquad (8)$$

with

* From here on the presentation is different from and simpler than the original derivations published in Quart. Appl. Math., 1944.

$$\left(\frac{du}{dZ}\right)_{Y=-\pi K'/2K} = \frac{b}{2}\frac{d}{dX}\,sn\,\frac{2}{\pi}KX \qquad (9)$$

The latter results from Eq. (7). In order that this boundary condition have constant coefficients we choose $c(y)$ proportional to du/dZ. To see what plan form this leads to it becomes necessary to write Eq. (9) in terms of the original span coordinate y. This is readily done using Eq. (7) and gives

$$\left(\frac{du}{dZ}\right)_{Y=-\pi K'/2K} = \frac{bK}{\pi}\sqrt{1-\left(\frac{2y}{b}\right)^2}\times \sqrt{1-k^2\left(\frac{2y}{b}\right)^2} \qquad (9')$$

Thus we are led to Eq. (1), but since k is supposed to be real and a genuine fraction, only wings of taper greater than elliptic result. Calling c_0 the maximum chord at the center, the area S of the wing is calculated readily* in terms of the two complete elliptic integrals E and K:

$$\left.\begin{aligned} S &= bc_0G(k) \\ G(k) &= (1/3k^2)\,[(1+k^2)E-(1-k^2)K] \end{aligned}\right\} \qquad (10)$$

The aspect ratio $\mathfrak{a} = b^2/S$ and the average chord $\bar{c}$ become, with this notation,

$$\mathfrak{a} = b/(Gc_0); \qquad \bar{c} = Gc_0 \qquad (10')$$

Substituting Eqs. (9) and (9′) into Eq. (8) and using Eq. (10′), the boundary condition at the lower side of the rectangle of Fig. 1 becomes

$$\left(\frac{\partial\varphi}{\partial Y}\right) - \frac{8}{\pi}\frac{\mathfrak{a}}{m}GK\varphi = V\alpha\,\frac{b}{2}\frac{d}{dX}\,sn\,\frac{2}{\pi}KX \qquad (11)$$

At the upper side the sign of the second term has to be reversed in view of Eq. (4). From here the solution of the problem proceeds according to standard methods. Let the right-hand side of Eq. (11) be expanded in a Fourier series for $|X| \leq (\pi/2)$:

$$\alpha\frac{d}{dX}\,sn\,\frac{2}{\pi}KX = \sum_{n=0}^{\infty} a_n \cos(2n+1)X \qquad (12)$$

The assumption will be made here that the angle of attack is a symmetric function of y and therefore of X, otherwise sine terms appear in the series. Unsymmetrical α distributions will be reported on briefly later.

The following assumption as to the form of φ is now made:

$$\varphi(X, Y) = \sum_{n=0}^{\infty} b_n sh(2n+1)Y\cos(2n+1)X \qquad (13)$$

Because of the fact that φ has to satisfy Laplace's equation the dependence upon Y has to be that of a hyperbolic function. The hyperbolic cosine has to be ruled out because of Eq. (4). After substituting Eqs. (13) and (12) into the condition (11) for $Y = -\pi K'/2K$ the following value for the coefficient b_n results:

$$\left.\begin{aligned} b_n &= \frac{1}{2}\frac{Vba_n}{(2n+1)D_n} \\ D_n &= ch(2n+1)\frac{\pi}{2}\frac{K'}{K} + \frac{8}{\pi}\frac{\mathfrak{a}}{m}\frac{GK}{2n+1}\,sh(2n+1)\frac{\pi K'}{2K} \end{aligned}\right\} \qquad (14)$$

Eqs. (13) and (14) contain the complete solution of the problem. The lift on the airfoil itself is obtained from Eq. (13) by putting $Y = \pi K'/2K$. If a sectional lift coefficient c_l is defined by

$$4\rho V\varphi = l = (1/2)\rho V^2 cc_l \qquad (15)$$

then c_l is found to be

$$c_l = 4\mathfrak{a}\sum_{n=0}^{\infty}\frac{a_n}{(2n+1)D_n}\,sh(2n+1)\frac{\pi K'}{2K}\times \cos(2n+1)X \qquad (15')$$

To this formula we add the relation between X and the span coordinate y:

$$y = (b/2)sn(2/\pi)KX \qquad (16)$$

which arises from Eq. (7).

The downwash $w = (\partial\varphi/\partial z)_{z=0}$ can be obtained from Eq. (3) by substituting Eq. (13) into it.

Various Cases of Twist

The coefficient a_n in Eq. (15) remains to be determined. A twist of the form

$$\alpha = \alpha_0 + 3\beta(2y/b)^2 + 5\gamma(2y/b)^4 + \ldots \qquad (17)$$

will be assumed. For untwisted wings only the first term is used; otherwise β and γ may be adjusted to fit a given structural or aerodynamic twist. This expression has to be written as a function of X which can be done with Eq. (16). The left-hand side of Eq. (12) may thus be put into the following form:

$$\alpha\frac{d}{dX}\,sn\,\frac{2}{\pi}KX = \frac{d}{dX}\left[\left(\alpha_0 + \beta\,sn^2\frac{2}{\pi}KX + \gamma\,sn^4\frac{2}{\pi}KX\ldots\right)sn\,\frac{2}{\pi}KX\right]$$

To obtain the coefficients a_n of Eq. (12) one needs therefore the Fourier expansions of the odd powers of the sn function. These are standard developments.[7] The results are

$$\left.\begin{aligned} sn\,\frac{2}{\pi}KX &= \frac{\pi}{Kk}\sum_{n=0}^{\infty}\frac{\sin(2n+1)X}{sh(2n+1)(\pi/2)(K'/K)} \\ sn^3\frac{2}{\pi}KX &= \frac{\pi}{Kk}\sum_{n=0}^{\infty}E_n\frac{\sin(2n+1)X}{sh(2n+1)(\pi/2)(K'/K)} \\ sn^5\frac{2}{\pi}KX &= \frac{\pi}{Kk}\sum_{n=0}^{\infty}F_n\frac{\sin(2n+1)X}{sh(2n+1)(\pi/2)(K'/K)} \end{aligned}\right\} \qquad (18)$$

* Using, for example, Hancock, p. 62, second formula from the bottom.

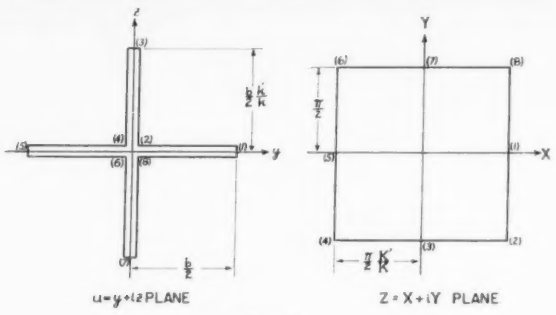

FIG. 2.

$$\left.\begin{aligned} E_n &= (1/2k^2)\left\{1 + k^2 - [(2n+1)(\pi/2K)]^2\right\} \\ F_n &= (1/4k^4)\left\{(1/2)(3 + 2k^2 + 3k^4) - \right. \\ &\quad (5/3)(1+k^2)[(2n+1)(\pi/2K)]^2 + \\ &\quad \left.(1/6)[(2n+1)(\pi/2K)]^4\right\} \end{aligned}\right\} \quad (19)$$

The coefficient a_n is obtained from this, and putting it into Eq. (15) the lift coefficient becomes

$$c_l = \frac{4\pi}{Kk}\,\mathfrak{A}\sum_{n=0}^{\infty}\frac{1}{D_n}(\alpha_0+\beta E_n+\gamma F_n)\cos(2n+1)X \quad (20)$$

The convergence of this series is quite rapid because the denominator D_n of Eq. (14) increases exponentially with n. For untwisted wings β and γ should be put equal to zero.

SECOND TYPE OF CONFORMAL MAPPING

Consider now, in place of Eq. (6) the function

$$u = (b/2k)\,ds\left(\frac{2}{\pi}KZ, k'\right) \quad (21)$$

where $k' = \sqrt{(1-k^2)}$ is the complementary modulus which is also real and between 0 and 1. K is, as before, the elliptic integral belonging to k, not to k'. The function (21) maps the u and Z planes upon one another in a fashion illustrated by Fig. 2. Again corresponding points in the two planes are designated by identical numbers. In the present case the $u = y + iz$ plane must be cut by a cross shaped branch cut which possesses the points $y = \pm b/2$ and $z = \pm(b/2)(k'/k)$ as end points. This is readily seen by two substitutions into Eq. (21).

(a) The two vertical sides of the rectangle correspond to the two horizontal arms of the cross. For when putting $Z = \pm(\pi/2)(K'/K) + iY$ we get*

$$u = \pm(b/2)cn[(2/\pi)KY, k] \quad (22)$$

u is therefore real. In particular for $Y = 0$: $y = b/2$ and $Y = \pm\pi/2$: $y = 0$.

(b) The two horizontal sides of the rectangle map into the vertical sides of the cross. Put $Z = \pm i(\pi/2) + X$ into Eq. (21). The result is†

$$u = \mp i\frac{b}{2}\frac{k'}{k}\,cn\left(\frac{2}{\pi}KX, k'\right)$$

u is imaginary, and the sign shows that the upper side of the rectangle gives the bottom branch of the cross and vice versa. The length of the vertical arms, $(b/2)(k'/k)$ may be greater or less than that of the horizontal arms accordingly as $k' \gtrless k$. It will be seen that only one of these cases, that of $k' \geq k$, has practical interest.

SOLUTION OF THE BOUNDARY VALUE PROBLEM FOR BLUNT WINGS

Boundary condition (3) on the lower side of the wing slit becomes, when transformed into the Z plane with Eq. (21),

$$\left(\frac{\partial\varphi}{\partial X}\right)_{X=\pi K'/2K} - i\frac{8}{mc}\left(\frac{du}{dZ}\right)_{X=\pi K'/2K}\varphi\left(\frac{\pi K'}{2K}, Y\right) = iV\alpha\left(\frac{du}{dZ}\right)_{X=\pi K'/2K} \quad (23)$$

As previously, the chord function $c(y)$ is chosen proportional to du/dZ which now is, using Eq. (22),

$$\left(\frac{du}{dZ}\right)_{X=\pi K'/2K} = -i\frac{b}{2}\frac{d}{dY}cn\left(\frac{2}{\pi}KY, k\right) = i\frac{bK}{\pi}k'\sqrt{1-\left(\frac{2y}{b}\right)^2}\sqrt{1+\frac{k^2}{k'^2}\left(\frac{2y}{b}\right)^2}$$

We therefore choose as chord

$$c(y) = c_0\sqrt{1-\left(\frac{2y}{b}\right)^2}\sqrt{1+\frac{k^2}{k'^2}\left(\frac{2y}{b}\right)^2} \quad (24)$$

which gives a wing blunter than the elliptic wing. Since for $k > k'$ this function has a maximum at a place between the center $y = 0$ and the tips $y = \pm b/2$ we shall only consider moduli k for which

$$0 \leq k \leq 2^{-1/2}$$

The entire family of plan forms—i.e., both the tapered ones given by Eq. (9′) and the blunt ones given by Eq. (24)—are shown for the arbitrarily selected aspect ratio of 8 in Fig. 3.

We also note that for S, $\mathfrak{A}$, and $\bar{c}$ we have now

$$S = bc_0H(k)/k'; \quad \mathfrak{A} = bk'/[H(k)c_0];$$

$$\bar{c} = H(k)c_0/k' \quad (25)$$

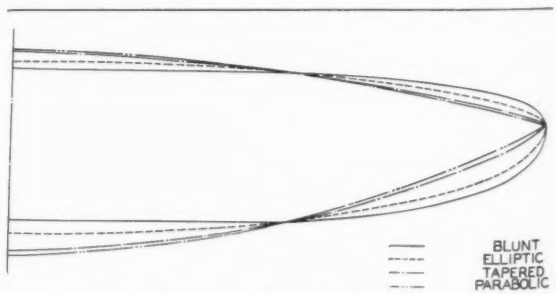

FIG. 3. Plan forms of $\mathfrak{A} = 8$ for various K values.

* Hancock, p. 33, second set. Primed and unprimed quantities must be interchanged.

† *Ibid.*, p. 33, last set of formulas on page.

where $H(k)$ is another standard elliptic integral

$$H(k) = (1/3k^2)\,[(1 - k^2)K - (1 - 2k^2)E]$$

For the limiting value $k = 2^{-1/2}$ which interests us most $K(k)$ has the numerical value 0.61802. The wing shape for this case is the full line in Fig. 3.

In accordance with the fact that now the condition (23) has to be satisfied on the two vertical boundaries of the rectangle, the following hypothesis as to the form of φ is made:

$$\varphi = \sum_{n=0}^{\infty} b_n' ch(2n + 1)X \sin (2n + 1)Y \qquad (26)$$

From then on the calculation runs quite analogously to that of Eq. (5). The final formula for the section lift coefficient, in case of a twist given by Eq. (17) is

$$c_l = \frac{4\pi}{Kk}\,\mathfrak{a} \sum_{n=0}^{\infty} \frac{1}{D_n'}\,(\alpha_0 + \beta E_n' + \gamma F_n') \times \sin (2n + 1)Y \qquad (27)$$

The relation between Y and the span coordinate y is

$$y = \frac{b}{2}\, cn\left(\frac{2}{\pi} KY, k\right) \qquad (28)$$

The following abbreviations, analogous to Eqs. (14) and (19), are employed:*

$$\left.\begin{aligned} D_n' &= sh(2n + 1)\frac{\pi}{2}\frac{K'}{K} + \frac{8}{\pi}\frac{\mathfrak{a}}{m}\frac{HK}{2n + 1}\, ch(2n + 1)\frac{\pi}{2}\frac{K'}{K} \\ E_n' &= \frac{1}{2k^2}\left\{-1 + 2k^2 + \left[(2n + 1)\frac{\pi}{2K}\right]^2\right\} \\ F_n' &= \frac{1}{4k^4}\left\{\frac{1}{2}(3 - 8k^2 + 8k^4) - \frac{5}{3}(1 - 2k^2) \times \left[(2n + 1)\frac{\pi}{2K}\right]^2 + \frac{1}{6}\left[(2n + 1)\frac{\pi}{2K}\right]^4\right\} \end{aligned}\right\} \qquad (29)$$

The convergence is as rapid as that of Eq. (20). For untwisted wings β and γ vanish. For twisted wings the coefficients E_n' and F_n' simplify somewhat if one restricts oneself to the interesting limiting case $k = 2^{-1/2}$.

Remarks on Discontinuities of the Velocity Potential φ in the Plane of the Original Variables y and z

As stated in Eq. (4) it is desired that φ have a discontinuity along the y axis when y is between $\pm b/2$. (The normal derivative, however, should be continuous.) It is immediately seen that our φ solutions (13) and (26) behave in this fashion. But the conformal representations (6) and (21) introduce, as Figs. 1 and 2 show, further lines of ramification, namely, either a branch cut from $\pm b/2$ to $\pm b/2k$ or, in the, blunt case, from ± 0 to $\pm(b/2)\,(k'/k)$. It should be verified that on these "unphysical" cuts the potential φ or its derivatives do not suffer discontinuities.

For tapered wings, Fig. 1 indicates that opposite points on, say, the cut between $b/2$ and $b/2k$ correspond to points whose Z is $\pi/2 \pm i\gamma$. Eq. (13) shows that for such values φ vanishes. Turning to the derivative we see that, by virtue of the Cauchy-Riemann equations

$$\left(\frac{\partial\varphi}{\partial X}\right)\left(\frac{\pi}{2}, Y\right) = -\left(\frac{\partial\varphi}{\partial z}\right)(y, 0)\cdot\left(\frac{\partial y}{\partial Y}\right)\left(\frac{\pi}{2}, Y\right)$$

Since the left-hand side is odd in Y, and the second member of the right is, by virtue of Eq. (7′), likewise odd in Y, the first member must therefore be even in Y—i.e., continuous for points on opposite sides of the cut $b/2 \le y \le b/2k$. Similarly one proves, using both Laplace's equation and the Cauchy-Riemann equations that all even derivatives of φ with respect to z vanish on the cut, while all odd ones are equal for opposite points. The proof for the vertical cuts of the "blunt" mapping is analogous.

Thus it is seen that, although the mapping possesses branch cuts in addition to the physical one $-(b/2) \le y \le (b/2)$, the velocity potential $\varphi(y, z)$ has the required discontinuity only at the latter cross cut while behaving perfectly continuously at the former ones.

Further Rigorous Calculations

For the sake of completeness, two extensions of the calculations presented in the previous sections should be pointed out.

(1) The first of these is concerned with the limiting case of extreme taper when the plan form is given by

$$c(y) = c_0[1 - (2y/b)^2]$$

This case is treated in detail in Section 8 of reference 1. It is of some interest, for it contains the rigorous solution of the lift problem for a wing whose tips are not rounded off, but rather pointed. The velocity potential φ and the lift coefficient now appear in the form of series proceeding according to the roots σ_n of the transcendental equation†

$$\sigma_n \cos \sigma_n + a \sin \sigma_n = 0; \qquad a = (4\pi/3)\,(\mathfrak{a}/m)$$

The result for the lift coefficient c_l of an untwisted wing turns out to be

$$c_l = 8\alpha\mathfrak{a} \sum_{n=1}^{\infty} (-1)^{n+1} \frac{\sigma_n(a^2 + \sigma_n^2)^{1/2}}{a(a + 1) + \sigma_n^2}\left(\frac{1 - 2y/b}{1 + 2y/b}\right)^{\sigma_n/\pi}$$

The roots σ_n can be obtained graphically with ease.

(2) In the doctoral dissertation of the junior author[5] still another case of twist is calculated, namely, one where the angle of attack is a linear function of span.

(3) Compact expressions for overall quantities, such as total lift, total drag, and rolling moment, have been

* The coefficients E_n' and F_n' are essentially the expansion coefficients in the Fourier series for the cube and the fifth power of cnu.

† The above a value should be substituted for Eq. (51″), p. 244 of reference 1.

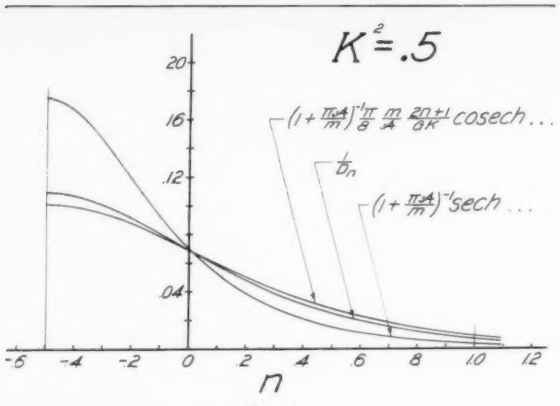

FIG. 4.

obtained, and their dependence upon taper, aspect ratio and degree of twist calculated. For this too, see reference 8.

(4) Tables and graphs of the dependence of the sectional lift coefficients upon span may also be found there.

AN APPROXIMATION LEADING TO SCHRENK'S FORMULA

As stated in the introduction, the rigorous formulas obtained will be approximated in such a fashion that Schrenk's rule results. For the sake of briefness this process will be explained using only the formulas of the tapered wing. The formulas for the blunt wing can be dealt with in an analogous fashion. We shall also restrict ourselves to untwisted wings, putting β and γ in Eq. (20) equal to zero.

The convergence of the series (20) depends essentially upon the denominator D_n which, from its definition (14), is seen to consist of two terms, both rapidly increasing functions of $2n + 1$. We propose to replace the denominator D_n of Eq. (20) by two simpler expressions. We shall

(a) Replace $ch(2n + 1)\ (\pi/2)\ (K'/K)$ by $\lambda(2n + 1)^{-1} sh(2n + 1)\ (\pi/2)\ (K'/K)$.

(b) Replace $(2n + 1)sh(2n + 1)\ (\pi/2)\ (K'/K)$ by $\lambda^{-1}\ ch\ (2n + 1)\ (\pi/2)(K'/K)$.

For small values of n this is a perfectly plausible approximation; however, for large values of n, while both expressions increase exponentially they deviate from one another more and more. As far as large n values go, it would seem more plausible simply to replace the *ch* by the *sh* function, and vice versa. If, nevertheless, the above method of approximation is chosen, it is in view of the fact that terms with small n contribute overwhelmingly more in Eq. (20). The numerical constant λ will be determined later so as to give the best approximation in the mean.

When replacing, according to (a), the rigorous expression for the lift per unit span l is changed into an approximation which will be denoted by l_1. This becomes, according to Eqs. (15) and (20),

$$l_1 = \frac{2\pi}{Kk} \frac{\alpha_0 \rho V^2 b}{\lambda + (8/\pi)\ (\mathfrak{a}/m)GK} \sum_{n=0}^{\infty} (2n + 1) \times \frac{\cos\ (2n + 1)X}{sh(2n + 1)\ (\pi/2)\ (K'/K)} \tag{30}$$

This is, according to the first formula (18), proportional to

$$cn(2/\pi)KX\ dn(2/\pi)KX$$

and therefore, according to Eqs. (9), (9′) and (16),

$$l_1 = \frac{4K}{\pi} \frac{\alpha_0 \rho V^2 b}{\lambda + (8/\pi)\ (\mathfrak{a}/m)GK} \times \sqrt{[1 - (2y/b)^2]\left[1 - k^2\left(\frac{2y}{b}\right)^2\right]} \tag{30′}$$

On the other hand, replacing according to (b) and calling the resulting approximate lift l_2,

$$l_2 = \frac{2\pi}{Kk} \frac{\alpha_0 \rho V^2 b \lambda}{\lambda + (8/\pi)(\mathfrak{a}/m)GK} \times \sum_{n=0}^{\infty} \frac{\cos\ (2n + 1)X}{ch\ (2n + 1)\ (\pi/2)\ (K'/K)} \tag{31}$$

The series is the well known expansion[9] of $cn(2/\pi)KX$. Therefore,

$$l_2 = \frac{2\lambda \alpha_0 \rho V^2 b}{\lambda + (8/\pi)\ (\mathfrak{a}/m)GK} \sqrt{1 - \left(\frac{2y}{b}\right)^2} \tag{31′}$$

To fix λ most advantageously, it seems reasonable to calculate the total lift by integrating Eqs. (30) and (31) along the span, and to equate the obtained expressions. We get first from Eq. (30)

$$L_1 = \frac{4K}{\pi} \frac{\alpha_0\ \rho V^2 b}{\lambda + (8/\pi)\ (\mathfrak{a}/m)GK} bG$$

where G is the elliptic integral introduced in Eq. (10). Then from Eq. (31)

$$L_2 = \frac{2\lambda \alpha_0 \rho V^2 b}{\lambda + (8/\pi)\ (\mathfrak{a}/m)GK} b \frac{\pi}{4}$$

Equating these two expressions we obtain for λ,

$$\lambda = 8KG/\pi^2 \tag{32}$$

while l_1 and l_2 assume the following form:

$$\left.\begin{aligned} l_1 &= \frac{1}{2} \rho V^2 \frac{\pi \alpha_0 b}{1 + \pi \mathfrak{a}/m} \frac{c(y)}{c} \\ l_2 &= \frac{1}{2} \rho V^2 \frac{\pi \alpha_0 b}{1 + \pi \mathfrak{a}/m} \frac{\sqrt{1 - (2y/b)^2}}{\pi/4} \end{aligned}\right\} \tag{33}$$

If we now take as a less biased approximation the arithmetic mean of the two,

$$l_S = (1/2)\ (l_1 + l_2) \tag{34}$$

we obtain exactly Schrenk's formula for untwisted wings.* For blunt wings the same formula—but with

* See first formula on p. 3 of Schrenk's paper quoted in the introduction. A correction constant K, used by him to adjust the dependence upon aspect ratio turns out to be zero in our case when λ is fixed as in Eq. (32).

the chord of Eq. (24)—results, after replacements corresponding to (a) and (b) have been made in the denominator D_n' of Eq. (29).

In Figs. 4 and 5 the coefficients $1/D_n$ of the exact solution together with the Fourier coefficients of the series (30), (31) for l_1 and l_2 are shown for two values of the modulus k.

Generalization of the Process Employed Above to Arbitrary Plan Forms and Twists

When looking at the rigorous solution (19) we see that its coefficients E_n, F_n, and D_n owe their appearance to different causes: E_n is due to the quadratic twist, F_n to the quartic twist, while D_n arises from the fundamental boundary condition (3). It is this latter coefficient which was replaced either by (a constant times) its second term or by (a constant times) its first term. But since the first term of D_n is due to the first term of the boundary condition (3), and the second term of D_n to the second term of Eq. (3), it may be said also that in the preceding paragraph we have replaced the rigorous boundary value problem (2), (3), and (4) by the following problems:

(a) The boundary value problem of the first kind with the boundary condition for $-b/2 \leq y \leq b/2$

$$\varphi_1(y, 0) = \frac{V\alpha m}{8(1+\lambda)}\, c(y)$$

(b) The boundary value problem of the second kind with the condition for $-b/2 \leq y \leq b/2$

$$\left(\frac{\partial \varphi_2}{\partial z}\right)_{z=0} = -\frac{\lambda V \alpha}{1+\lambda}$$

In addition, both φ_1 and φ_2 have to satisfy Eq. (4) and have to be solutions of Laplace's equation (2). The constant is fixed by the requirement that the integrals along the span of φ_1 and of φ_2 agree. The Schrenk approximation is the arithmetic mean of φ_1 and φ_2.

The above problems may readily be solved for any chord or angle of attack distribution. But inasmuch as we are interested only in lift—i.e., in $\varphi\ (y, 0)$—the value of $\varphi_1(y, 0)$ is already fixed by the above condition (a). Problem (b) is seen to be independent of the plan form and can therefore be solved as if an elliptic wing were being studied.

We shall illustrate this for the case of an untwisted wing by rederiving—for an arbitrary plan form—the two approximate lifts (33) whose arithmetic mean Schrenk's formula (34) employs. l_1 is taken immediately from (a) and gives

$$l_1 = \frac{1}{2}\rho V^2 \frac{\alpha m}{1+\lambda}\, c(y) \tag{35}$$

and a total lift

$$L_1 = \frac{1}{2}\rho V^2 \frac{\alpha m}{1+\lambda} S$$

φ_2 and l_2 we anticipate to be elliptic since the downwash derivative is constant. The conformal transformation* $u = (b/2)ch\zeta$ maps the exterior of the wing slit into the semi-infinite strip bounded by the points ∞, 0, $2\pi i$, $\infty + 2\pi i$. The two sides of the cut from $-b/2$ to $b/2$ become the imaginary axis from 0 to $2\pi i$. Boundary condition (b) becomes, in terms of ξ and η ($\zeta = \xi + i\eta$),

$$\left(\frac{\partial \varphi_2}{\partial \xi}\right)_{\xi=0} = -\frac{V\alpha B\lambda}{2(1+\lambda)} \sin \eta$$

The solution of this boundary value problem is

$$\varphi_2 = \frac{V\alpha b\lambda}{2(1+\lambda)} \sin \eta e^{-\xi}$$

which gives as lift

$$l_2 = \frac{2\rho V^2 \alpha b\lambda}{1+\lambda}\sqrt{1-\left(\frac{2y}{b}\right)^2} \tag{36}$$

and as total lift

$$L_2 = \frac{1}{2}\rho V^2 \frac{\pi a b^2 \lambda}{1+\lambda}$$

Equating the L we find

$$\lambda = (m/\pi)\ (S/b^2) = m/\pi a$$

After substituting this value for λ into Eqs. (35), (36), these l values are seen to agree with Eq. (33).

A last remark on discontinuously varying α distributions, which occur in the case of flaps or ailerons, may be added. The above cited papers† have several figures which demonstrate that Schrenk's original recipe gives rise to discontinuous lift distributions. These being unreasonable, more or less arbitrary methods are given to "fair out" the discontinuities. Let us see what our approximations (a) and (b) give instead. The function φ_1 being proportional to α is also discontinuous. But φ_2 will be perfectly continuous even though its normal derivative may jump. The arithmetic mean of φ_1 and φ_2 will thus show only a discontinuity of half the amount.

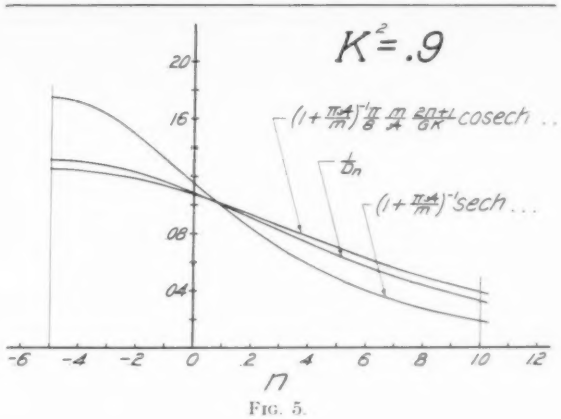

Fig. 5.

* See reference 1, Section 2, p. 234.

† See reference 2.

REFERENCES

[1] Laporte, O., *Rigorous Solutions for the Spanwise Lift Distribution of a Certain Class of Airfoils*, Quarterly of Applied Mathematics, Vol. 2, No. 3, pp. 232–250, October, 1944.

[2] Schrenk, O., *A Simple Approximation Method for Obtaining the Spanwise Lift Distribution, NACA* TM 948, 1940. See also Engineering Section Rep. No. 28, Civil Aeronautics Administration, Department of Commerce, August 1, 1941.

[3] Trefftz, E., Zeitschr. f. Angew. Math. und Mech., Vol. 1, pp. 206–209, 1921.

[4] This is the notation of Mises and Friedrichs in their *Fluid Dynamics*, Brown University lecture notes, 1941. On p. 108 and following a presentation of Trefftz' paper may be found.

[5] The most convenient tables of elliptic functions and elliptic integrals are by L. M. Milne-Thomson, Published 1931 by Springer in Berlin. The usual abridged notation for elliptic functions is adhered to here, according to which $1/sn = ns$, $1/dn = nd$, $cn/dn = cd$, $dn/cn = dc$, etc. If an elliptic function is followed by only one argument the modulus K is understood.

[6] For the very simple transformations of elliptic functions used here, see for instance, Whittaker and Watson, *Modern Analysis*, pp. 493–498; or Hancock, *Elliptic Integrals*, p. 33.

[7] In Whittaker and Watson, 4th Ed., p. 510, the general method for obtaining any of these series is described. The series for sn may be found there, while that for sn^3 is on p. 535, example 57. The series for sn^5 with rules for obtaining even higher powers are given in C. G. J. Jacobi's *Collected Works*, Vol. I, pp. 170–186, Berlin, 1881.

[8] Yoshihara, Hideo, *Rigorous Solutions of Prandtl's Integral Equation*, Thesis, 1945, University of Michigan.

[9] See, for instance, Whittaker and Watson's *Modern Analysis*, 2nd Ed., p. 504, 1915. A troublesome misprint has crept into the 3d, 4th and American editions published, respectively, 1920, 1927, and 1943. On p. 511, the second formula from the top of the page, representing the Fourier series for cnu, should have the exponent $2n + 1$ in the denominator instead of $2n - 1$.

Gas Dynamic Behavior of Real Gases

(*Continued from page 774*)

[8] *Handbuch der Experimentalphysik*, Vol. 8, Part 2, pp. 224–228; Leipzig, 1929.

[9] Maron, S. H., and Turnbull, D., *Calculating Beattie-Bridgeman Constant from Critical Data*, Ind. & Eng. Chem. Vol. 33, No. 12, pp. 1536–1537, 1941.

[10] Kelly, K. K., *High Temperature Specific Heat Equations for Inorganic Substance*, U.S. Bur. Mines, Bulletin 371, 1934.

[11] Schmidt, E., *"Laval Druckverhaltnis" statt "Kritische Druckverhaltnis"*, Forsch. auf dem Geb. des Ing. Wes., Vol. 16, No. 5, p. 154, 1949.

[12] Buffington, R. M., and Gilkey, W. K., *The Thermodynamic Properties of Dichlorodifluoromethane, A New Refrigerant*, Ind. & Eng. Chem., Vol. 23, No. 3, pp. 254–256, 1931.

[13] Bradley, C. A., Jr., *The Smekal-Raman Spectra of $SiHCl_3$, $CHFCl_2$ and CF_2Cl_2*, Phy. Rev., Vol. 40, p. 908, 1932.

[14] Plyler, E. K., and Benedict, W. S., *Infrared Spectra of Eighteen Halogen-Substituted Methane*, Jour. of Res. of NBS, Vol. 47, No. 3, pp. 202–220, 1951.

[15] Tao, L. N., *Gas Dynamic Behavior of Real Gases*, Ph.D. Thesis in Mechanical Engineering, University of Illinois, 1953.

[16] Kantrowitz, A., *Effects of Heat-Capacity Lag in Gas Dynamics*, NACA-APR 4A22, 1944.

[17] Bethe, H. E., and Teller, E., *Deviations from Thermal Equilibrium in Shock Waves*, Aberdeen Proving Ground, Aberdeen, Md., Ballistic Research Laboratory, Rep. No. X-117, 1945.

JOURNAL EXPANSION PLANS

Beginning with the January, 1956, issue, the contents of the JOURNAL OF THE AERONAUTICAL SCIENCES will be expanded approximately 25 per cent. Subscription rates will be:

IAS Members—$5.00 per year
Nonmember Subscriptions—$15.00 per year
($1.00 additional for foreign subscriptions)

Readers' Forum

BRIEF REPORTS of investigations in the aeronautical sciences and discussions of papers published in the JOURNAL are presented in this special department. Publication is completed as soon as possible after receipt of the material. The Editorial Committee does not hold itself responsible for the opinions expressed by the correspondents.

Remarks on the Velocity of Sound

Max M. Munk
The Catholic University of America, Department of Aeronautical Engineering, Washington, D.C.
May 15, 1955

THERE IS A NEED for a wider spread understanding of the precise meaning and definition of the velocity of sound. This is a fundamental quantity in the theory of gas dynamics. Whoever wants to understand the theory has first to understand the velocity of sound.

We learn to understand and to compute the velocity of sound by scrutinizing how it is first introduced into the equations. The initial and most basic equations of gas motion do not contain the velocity of sound. It is introduced as a later step to get the theory under better control.

The theory deals with the motion of a continuous fluid in three dimensions, not necessarily a steady motion. Shear forces are assumed to be absent. This is the only limiting assumption. Viscosity is excluded only as far as it would introduce shear forces. Heat conduction and addition or removal of heat are not excluded at all. That by itself does not lead to shear. The gas is not necessarily perfect, not barotropic, not even homogeneous.

The broad class of shearless fluid motions is governed by the system of equations

$$\left.\begin{aligned} \dot{v} + (\text{grad } p)/\rho &= 0 \\ \dot{\rho} + \rho \,\text{div}\, v &= 0 \end{aligned}\right\} \tag{1}$$

The first of these two equations is a vector equation and is equivalent to three ordinary equations. It describes the dynamic relation between the velocity v, the pressure p, and the density ρ. The second equation expresses the condition of continuity.

Eqs. (1) contain five dependent variables. The system (1) is incomplete. It is necessary to introduce a combination of the dependent variables as a new independent variable. It is expedient and customary to choose the velocity of sound for that purpose.

In Eqs. (1) the dot represents time differentiation with Lagrangian independent variables. That is to say it designates the rate of change of the quantity in question with reference to each separate fluid particle preserving its identity by itself. Such rate of change has a much more vivid physical significance than items merely describing the variation of the pressure field or density field.

The square of the velocity of sound, c^2, is introduced by way of eliminating the derivative of the density, by the equation

$$\rho = p/c^2 \tag{2}$$

The quantity c^2 relates accordingly to one specific gas particle and its doing. It does not relate at all to the adjacent particles or to the field distributions and their variations. The expression $1/c^2$ is a kind of de facto specific volumetric elasticity modulus of the particle, a kind of effective hardness of the gas. It is the intensity by which it appears to resist the change of its volume under the action of the pressure, as if all volume changes were attributable to the pressure and none to the change of temperature. That is to say, the pressure changes are made responsible for the temperature changes and its effects too, whether they are or not.

It is often stated in the literature.

$$c^2 = dp/d\rho \tag{3}$$

Eq. (3) is consistent with Eq. (2) provided the density throughout the flow is a function of the pressure only. If it were not the ordinary differential quotient in Eq. (3) would not even have any meaning. If the pressure and the density vary independently of each other, only the partial derivative $\partial p/\partial \rho$ would come in the question. That partial derivative has not a unique value for any point or particle. In a steady flow the partial derivative $\partial p/\partial \rho$ depends on the direction of the line along which in succession the values of the pressure and of the density are studied, and their changes compared with each other. No such lack of uniqueness attends the velocity of sound. Only one of the many values of $\partial \rho/\partial \rho$ can therefore be equal to the square of the velocity of sound. It is computed in a steady flow in the direction of the stream line, for the same particle occupies then, in succession, all points of that line and of that line only.

Acoustical waves are assumed to be associated with isentropic expansions and contractions. Therefore the square of the acoustical velocity of sound is equal to the thermodynamic partial derivative $\partial p/\partial \rho$ for constant entropy. The velocity of sound appearing in the equations of the gas motion, including the forms of these equations called "characteristic" is not necessarily equal to the isentropic derivative. "Velocity of sound" is then somewhat of a misnomer. Superposing acoustic waves to a gas motion changes the flow and its gas properties, and may change a steady flow into an unsteady one. That would change the magnitude of the applicable velocity of sound, too.

An incompressible fluid having a density variable throughout space exhibits many different magnitudes of $\partial p/\partial \rho$ but its velocity of sound is, of course, infinite. That illustrates the lack of identity between c^2 and $\partial p/\partial \rho$.

Strength Under Combined Tension and Bending in the Plastic Range

J. M. Frankland and R. E. Roach
Staff Assistant, Structures Technical Group, and Lead Structures Design Engineer, Respectively, Chance Vought Aircraft, Incorporated, Dallas, Tex.
May 18, 1955

ANTHONY J. BARRETT has recently published[1] in the Readers' Forum some interesting comments on our paper[2] on plastic effects under combined tension and bending. He points out, quite correctly, that the effects of deformation of cross section are small and could well have been neglected. This circum-

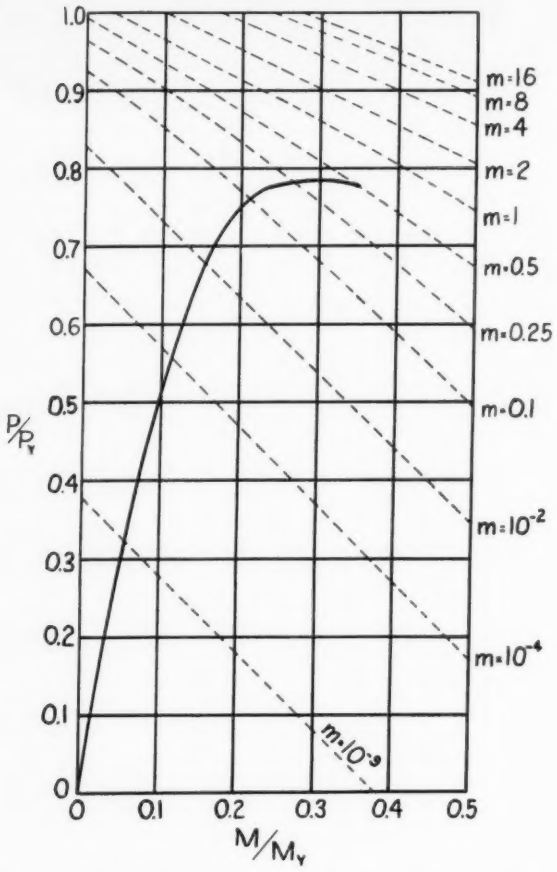

FIG. 1. Loading history of a curved bar under compression loading.

stance, however, was not self-evident and called for confirmation. A statement regarding the negligible effects of change in section shape was inadvertently omitted from the published paper.

We are particularly glad that Barrett has brought up this point, since otherwise it might appear that the published curves apply only to a material with the stated value of yield strain. The complications due to section deformation can be eliminated from the expressions in the original paper by setting $\epsilon_Y = 0$ in Eqs. (3) through (8), (12), (16), and (17).

Regarding the use of apparent stress rather than true stress, there seems to us no advantage to the use of apparent stress. This choice enters only into the determination of n, the constant characterizing the shape of the stress-strain curve. There is little work required to convert the conventional stress-strain curve to the true stress-strain curve for the values of strain which are of interest, since these are less than the strain required to reach maximum load in the tensile test.

Doubts were expressed in the original paper regarding the applicability of our results to the calculation of curved bars under axial compression in view of the stress reversals which would take place. Barrett, however, points out that this is too pessimistic a conclusion for a material which can be considered elastic up to three-quarters of the yield strength, which is true of most of the high-strength alloys in use today. He proposes that our methods apply for eccentricities larger than one-fortieth of the beam depth. He justifies this by consideration of extreme fiber stresses.

It is our belief, however, that the strain history of each point in the cross section must be considered, since stress reversals may take place in the interior of the beam as well as at the surface. Only in this way can one be certain that variations in conditions, such as different shapes of the stress-strain curve, and different redundant combinations of axial load and bending, such as eccentric loading of an initially straight member, have not made the calculation invalid.

Considering the case of a curved bar under axial compression with an initial eccentricity equal to one-fortieth of the beam depth (Barrett's approximate limiting case in compression) and assuming the same proportions used in the example in our original paper,[2] except for the eccentricity,

$$l = 16.2\,h$$

$$a_0 = h/20$$

and $\epsilon_Y = 6.3 \times 10^{-3}$

For compression loading, Eq. (23)[2] becomes

$$\frac{M}{M_Y} = \left(\frac{3a_0}{h} + \frac{3\epsilon_Y l^2}{\pi^2 h^2}\,\kappa\right)\frac{P}{P_Y}$$

For the specific example this reduces to

$$M/M_Y = (0.15 + 0.5\,\kappa)\,(P/P_Y)$$

The resulting load history through maximum load for a material with a stress-strain curve characterized by $n = 21$ is shown in Fig. 1.

From the intersection of this loading curve with the lines of constant elongation, m, the strain in the most highly stressed fiber, e_1, can be determined at a number of load levels. The values of κ can be obtained either by interpolation between κ curves or by calculation from the slope of the line connecting the origin and the intersection of the loading curve and the appropriate m-line. That is,

$$\kappa = 2\left(\frac{M/M_Y}{P/P_Y} - 0.15\right)$$

From the value of κ, the strain in the least strained fiber is, from Eq. (20)[2]

$$e_2 = e_1 - 2\kappa$$

The strains over the depth for the example case are shown in Fig. 2 for several values of extreme fiber strain.

Accepting Barrett's suggestion that strain reversals below three quarters of the yield strength take place elastically, and therefore reversibly, it will be seen that up through maximum load all strain reversals occur in the elastic core of the section. In this particular case, then, the method of our paper is applicable

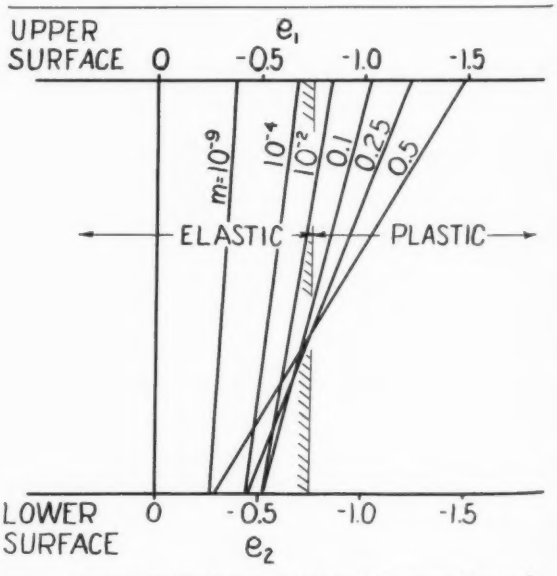

FIG. 2. Strain distributions over the depth of a curved bar under compression loading.

TABLE 1

Values of Stress and Total Strain at Which the Plastic Strain is one per cent of the Elastic Component of Yield Strain

n	7	11	15	21
σ/σ_Y	0.585	0.711	0.778	0.836

in compression certainly down to an eccentricity of one-fortieth the beam depth, in confirmation of Barrett's remarks.

The level of stress below which stress reversals are permitted should more reasonably be stated in terms of an acceptable plastic strain. With this criterion, the value of allowable stress (or strain) for stress reversals will depend on n. If it is assumed that a reversal of plastic strain no greater than one per cent of the elastic component of the yield strain should occur, then a value of the plastic component of strain, m, equal to 0.01 would define the limiting stress. The limiting values of stress for this assumption are shown in Table 1 for several shapes of the stress strain curve.

REFERENCES

[1] Barrett, Anthony J., *Beam Strength and Curvature Under Combined Tension and Bending in the Plastic Range*, Journal of the Aeronautical Sciences, Readers' Forum, Vol. 22, No. 1, pp. 71–72, January, 1955.

[2] Frankland, J. M., and Roach, R. E., *Strength Under Combined Tension and Bending in the Plastic Range*, Journal of the Aeronautical Sciences, Vol. 21, No. 7, pp. 449–453, July, 1954.

Some Comments on "A Theoretical and Experimental Study of Shock Tube Flows"*

Darshan S. Dosanjh
Research Associate, Institute for Fluid Dynamics and Applied Mathematics, University of Maryland, College Park, Md.

May 21, 1955

RECENTLY GLASS AND PATTERSON[1] have published some position vs. time schlieren records of the interaction of a shock wave with screens. These were recorded by the technique of a rotating drum camera in conjunction with a wave interaction tube. They observed that after the interaction, the wave system consists of a reflected and transmitted shock wave separated by a contact surface and a vortex (see plates 18–19 in reference 1).

The author[2, 3, 4] also conducted, independently, some similar experiments in a shock tube to study the various aspects of the interaction of traveling shock waves with grids (perforated plates, Fig. 1). A combination of optical (shadowgraphic) and hot wire techniques was used for experimental recording. The wave model for shock wave – grid interaction is reproduced in Fig. 2. The grids were mounted between two glass sections about 16 ft. downstream from the diaphragm location. By this arrangement, it was possible to simultaneously record the reflected shock wave upstream of the grid, as well as the transmitted shock wave, turbulent contact surface and any allied phenomena downstream of the grid. (For details see references 2 and 3.)

The presence of a vortex as reported by Glass and Patterson[1] is not substantiated by our experimental observations. A large number of shadowgraphs of the shock wave – grid interaction were taken systematically for various incident shock strengths at controlled delay time settings. No vortex, of the nature reported in reference 1, was observed. What was, however, consistently observed was that for incident shock waves of strength $S \geq 3.0$ where S = the ratio of the pressure behind the incident shock wave to the pressure ahead of the incident shock wave, there emerged, following the transmitted shock wave and turbulent contact surface, an auxiliary shock pattern out of the grid (Fig. 3a). Notice that the reflected shock wave and this auxiliary shock pattern are similarly faced and the transmitted shock wave is oppositely faced to them.

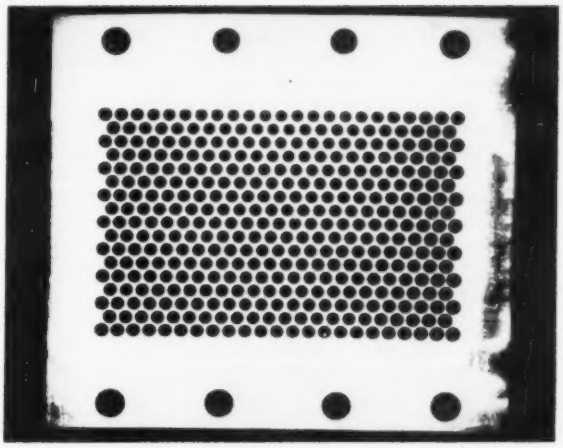

FIG. 1. The grid used for the investigation of shock wave-grid interaction. 1/4-in. thick perforated steel plate with reamed holes of 0.25 in. diameter. Solidity ratio $s = 0.25$.

A controlled set of shadowgraphs, with longer time delays, established that this auxiliary shock front was being washed downstream at very slow speeds (about 1/2 in. in 1.3 millisec., Fig. 3b. The upstream face of the grid corresponds to zero delay in both of the shadowgraphs reproduced here). It is felt that if the flow field approaching, and out of, the grid was really steady then this auxiliary shock front will stabilize itself, depending upon the effective grid solidity, at some suitable distance downstream of the grid.

The author believes that it is this auxiliary shock front which Glass and Patterson[1] have identified as a vortex in their position vs. time schlierens. The general agreement between their other results and ours[2, 3] and also a clear similarity of behavior of this auxiliary shock phenomena, viz. its appearance only at comparatively high incident shock strengths and its slow speed of advance, strengthens our belief that the said authors[1] were handicapped in analysis of this aspect of the experimental data by their experimental technique. A step-by-step record of the time history and development of the interaction by shadowgraphs happens to be comparatively more revealing in this present case.

Behind the traveling reflected and transmitted shock waves, the flow field (in regions 3 to 5, Fig. 2) is riddled with diffracted shocklets. There are rarefaction waves and also an intensely

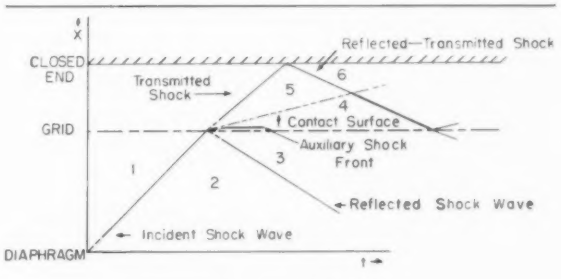

WAVE MODEL FOR SHOCK WAVE– GRID INTERACTION

FIG. 2.

* The experimental work on which this article is based[2, 3] was carried out by the author during 1953 at the Department of Aeronautics, Johns Hopkins University, Baltimore, Maryland. The work was sponsored by the United States Air Force, under Contract AF18(600)-757.

The author gratefully acknowledges the helpful discussions with Francis H. Clauser. Richard Swartley's help with the experimental work is appreciated.

turbulent contact surface in the region 4. At higher incident shock strengths the auxiliary shock fronts appear in region 4. This makes any complete theoretical analysis difficult to attempt. However, to extract as much information and/or inferences from the experimental data as possible, some simplifying assumptions have been resorted to.

It is assumed that the reflected shock front very close to the upstream side of the grid becomes normal and plane—i.e., parallel to the grid (not too far from reality, see Fig. 3a and also reference 3)—and that the flow in the regions 2 and 3 is steady, one-dimensional and isentropic. Extending the conventional plane normal shock wave analysis to the reflected shock wave one can then get

$$M_3 = f(U_{SR}, U_s, \ldots) \qquad (1)$$

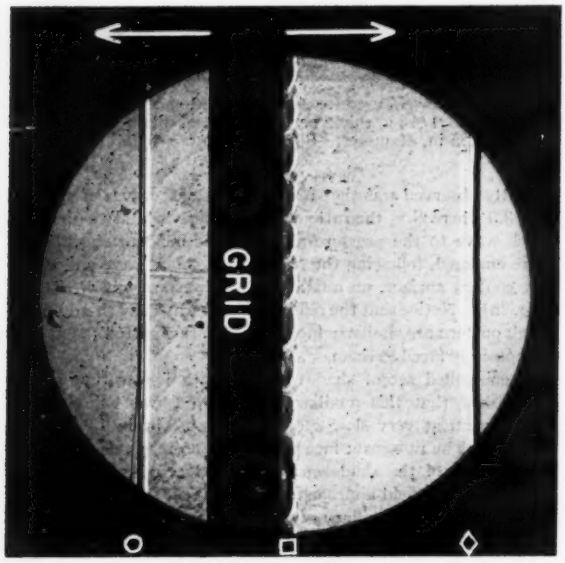

FIG. 3a. Emergence of the auxiliary shock front through the grid. ○ reflected shock wave; □ auxiliary shock front; ◇ transmitted shock wave. $S = 3.2$. Delay time = 65×10^{-6} sec.

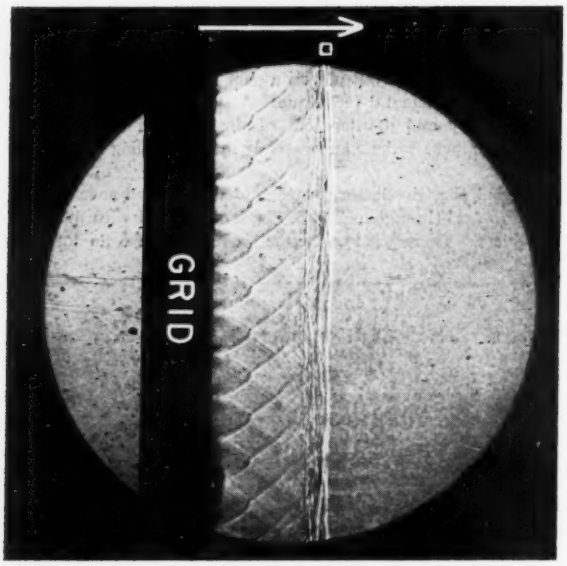

FIG. 3b. Emergence of the auxiliary shock front through the grid. □ auxiliary shock front. $S = 3.2$. Delay time = $1{,}375 \times 10^{-6}$ sec.

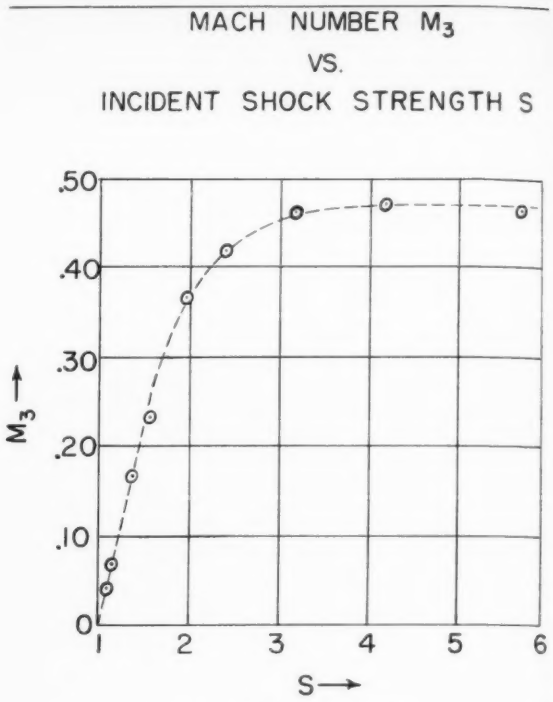

FIG. 4. ⊙ Calculated points.

where $M_3 = u_3/a_3$ = the Mach Number of the flow approaching the grid in region 3 (called M_3 in reference 1). u_3 and a_3 represent respectively the flow velocity and the sound speed in region 3. U_s = speed of the incident shock front. U_{SR} = speed of the reflected shock front traveling upstream against the drift flow behind the incident shock wave.

From the experimentally measured ambient conditions and shock speeds U_s and U_{SR}, M_3 can be calculated. It was observed[2] that, for the grid used, M_3 reaches an upper limit for $S = 3.2$ and stays fairly constant for values of S higher than that (Fig. 4). Glass and Patterson[1] have also arrived at a similar conclusion.

It is important to point out that the auxiliary shock fronts first appear only when the incident shock strength S is high enough (depends on effective solidity of the grid). Since it is observed that corresponding to these high values of S the Mach Number M_3 assumes a constant value, obviously the grid is choked.[5] The grid holes act like crude nozzles. At their exit the flow expands and develops a shock front similar to a terminal shock in a supersonic tunnel. The associated diamond-type wave pattern (see Fig. 3b) is similar in nature to the one observed, due to over-expansion, in the flow of a supersonic jet at the exit of a nozzle.

Our experimental observation of this auxiliary shock front downstream of the grid is very well substantiated by the shadowgraphs of a supersonic "Swiss Cheese" projectile fired on a ballistic range.[6]

Let the solidity ratio of the grid be defined as

$$s = 1 - (A_0/A)$$

where A_0 is the projected open area of the grid exposed to the flow (in the present setup the grid is mounted perpendicular to the flow direction), and A is the projected area of the grid boundary exposed to the flow and is equivalent to the cross-sectional area of the shock tube.

The solidity ratio s is essentially the fractional degree to which the grid obstructs the flow. Let us imagine that the solid and the open parts of the grid are so arranged that, at the section

in which the grid is mounted, they represent an idealized and symmetrical contraction and then enlargement of the cross-sectional area of the shock tube. The minimum cross section (say A_{cr}) thus created is equivalent to A_0, the total open area of the grid.

Let us further assume that one-dimensional isentropic flow conditions are still valid. These are obviously crude assumptions. However, the presence of an expansion through the grid makes the assumption of isentropic flow a bit less unpalatable, especially prior to the advent of the choking phenomena.

Under these assumptions, we have at our disposal the standard area ratio – Mach Number relationship for an isentropic one-dimensional channel flow.[7] When the incident shock strength S (or M_s) reaches a certain value, the flow reaches Mach Number One at the minimum cross section A_{cr} of the shock tube.

Therefore

$$A_{cr}/A = f(M_s) \tag{2}$$

If one experimentally measures U_s and U_{SR} for some incident shock strength S for which the grid manifests choking, then the corresponding Mach Number M_s can be calculated from relation 1. Then by the use of relation 2, A_{cr}/A and (since $A_{cr} \equiv A_0$) the solidity ratio s of the grid can be determined.

For the case in hand, the first indication of choking of the grid appeared at incident shock strength $S \approx 3.0$. The phenomena was clearly established at $S = 3.2$ (Fig. 3a). The corresponding Mach Number $M_s \approx 0.47$ (Fig. 4). The calculated solidity ratio $s = 0.29$. The grid used had a solidity ratio $s = 0.25$ (Fig. 1). Considering the bold assumptions involved, the agreement is surprisingly close. For a grid of known solidity ratio, one should, therefore, be able to predict within a tolerable approximation, the value of Mach Number M_s of the approaching flow at which the grid will get choked.

Before submitting this article for publication, the author referred it to Glass and Patterson for their comments. They agreed that my recognition of the choked flow and the emergence of an auxiliary shock front downstream of the grid correctly establishes the true identity of the so-called "vortex" in their paper.[1] The author first observed this choking phenomena during the summer of 1953 and the results are reported in references 2 and 3.

Dr. Glass also disclosed that they are currently investigating the shock wave – screen interaction by using schlieren and interferometer techniques. They furnished the author with some of their recent interferograms and schlieren photographs on the basis of which they too had recently recognized the true identity of the "vortex". The author understands that Glass and Patterson expect to present the results of their recent investigations of shock wave – screen interaction at the Fifth International Meeting of the IAS—RAeS at Los Angeles.

References

[1] Glass, I. I., and Patterson, G. N., *A Theoretical and Experimental study of shock tube flows*, Journal of the Aeronautical Sciences, Vol. 22, No. 2, pp. 73–100, February, 1955.

[2] Dosanjh, Darshan S., *The interaction of travelling shock waves with grids*, Part II of Ph.D. dissertation, Department of Aeronautics, Johns Hopkins University, Baltimore, Md., 1953.

[3] Dosanjh, Darshan S., *The interaction of grids with travelling shock waves*, NACA TN (to be published).

[4] Kovásznay, Leslie S. G., and Dosanjh, Darshan, *Shock tube Experiments on Grid Flows*, The Physical Review, Vol. 94, No. 3, p. 789, May 1, 1954.

[5] Liepmann, Hans W., and Puckett, Allen E., *Introduction to Aerodynamics of Compressible fluids*, Chapter III, John Wiley and Sons, New York, 1947.

[6] Uberoi, Mohinder S., and Kovásznay, Leslie, S. G., *Analysis of Turbulent Density Fluctuations by the Shadow Method*, Journal of Applied Physics, Vol. 26, No. 1, pp. 19–24, January, 1955.

[7] Ferri, Antonio, *Elements of Aerodynamics of Supersonic Flows*, Chapter 1, The MacMillan Book Company, New York, 1949.

Surge Behavior in a Three-Stage Compressor

Carl E. Pearson

Assistant Professor of Applied Mechanics, Harvard University, Cambridge, Mass.

June 8, 1955

Summary

Experimental pressure and flow patterns corresponding to the onset of surge in a three-stage compressor have been studied under a variety of operating conditions. Two very different types of surging, mild and deep, were encountered. The former always occurred in the presence of stall propagation and at an operating point which depended on the exit-chamber volume; its wave form was sinusoidal and its amplitude ranged from zero upwards. The latter was of large amplitude, had a distorted wave form, and corresponded to complete flow blockage which was not overcome until the exit pressure had dropped to almost the inlet value. The onset of this deep surge was not affected by the exit volume, although its subsequent character was.

(1) Characteristics of Compressor

The compressor consisted of a set of inlet guide vanes and a stator ring, followed by three stages, each of which contained a rotor and a stator. Inlet was atmospheric, and the discharge was diffused into a chamber of variable volume which in turn discharged through a calibrated exit throttle. The exit throttle was made up of a large number of small butterfly valves distributed over one end of the exit chamber.

A set of pressure and throttle characteristics is plotted in Fig. 1 at a number of r.p.m. for the operating region near the peak of the pressure characteristics. It may be of incidental interest to remark that for flows lower than those corresponding to the pressure peaks, conventional flow pressure instrumentation was found to yield entirely erroneous operating points because of local flow irregularities. In the present compressor, the pressure drops abruptly as the flow is decreased beyond the pressure-peak point; the dotted portions of the pressure characteristics are unstable, and these portions cannot be retraced without some hysteresis.

(2) Tests with Exit Chamber Volume of 46 cu.ft.

Two strain gage pressure pick-ups were placed 180° apart on opposite sides of the exit chamber; surge would then be evidenced by the coincidence in phase of the resulting tracings (Sanborn recorder, trace speed 100 mm. per sec.). At all r.p.m., the traces were perfectly smooth until the flow was decreased beyond that corresponding to the peak of the pressure characteristic. When this point was passed by closing the throttle slightly, the character of the traces altered in a manner which depended on the r.p.m. Figs. 2 and 3 show typical traces for r.p.m. values less than and greater than 4,000 r.p.m., respectively.

The surging of Fig. 2 is called *mild* and that of Fig. 3 is called *deep*. The former could be of any amplitude down to zero, whereas the total pressure fluctuation of the latter was of the same order as the difference between peak pressure and atmospheric pressure. (For example, Fig. 3 was taken at 5,500 r.p.m., and the double amplitude of the trace was 0.11 atmospheres. The pressure scale in Fig. 2 is magnified by a factor of four as compared to Fig. 3.)

At the very lowest r.p.m., mild surging did not begin immediately the pressure peak points was passed; as the throttle was closed further, mild surge began in an intermittent fashion, and became steady and of increasing amplitude with still further closure. Finally, with the throttle almost completely closed, deep surge ensued. As the r.p.m. increased (but remained below 4,000), mild surge began sooner with throttle closure; at 4,000 r.p.m., it began immediately the pressure peak point was passed.

The presence of stall propagation[1] at various flows was next examined by placing two (uncompensated) hot wires 90° apart behind the first rotor, and again taking simultaneous tracings. No stall propagation was observed at any r.p.m. until the flow was reduced beyond the peak pressure point. For r.p.m. below 4,000, definite stall propagation then occurred for all lower flows (and it is of course this alteration in the flow character which causes the

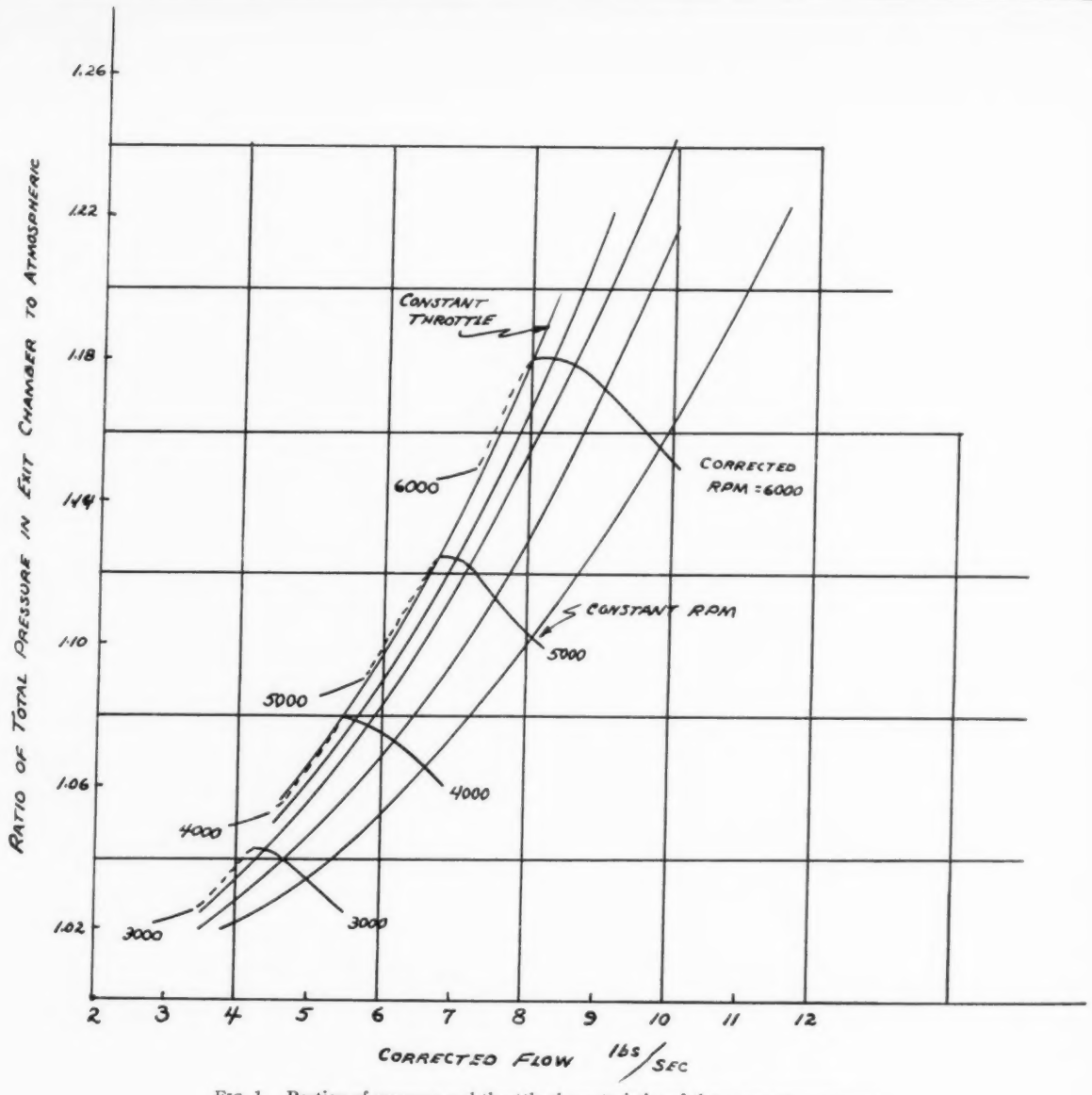

FIG. 1. Portion of pressure and throttle characteristics of three-stage compressor.

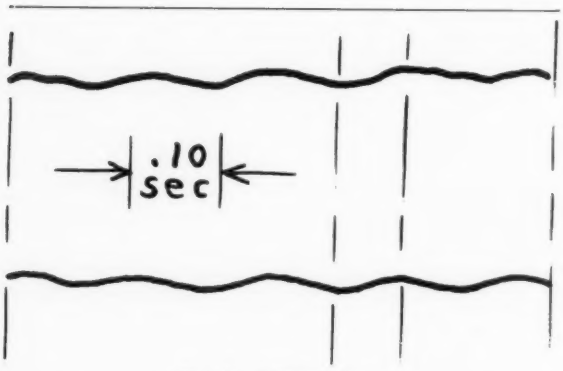

FIG. 2. Mild surging.

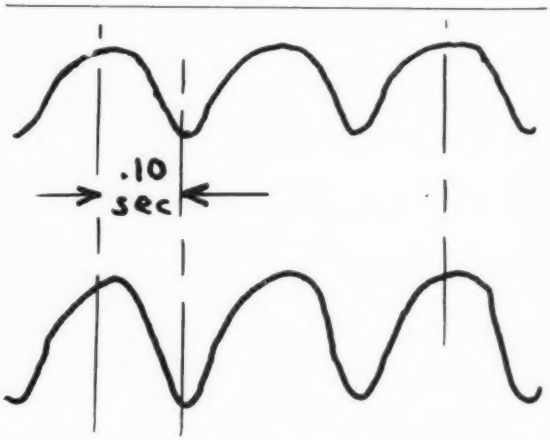

FIG. 3. Deep surging.

sudden drop in total pressure). A typical trace is shown in Fig. 4. The time separation between the two traces corresponded to usual stall propagation speeds. The frequency decreased as the throttle was further closed. For r.p.m. above, 4,000, the deep surge masked the stall propagation known from previous work[1,2] to be present during a portion of each surge cycle.

In deep surge, that portion of the curve corresponding to a pressure decrease was found to be parallel to the throttle discharge line of the exit chamber—i.e., during this portion of the surge cycle, the compressor was completely blocked. This result was checked by taking simultaneous tracings of the exit chamber pressure and the d.c. voltage across a hot wire placed ahead of the first rotor. A typical tracing is shown in Fig. 5. The lowest part of the hot-wire trace corresponds to about 10 per cent of the velocity represented by the upper part of the trace (the vertical scale is not linear, the wire being most responsive at low velocities).

By setting the operating point on the verge of deep surge, and then momentarily slightly closing and reopening the throttle, as little as a single surge pattern resulted (see Fig. 6). In no case could less than this pattern be obtained—i.e., once blockage had occurred, it could not be overcome until the exit pressure attained a level near atmospheric. It was found that the pressure fall-off time in deep surge was always about the same, corresponding to the calculated time required to discharge the exit chamber down to a level near atmospheric (the precise level affects the discharge time only logarithmically). It will be noticed for example in Fig. 7, which shows the effect of running into deep surge along a constant throttle line, that although the period of the surging is much longer than in Fig. 3, the fall-off time is about the same. The reason for the longer period of Fig. 7 is probably to be found in the more delicate surge-point setting available by use of the constant throttle line; it takes a long time for the exit pressure to build up to the blocking value.

(3) Tests with Exit Chamber Volume of 12 cu.ft.

The behavior at speeds below 4,000 r.p.m. was similar to that described in Section 2 as regards stall propagation and surging, except that mild surging was weaker and required more throttle closure for inception. For r.p.m. above 4,000, the initial deep surge was as before, except that it now did not continue. A typical trace is shown in Fig. 8 (same operating point as Fig. 3). Again, the fall-off times were roughly the same for all r.p.m., and corresponded to the discharge time for the new volume. The subsequent average pressure level was lower than with the larger volume. After the initial deep surge cycle, mild surging of various amplitudes was found superposed on stall propagation.

Discussion

If the air were perfectly incompressible, then the same proportional increase in both flow and r.p.m. would not alter the interior flow angles, and the ratio of r.p.m. to flow corresponding to the pressure fall-off point would be the same at all r.p.m. (For the above compressor, this result is indeed approximately correct.) Compressibility does however have the effect that (because of general design considerations) the last stages are closer to stall at the higher r.p.m. than the lower, when the first stage stalls. This means that stall should be more severe at the higher r.p.m.

There is an associated effect involving the pumping action of the last stages. It is known[1] that the same rotor will permit a variety of stall propagation patterns to exist at a particular flow and r.p.m. point, the total area stalled increasing as the pumping action of the latter stage decreases. In the present machine, the less-compressed flow at the lower r.p.m. has a relatively greater axial velocity in the latter stages, and so the pumping action of these stages is affected by first stage stall less than at the higher r.p.m., thus favoring less stalling in the first stage.

The combination of these two related effects would seem to account for the difference between the character of the pressure

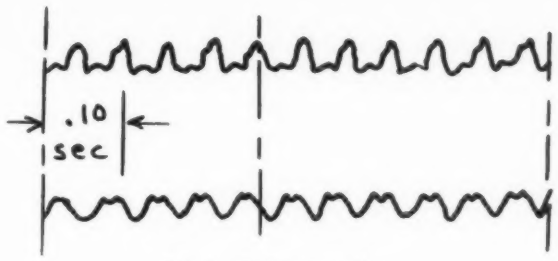

Fig. 4. Stall propagation.

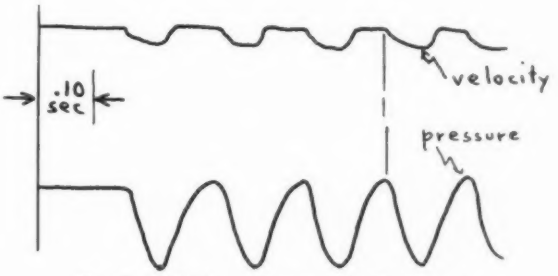

Fig. 5. Velocity and pressure in deep surge.

Fig. 6. Single surge cycle.

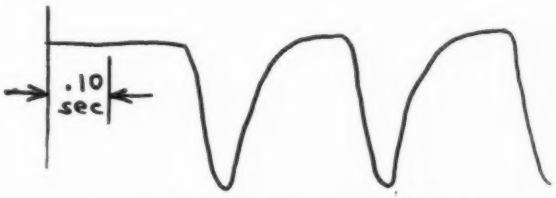

Fig. 7. Surge along constant throttle line.

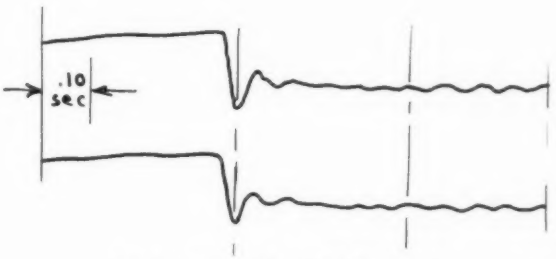

Fig. 8. Surge with small exit volume.

fall-off encountered in the two r.p.m. ranges. It may incidentally be pointed out that the slope of the pressure characteristic at that point at which deep surge commences is so steep that this term dominates all others in the criteria of reference 2 and in fact ensures fulfillment of the criteria. The question now arises as to why the deep surging continues with large volumes but not with small. Perhaps the explanation lies in the fact that with the larger volume, the pressure fall-off time and the beginning of the rise time are sufficiently long for the compressor to thoroughly purge itself of stalled flow, whereas this is not the case for the shorter times associated with the smaller volume so that the compressor in the latter case falls naturally into a stall propagation pattern. The effect would seem to be similar to that of hysteresis in a compressor, in which the flow may have a different character depending on whether it is approached from the high or low flow sides.

Mild surge in the compressor always takes place in the presence of stall propagation, but stall propagation may exist without surge. Presumably, the locally steep slope of the pressure characteristic required by reference 2 for surge is obtained by the possibility of alteration in the size of the stalled regions propagating around the wheel. Its incidence and character is very much affected by the exit chamber volume, as predicted by reference 2.

Insofar as the results of these tests may be generalized to apply to jet engine compressors, the conclusions of reference 2 may be extended by the following remarks:

(a) Other than the position of the operating point, there seems to be no overall effect—such as the presence of pressure fluctuations—which warns of the imminence of the pressure fall-off point. (This statement may have to be modified for those compressors which stall-propagate before the fall-off point is reached, where the character of the stall propagation might provide such a clue.)

(b) During acceleration, the tendency to surge is greatest in the vicinity of the knee of the surge line; this corresponds to a moderate value of r.p.m. which conceivably could fall either side of the r.p.m. dividing line described above, depending on the engine design. It is then possible that the designer may exercise some choice as to the type of pressure fall-off—i.e., as to whether the pressure is to fall to a steady nonoscillatory lower value well above atmospheric or almost to atmospheric with at least initial oscillations.

(c) It also appears that there is a critical value of combustion chamber volume, such that (assuming the r.p.m. sufficiently high) for smaller volumes only one surge cycle will occur whereas for larger volumes continued surging takes place. The latter solution may be mechanically and thermally destructive, but does have the advantage of maintaining a higher average pressure.

(d) If surge occurs at fairly high r.p.m., then the compressor remains totally blocked until its exit pressure has fallen to a certain level, and the only way in which recovery can be speeded is to increase the discharge rate of the exit air. The important fact seems to be that the blockage process can not be interrupted, as, for example, by using an emergency discharge nozzle to open automatically when the exit pressure begins to fall.

Because of the way in which the slope of the characteristic dominates the surge criteria of reference 2, it follows that the only way of preventing surge of this stall-blockage type is to inhibit the stall itself by some of the methods there discussed; alteration in burner volume or rate of fuel-burning, for example, would be expected to have little effect.

References

[1] Emmons, H. W., Grant, H. P., and Pearson, C. E., *Compressor Surge and Stall Propagation*, Trans. ASME, vol. 77, pp. 455, May, 1955.

[2] Pearson, C. E., *A Study of Surge in Compressors and Jet Engines*, Journal of the Aeronautical Sciences, Vol. 22, No. 1, pp. 10–16, January, 1955.

Supplementary Remark on "Airplane Stopping Distance"[2]

B. Saelman
Design Weight Engineer, Lockheed Aircraft Corp., Burbank, Calif.
June 9, 1955

In reference 1 a formula was given for airplane stopping distance. It should be noted that the basic differential equation for the landing ground run is integrable when the following devices, not mentioned in the above reference, are taken into account:

(1) Jet reverse thrust, usually considered constant, but may be considered proportional to a power of ground speed.

(2) Downhill or uphill component of gravity, constant.

(3) A variable coefficient of friction expressible as a polynomial in ground speed.

(4) Drag chute.

For example, if

$$\mu = \mu_0 - c\dot{x} \tag{1}$$

and the jet reverse thrust is constant, the differential equation of motion reduces to

$$(A - By)\dot{y} + Dy^3 + Ey^2 - Fy + G = 0 \tag{2}$$

where

$$y = \dot{x}$$

$$A = \frac{W}{g} + \frac{We}{gl}\mu_0$$

$$B = \frac{Wec}{gl}$$

$$D = \frac{\rho_0\sigma C_L Sbc}{2l} - \frac{\rho_0\sigma C_D Sh_2c}{2l} - \frac{\rho_0\sigma C_{D_p}S_p h_3 c}{2l} - \frac{nK_2h_1c}{l}$$

$$E = \frac{\rho_0\sigma C_D S}{2} + \frac{\rho_0\sigma C_{D_p}S_p}{2} + \frac{nK_2h_1\mu_0}{l} + \frac{\rho_0\sigma C_D Sh_2\mu_0}{2l} + \frac{\rho_0\sigma C_{D_p}S_p h_3\mu_0}{2l} - \frac{\rho_0\sigma C_L Sb\mu_0}{2l} + nK_2$$

$$F = \frac{nK_1h_1c}{l} + \frac{W\cos\theta bc}{l} + \frac{Jh_4c}{l} \pm \frac{Wce\sin\theta}{l}$$

$$G = \frac{W\cos\theta b\mu_0}{l} + nK_1 \pm W\sin\theta + J \pm \frac{We\mu_0}{l}\sin\theta + \frac{Jh_4\mu_0}{l} + \frac{nK_1\mu_0h_1}{l}$$

and

C_{D_p} = chute drag coefficient
S_p = drag chute area
θ = runway slope
J = jet reverse thrust
$K_1J = 0$
$K_2J = 0$

where the nomenclature is the same as in reference 1.

Eq. (2) can be expressed

$$\frac{By - A}{Dy^3 + Ey^2 - Fy + G}\,dy = dt \tag{3}$$

The coefficient of dy is a rational fraction and can be integrated by the method of reference 2, assuming that it can be resolved into a series of partial fractions.

From the brake characteristics, a curve of coefficient of friction versus velocity can be obtained. By substituting sets of points from the characteristic brake curve into the general polynomial relationship, an analytic expression for μ versus $\dot{x}$ can be obtained. This can then be used in the above analysis for stopping distance.

The method provides a refinement only if the actual variation in the coefficient of friction is described by Eq. (1) or a polynomial in $\dot{x}$. When the coefficient of friction is described by

different functions over the various segments of the run, an integration by segments may be performed.

Possible additional refinements would include the effects of tail loads, noncoincidence of lift and gravity forces, induced drag resulting from lift and ground effects, and rolling drag resistance of nose wheel.

References

[1] Saelman, B., *Airplane Stopping Distance*, Journal of the Aeronautical Sciences, Readers' Forum, Vol. 21, No. 11, p. 790, November, 1954.

[2] Wilson, E. B., *Advanced Calculus*, p. 20, Ginn & Co., New York, 1912.

Measurements of the Effect of Two-Dimensional and Three-Dimensional Roughness Elements on Boundary-Layer Transition*

P. S. Klebanoff, G. B. Schubauer, and K. D. Tidstrom
Fluid Mechanics Section, National Bureau of Standards, Washington, D.C.

June 15, 1955

In his study of the effect of roughness on transition, H. L. Dryden[1] found, on the basis of available data, that the effect of a two-dimensional roughness element such as a "trip wire" could be represented reasonably well in terms of a functional relation between Re_t and k/δ_k^*, where Re_t is the Reynolds Number of transition based on distance from the leading edge, k is the height of the roughness element, and δ_k^* is the boundary-layer displacement thickness at the position of the element. At his suggestion some additional data were obtained, primarily to extend the range to higher values of k/δ_k^*, during the course of an investigation of transition on a flat plate conducted at the National Bureau of Standards.[2] After the results on the two-dimensional roughness elements were obtained, it appeared to be desirable to see whether a row of three-dimensional roughness elements would behave in the same way.

The roughness elements were attached to the smooth flat plate with sharpened leading edge on which transition studies were conducted. The plate spanned the test section of the Bureau's 4½-ft. wind tunnel in which the turbulence level was sufficiently low for the Reynolds Number for the start of transition without roughness, Re_0, to be 2.5×10^6 at a wind speed of 80 ft. per sec. A small favorable pressure gradient existed over the first 1½ ft., but from there on the pressure was constant to within ±0.5 per cent of the dynamic pressure.

The two-dimensional roughness elements were cylindrical rods which were cemented individually to the surface 2 ft. from the leading edge. They spanned the plate for a distance of 1½ ft. on each side of the centerline and ranged in size from 0.033 in. to 0.1875 in. The three-dimensional elements were spheres cemented to the surface in a row perpendicular to the flow at 2 ft. and also 1 ft. from the leading edge with various spacings. Spheres 1/32-, 1/16-, and 1/8-in. in diameter were studied. Fig. 1 shows the experimental arrangement, which in this case consisted of the 1/16-in. spheres with a spacing twice the diameter and extending for a distance of 6 in. on each side of the centerline. Extension of this distance had no effect on the results. The hot-wire anemometer used to detect transition is shown in position for traversing along the centerline downstream from the spheres.

* Sponsored by the NACA.

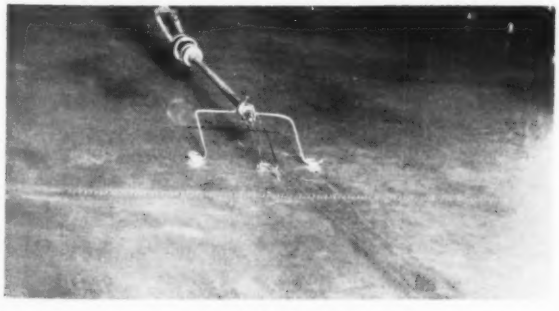

Fig. 1.

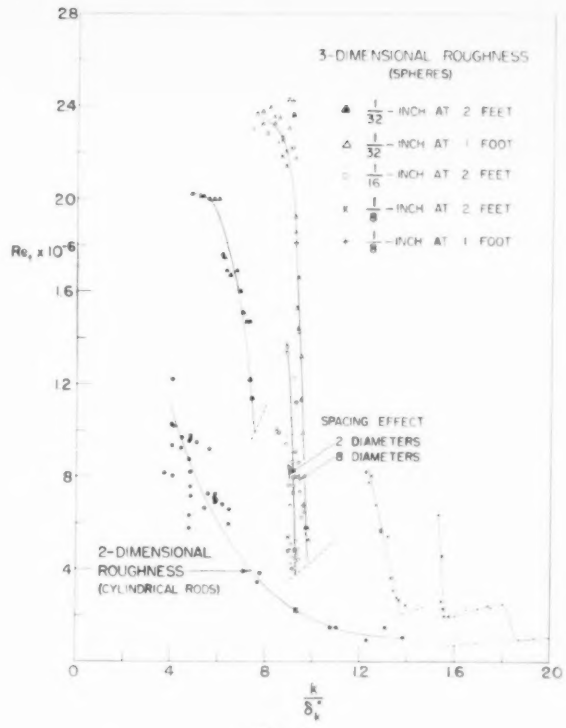

Fig. 2.

It is well known that transition need not occur at the roughness element. If the speed is low enough or the height of the roughness is small enough, transition will take place some distance downstream, beginning with the appearance of small patches of turbulence which develop in size and number over a transition region to form the fully turbulent layer, as described in reference 2. As the speed or the height is increased, the region moves upstream and becomes shorter until it finally reaches a limiting position at the roughness. It is then said to be attached. As shown in reference 1, the limiting position defines limiting lines in Fig. 2 expressed by

$$Re_t = 2.96\,(x_k/k)^2\,(k/\delta_k^*)^2$$

where x_k is the distance of the roughness element from the leading edge. These limiting lines apply to both two- and three-dimensional elements, but are shown in Fig. 2 by the short dashed curves only for the three-dimensional results. All of the plotted results pertain to the unattached condition, and values of Re_t refer to the beginning of transition. Depending on the size and position of the roughness elements, the permissible speeds ranged from 6 to 80 ft. per sec.

Dryden found that Re_t/Re_0 correlated data obtained in different wind tunnels better than did Re_t alone, account thus being taken of variations in turbulence from tunnel to tunnel. However, Re_t is used here, since the present results pertain to only one wind tunnel and since in reference 3 it is shown that the effect of stream turbulence becomes negligible for values of $k/\delta_k^* > 0.6$. Fig. 2 shows in marked contrast the difference between the

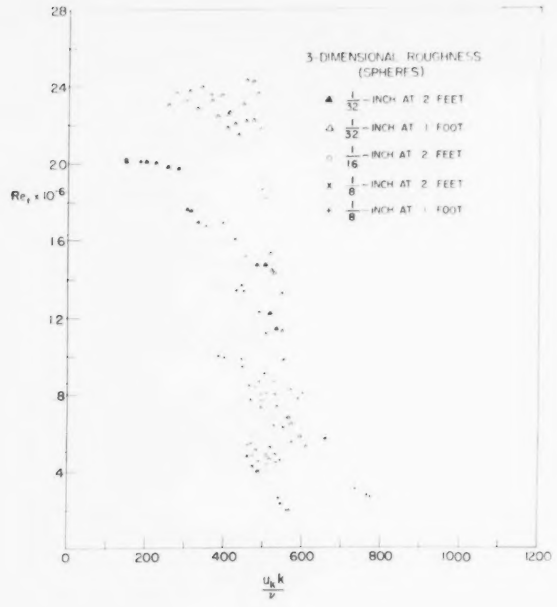

FIG. 3.

effects of two- and three-dimensional roughness. Whereas the two-dimensional results indicate a relationship between Re_t and k/δ_k^* in agreement with Dryden's findings, the three-dimensional results fail to satisfy such a relationship. The three-dimensional roughness has less effect on transition for a given k/δ_k^* than the two-dimensional roughness, but the effect is of a more critical nature. This is seen from the very narrow range of k/δ_k^* covered by a given size, indicating a rapid change in transition Reynolds Number for small changes in wind speed. Fig. 3 shows an attempt to represent the effect of the spheres in terms of a roughness Reynolds Number, $U_k k/\nu$, where U_k is the velocity at the height of the sphere. The scatter is appreciable and the nearly vertical array of points shows the sensitivity of Re_t to $U_k k/\nu$ once the effect of the roughness begins to be felt. This means that the roughness is essentially without effect until a value of $U_k k/\nu$ is reached which is likely to bring transition to the point of attachment. The following critical values for attachment appear therefore to be the practically important quantities:

	$(U_k k/\nu)_c$
1/16-in. spheres at 2 ft., spacing $8k$	573
1/16-in. spheres at 2 ft., spacing $4k$	490
1/16-in. spheres at 2 ft., spacing $2k$	518
1/8-in. spheres at 2 ft., spacing $2k$	760
1/8-in. spheres at 1 ft., spacing $2k$	890
1/32-in. spheres at 2 ft., spacing $4k$	542
1/32-in. spheres at 1 ft , spacing $4k$	578

Excluding the value of 890, the critical values are in reasonable agreement and the average is 577. The corresponding value found for the two-dimensional roughness lies between 200 and 300. It may be of interest to note that the ratio of approximately two corresponds to the relative perturbations of spheres and cylinders in potential flow.

The value of 890 is found for the curve at the extreme right of Fig. 2. Here the curve follows a pseudo limiting line, corresponding to a fixed distance downstream from the roughness, and then finally drops to the real limit. This behavior is apparently associated with the stability of the layer, and it is noteworthy that the intersection with the real limiting line does not occur until this line itself rises above what appears to be an asymptotic limit of $Re_t \simeq 90{,}000$. The corresponding Reynolds Number based on displacement thickness is 520, which is about the critical value found for a Blasius distribution for stability against small perturbations. Apparently self-sustaining turbulence will not develop below this limit no matter how large the initial disturbance. One may question why this limit should apply when obviously the mean velocity is altered just back of the roughness. It is observed that when transition occurs some distance from a roughness element, the alterations in the velocity profile have disappeared, leaving, however, perturbations that would not have been present in the absence of the roughness. It appears, therefore, that the primary effect of the roughness is to increase the magnitude of the perturbations, probably through the unstable character of the flow behind the roughness. This argument does not hold when transition occurs at the element, but in the case of a three-dimensional element, the development of a wedge of turbulence starting from the element evidently is not possible when the surrounding flow is below the stability limit.[2] This is a point which may possibly deserve further investigation in view of the possibility of obtaining much higher stability limits by means of distributed suction.

REFERENCES

[1] Dryden, H. L., *Review of Published Data on the Effect of Roughness on Transition from Laminar to Turbulent Flow*, Journal of the Aeronautical Sciences, Vol. 20, No. 7, pp. 477–482, July, 1953.

[2] Schubauer, G. B., and Klebanoff, P. S., *Contributions on the Mechanics of Boundary Layer Transition*, NACA TN 3489 (to appear also in the Proceedings of Symposium on Boundary Layer Effects in Aerodynamics, March 31–April 1, 1955, National Physical Laboratory, England).

[3] Tani, I., Iuchi, M., and Yamamoto, K., *Further Experiments on the Effect of a Single Roughness Element on Boundary Layer Transition*, Reports of the Institute of Science and Technology, University of Tokyo, Vol. 8, No. 4, August, 1954.

Errata—"On Buckling of a Clamped Rhombic Thin Plate in Shear"[1]

M. Hasegawa
Shimane University, Matsue, Shimaneken, Japan
June 22, 1955

IN REFERENCE 1, the following errata have been found:

The sentence immediately preceding Eq. (1) should read: "If w be the transverse displacement of a point on the middle plane, the total energy U of the clamped rhombic plate is expressed by the following: (see Fig. 1.)"

Eq. (1) should read:

$$2U = \frac{D}{\sin^3\alpha}\int_{-a}^{a}\int_{-a}^{a}\left\{(\Delta_1 w)^2 - 4\cos\alpha\,\frac{\partial^2 w}{\partial x \partial y}\,\Delta_1 w + 4\cos^2\alpha\left(\frac{\partial^2 w}{\partial x \partial y}\right)^2\right\}dxdy + \frac{2\lambda D}{a^2}\int_{-a}^{a}\int_{-a}^{a}\frac{\partial w}{\partial x}\frac{\partial w}{\partial y}\,dxdy \quad (1)$$

Fig. 1 should be inverted.

Table 1 should read:

55°	60°	70°	75°
125.8	98.99	65.74	51.82

The last paragraph should read: "The true value of λ_0 calculated by the author for square plate is 36.13, and B. Budiansky and R. W. Connor found that $36.12 \leqq \lambda_0 \leqq 36.49$. By comparing these values, the values in the table seem to be of good accuracy."

REFERENCE

[1] Hasegawa, M., Journal of the Aeronautical Sciences, Readers' Forum, Vol. 21, No. 10, p. 720, October, 1954.